

Dissertation

Characterization of Permanent Magnets Used in Biased Chokes

ausgeführt zum Zwecke der Erlangung des akademischen Grades
eines Doktors der technischen Wissenschaften unter der Leitung von

Univ.-Prof. Dr. techn. Manfred Kaltenbacher

E325

Institut für Mechanik und Mechatronik

eingereicht an der Technischen Universität Wien

Fakultät für Maschinenwesen und Betriebswissenschaften

von

DI (FH) DI Dominik Perchtold

Matrikelnummer 0961907

Leipziger Straße 58, 1200 Wien

Wien, am

Kurzfassung

In dieser Arbeit wird das magnetische Verhalten von vorgespannten Drosseln analysiert. Dabei handelt es sich um Spulen, die zur Kompensation des Gleichanteils des magnetischen Flusses mit Permanentmagneten (PM) vorgespannt werden. Ein magnetischer Fluss mit einem hohen Gleichanteil tritt z.B. in Umrichtern auf, in denen der elektrische Strom einen hohen Gleichanteil zusätzlich zum Wechselanteil aufweist. Diese Vorspannung kann dazu verwendet werden, die Baugröße der Drossel potenziell zu halbieren. Das Hauptaugenmerk liegt auf dem PM, da er für die Funktionalität die wichtigste Komponente darstellt, auf der anderen Seite jedoch die fehleranfälligste. Daher wird der Arbeitsbereich der Drossel gemeinsam mit dem des PM behandelt. Hinsichtlich der Simulation von Drosseln wird auf die wichtigsten Faktoren eingegangen, da es eine Reihe von Parametern gibt, die sich auf die magnetischen und elektrischen Eigenschaften der Drossel auswirken, wobei einige voneinander abhängen.

Den zweiten großen Teil der Arbeit stellt die Entwicklung einer Methode zur Charakterisierung der PM dar. Da der Einfluss von verschiedenen Belastungen auf den PM untersucht wird, wird eine schnelle und kostengünstige Methode zur Identifizierung der Haupteigenschaften des PM benötigt, nämlich der Remanenz und der Permeabilität. Diese Parameter werden mit Hilfe eines magnetischen Ersatzschaltbilds sowie 3D Finite-Elemente-Simulationen identifiziert ohne die gesamte Hysteresekurve messen zu müssen. Die Anwendbarkeit wird mit einem Messaufbau gezeigt, der für Temperaturen bis zur maximalen Arbeitstemperatur des PM und höher ausgelegt ist. Der Messaufbau ist auch für höhere Frequenzen ausgelegt, da ein Ferrit als Kernmaterial eingesetzt wird. Der Nachteil dieses Materials ist, dass es eine niedrigere Sättigung aufweist als die Remanenz des PM. Die entwickelte Methode ermöglicht dennoch die Identifizierung des PM und die Untersuchung dynamischer Einflüsse. Des Weiteren wird die Auslegung des Messaufbaus beschrieben, wobei ein besonderes Augenmerk auf der niedrigen Sättigung des Kerns und der Messung der magnetischen Feldstärke liegt.

Schließlich werden die vorgestellten Methoden und das Wissen aus den Simulationen auf eine E-Kern Drossel und ihre PM angewandt. Die PM werden einerseits magnetisch belastet und andererseits thermisch. Die Ergebnisse werden hinsichtlich reversibler und irreversibler Verluste und der beiden Belastungsarten behandelt. Eine weitere wichtige Eigenschaft der PM ist die elektrische Leitfähigkeit, die für die Bildung von Wirbelströmen verantwortlich ist und daher für eine Erwärmung der PM in der Anwendung. Die Messung der elektrischen Leitfähigkeit und ihre Auswirkungen werden in dieser Arbeit ebenfalls behandelt. Schließlich wird auf die Verringerung der Wirbelströme eingegangen basierend auf demselben Prinzip wie die Schichtung von magnetischen Kernen. Die Unterteilung der PM in kleinere Teile führt zu einer erheblichen Verringerung der elektrischen Leistung der Wirbelströme.

Abstract

In this thesis, the magnetic behavior of biased chokes is analyzed. Those are inductors biased by permanent magnets (PM) in order to compensate the static component of the magnetic flux. A magnetic flux with a high static component occurs e.g. in converters, where the electric current has a high DC component additionally to its AC component. Biasing a choke can lead to a potential reduction of the size of the choke by a factor of 2. The PM is a main focus, since it is the most important component for the functionality, but also the most fault-prone component. Therefore, the characteristics of the choke are discussed in combination with the characteristics of the PM. The most important considerations regarding the simulation of chokes are pointed out, as there are many parameters which affect the magnetic as well as the electric characteristics of the choke, where some of them are interdependent.

The second important part of the thesis is the development of a method to characterize the PMs. Since the influence of different load conditions on the PMs is investigated, a fast and inexpensive method is needed to identify the main characteristic quantities of the PMs, which are the remanence and the permeability. These parameters are identified based on a magnetic equivalent circuit and 3D finite element simulations without the necessity of measuring the complete hysteresis curve. The applicability of the method is demonstrated with a measurement setup that is designed for temperatures up to, and even higher than, the maximum operating temperature of the PMs. The setup is also designed for higher frequencies, as ferrite is chosen as a core material. The disadvantage of this material is that it has a lower saturation than the remanence of the samples under test. Nevertheless, the method developed allows for an identification of the PM and enables the investigation of dynamic conditions. The design of the measurement setup is also described, which is especially interesting with respect to the low-saturation core and the measurement of the field intensity.

Finally, the methods and knowledge from the simulations are applied to a biased E-core choke and its PMs. On the one hand, the PMs are magnetically loaded, and on the other hand, they are loaded thermally. The results are discussed in terms of reversible and irreversible losses and the two different types of load. Another important property of the PM is the electric conductivity, which leads to eddy currents and is therefore responsible for a temperature rise of the PMs in the application. The measurement and the effects of the electric conductivity are also addressed in this thesis. Finally, the reduction of the eddy currents is discussed based on the same principle as the lamination of magnetic cores. The subdivision of the PM into smaller parts leads to a significant reduction of the electric power of the eddy currents.

Danksagung

Mein herzlichster Dank gilt Hr. Univ.-Prof. Dr. techn. Manfred Kaltenbacher für die Betreuung dieser Arbeit. In zahlreichen Gesprächen und geschäftlichen Treffen konnte ich mich auf seine fachliche Unterstützung verlassen sowie auf Hinweise und Vorgabe neuer Richtungen, ohne das selbstständige Arbeiten zu vernachlässigen. Durch seine Führungskompetenz schafft er ein motivierendes und freundschaftliches Arbeitsumfeld.

Außerdem möchte ich mich bei Hr. Privatdoz. Dr. techn. Dieter Süss bedanken, der sich zur Begutachtung der Arbeit bereit erklärt hat.

Zu dem positiven Arbeitsumfeld haben auch wesentlich die Kollegen und Freunde am Institut beigetragen, die nicht nur fachlich, sondern auch abseits der Arbeit mit Rat und Tat zur Seite standen und die Zeit wie im Flug vergehen ließen. Ich bitte um Verständnis, dass ich an dieser Stelle nicht alle nennen kann. Besonders erwähnen möchte ich jedoch die Doktoren Andreas Hüppe, Hendrik Husstedt, Stefan Zörner und David Tumpold, sowie Kirill Shaposhnikov, die mich über einen langen Weg begleitet haben. Es war mir außerdem eine Freude, Ruth Polterauer, Jochen Metzger und Clemens Junger kennenlernen zu dürfen.

Zudem möchte ich den Kollegen am Institut danken, die zum reibungslosen Ablauf beigetragen haben, unterstützend gewirkt haben und hervorragende Arbeit leisten, besonders Manfred Neumann, Peter Unterkreuter und Birgit Pimperl.

Schließlich möchte ich mich noch bei meiner Familie und meinen Freunden bedanken für den Rückhalt, die Unterstützung und auch das Verständnis während dieser Zeit.

Contents

1	Introduction	1
1.1	Permanent Magnets in Magnetic Circuits	1
1.2	Motivation	2
1.3	State of the Art	4
1.3.1	Biased Chokes	4
1.3.2	Characterization of Magnetically Hard Materials	7
1.4	Structure of the Dissertation	11
2	Quasistatic Electromagnetics	12
2.1	Maxwell's Equations	12
2.2	Eddy Current Case	12
2.3	Finite Element Formulation	14
2.4	Magnetic Material and Permanent Magnets	16
2.5	Inductance	21
3	Biased Chokes	26
3.1	Operating Characteristics	26
3.2	Influence of the Electric Conductivity	32
4	Characterization of Magnetic Properties	38
4.1	Design of a Measurement Setup	39
4.2	Identification Procedure	45
4.3	Application and Verification	49
4.3.1	Verification by Simulation	53
4.3.2	Verification by Reference Measurements	53
5	Application	57
5.1	Operating Range	57
5.2	Stress Tests	62
5.2.1	Temperature Cycle up to Maximum Operating Temperature	62
5.2.2	Magnetic Load at Maximum Operating Temperature	62
5.2.3	Special Tests	67
5.2.4	Long-Term Tests at Elevated Temperatures	69
5.3	Electric Conductivity	74
5.4	Measures against Eddy Currents	80
6	Conclusion	87

1 Introduction

1.1 Permanent Magnets in Magnetic Circuits

Permanent magnets (PM) are used in many applications ranging from sensor devices like sensors measuring position, rotational speed or angle, to actuators like electrodynamic loudspeakers and electrical machines. In case of the mentioned sensors, the sensor principle is mostly to determine the presence of the magnetic field of a PM or to determine the direction of the field. In contrast to the sensors, the mentioned actuators have in common that there is mostly a closed magnetic circuit, where the field is guided by a core with a high permeability. The PM is inserted to bias the magnetic circuit and to set a specific operating point, whereas a voltage or current loaded coil is responsible for the operating range around the operating point.

The operating point can refer to e.g. a magnetic force or to the flux density itself. If the flux is guided by a magnetic core, the property of saturation is specifically important, since it determines (nearly) the maximum flux density the material can be loaded by. If the core is saturated, the desired functionality of the application is usually severely affected, whereas, on the other hand, it can also be exploited to protect certain parts of the circuit, as e.g. the PM, or other devices, by preventing a flux density or a current higher than specified. Nevertheless, the saturation is often neglected for simple considerations. However, in fact, every ferromagnetic material has this non-linear property, and therefore, it is crucial to be taken into account to accurately model such devices.

In any case, the PM is loaded by an external field, which can lead to demagnetization if the field is too high. On the other hand, the properties of a PM are subject to degradation with environmental influences like the temperature. Both of these load conditions are addressed in increasing numbers of publications in the field of electric machines, see e.g. [10], [11] and [12], and about fault current limiters [13], which focuses on the magnetic modeling. However, the presented physical models do not consider the frequency of the excitation. If the PM is operated at higher frequencies, the induced eddy currents can cause significant Joule heating. What makes this important is that many of the strong PM materials show a high electric conductivity. Their high energy product allows for a more compact design, but comes with the disadvantage of a high electric conductivity. Although electromagnetic devices can usually be cooled efficiently, this effect should be taken into consideration.

In this work, the main application of PMs is the biased choke. This is basically an inductor with a closed magnetic circuit with PMs inside. It is not only loaded by an alternating current, but also by a significant direct component, which is why they are sometimes also called DC choke or DC line reactor. Their main purpose is to store energy and to filter the electric current in applications like e.g. converters, switched-mode power

supplies and power factor corrections. The working principle is to counteract the direct component of the magnetic flux with PMs, ideally compensating it. Therefore, a larger part of the operating characteristic is available for the alternating current. One of the recently published works is [2], which provides an overview of different designs, and also suggests a new design. The work on biased inductors can be traced back to the 1950s [18], whereas reports on available products are rare. This is suspected to be related to the eddy currents and the trend towards higher frequencies in those applications. A further reason is that newer PM materials, such as rare earth magnets, make the concept more interesting due to their higher energy product, thus a smaller required volume.

1.2 Motivation

The basic working principle is described e.g. in [2], [4] or [28]. A very comprehensive explanation of the possibilities with biasing chokes is given by the simple approximation [4]

$$L \approx N \frac{\Delta B}{\Delta I} \Gamma_{\text{Fe}}, \quad (1.1)$$

where L denotes the inductance, N the number of turns of the coil, ΔB the change of the flux density, ΔI the change of the current, and Γ_{Fe} the cross section of the core. Despite the several possibilities of optimization due to the several design parameters from above, the most popular argument is the reduction of the size, i.e. the cross-section and the volume, by ideally a factor of 2. This reduction is illustrated in Fig. 1.1 by means of a simple choke. As mentioned, the electric current has a DC offset, which means that the core of an ordinary choke is only operated in the first quadrant of the flux density characteristics. The second and third quadrant remain unused. Inserting PMs into the air gaps shifts the operating point, in this case at $i = 0$, to a negative value of B_{Fe} , ideally doubling the available ΔB in the non-saturated region. According to (1.1), the cross-section Γ_{Fe} can now be halved to obtain the same inductance. In order to obtain the same maximum inductance, the effective length of the air gap, or the PM respectively, also has to be halved, if we assume that the PM has a relative permeability of 1. This is not covered by (1.1) at a first glance, but it results from the inductance being inversely proportional to the total magnetic resistance. Thus, the length has to be adjusted accordingly if the cross-section is adjusted in order to obtain the same maximum inductance, which is further explained in Chapter 3. In [4], the possibilities are also briefly discussed regarding the mass of the required copper for the coil, of the core, and regarding the core loss, switching loss and electromagnetic interference. However, in this thesis, the main focus is on the characteristics of the PM and its influence on the main characteristics of the choke, whereas the core is not considered in much detail. The major challenge in the development of biased chokes is the PM with its typically high energy product, but also its high electric conductivity.

Therefore, a part of this thesis is dedicated to the development of a measurement setup for characterizing the PMs. Since conventional means like pulsed field magnetometers (PFM) and vibrating sample magnetometers (VSM) are typically costly, specialized and

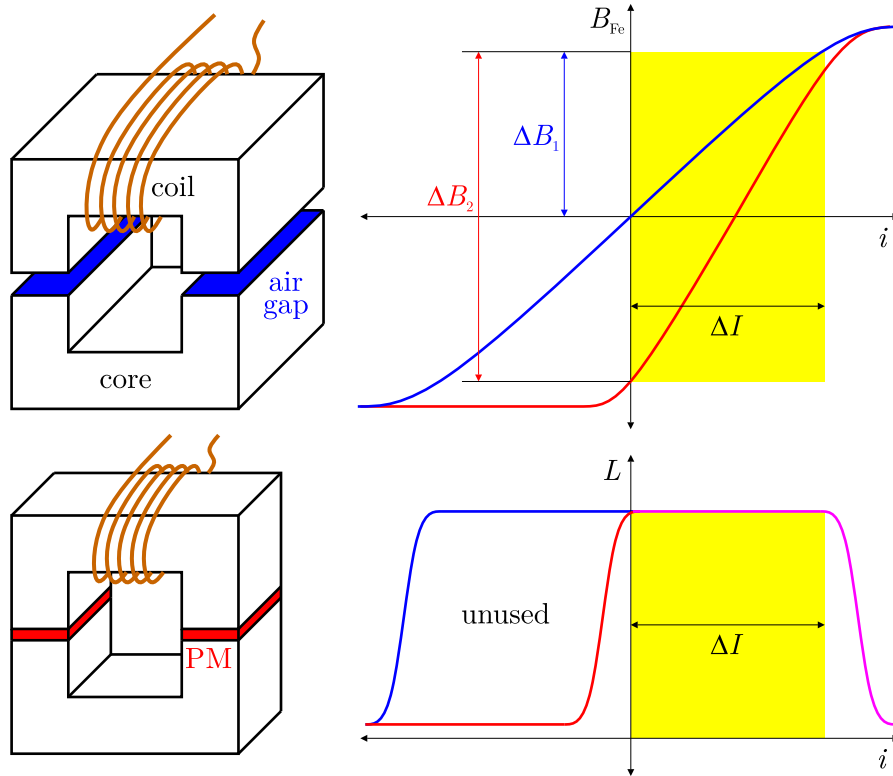


Figure 1.1: Principle of a biased choke and of the size reduction compared to a regular choke according to (1.1).

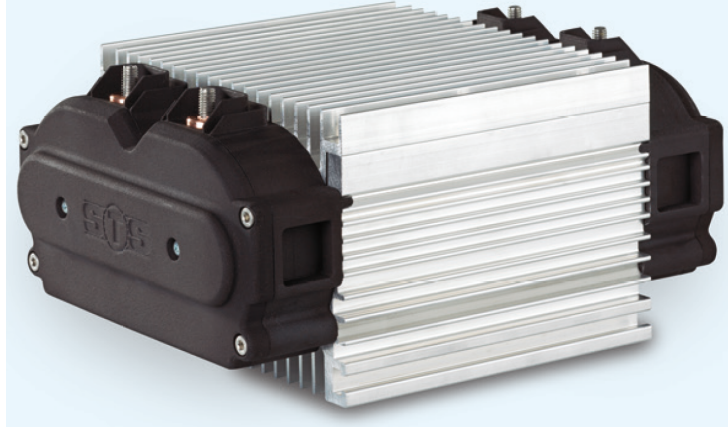


Figure 1.2: InDUR MaxFlux biased choke [5] produced by *Spezialtransformatoren Stockach GmbH*.

bulky, a method of characterization was developed with the main goal of reducing the effort and cost for the measurements. The approach is to focus on the main characteristic quantities that are relevant for the application, which are the remanence and the permeability. In order to obtain those quantities, it is not necessary to measure the full magnetization curve, which is an advantage because strong PMs require high field intensities for a full polarization. The high field intensity results in a high coil current and consequently in a high required electric power. Therefore, the measurement of only a part of the magnetization curve is advantageous regarding the excitation, since a higher power results in a higher effort and cost of the electric power source. However, the method of characterization has to be combined with accurate simulations, which is common practice in material characterization (see e.g. [27], [32]), as there is not enough information through the partial measurement of the magnetization curve alone.

1.3 State of the Art

1.3.1 Biased Chokes

As already mentioned, indications of mass-produced biased chokes are rare. However, there is a custom product manufactured by *Spezialtransformatoren Stockach GmbH* [5]. An example of this type of choke is depicted in Fig. 1.2. The photograph and the product description lead to the conclusion that the cooling plays an essential role. It also mentions the trend towards higher frequencies and current amplitudes ΔI .

Another biased choke is produced by *Payton* [7], which is depicted in Fig. 1.3. They use low-cost ferrite-based magnets having practically negligible electric conductivity. The disadvantage of those magnets is the comparably low energy product.

As mentioned, an overview of scientific publications about biased chokes is given in [2]. It also provides a categorization of the different types of biased inductors, which are

1 Introduction

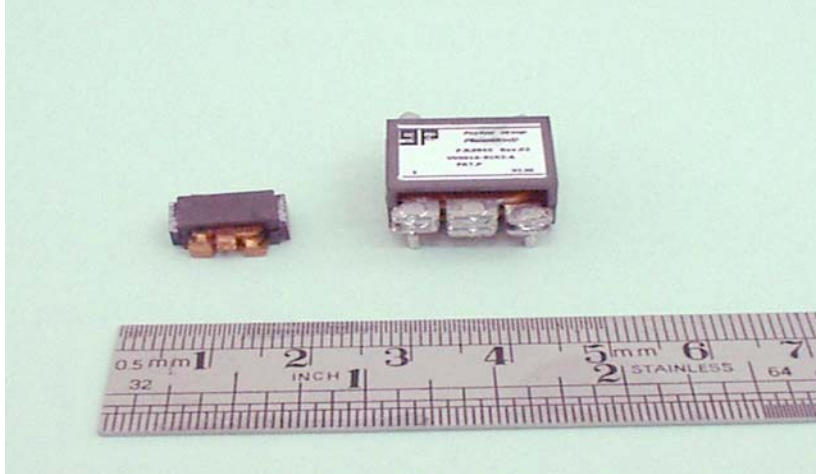


Figure 1.3: A biased choke compared to a regular choke of about the same inductance characteristics, both produced by *Payton* [7].

briefly described in the following.

The first and most obvious approach is the placement of the PM inside the air gap(s) (see Fig. 1.1). Many inductors are designed with air gaps, which allows for an adjustment of the inductance and leads to linearized characteristics over a wide range of the electric current. The placement of a PM inside an air gap does not alter the magnetic resistance too much if the PM has a relative permeability close to 1, thus the design process does not change vastly. The main characteristic is that the PM is directly exposed to the main flux, which is both an advantage and a disadvantage. On the one hand, the PM can fully contribute to the flux, on the other hand, the main flux induces the maximum possible eddy currents in the PM. A design of such a type is discussed in [14] and will be the focus of investigation of this thesis. Such a design is patented in US4009460A (1975), which consists of two EI-core configurations, where a PM is placed in one of the air gaps. Another one is US4103221 (1976), which describes an E-core as well as a U-core configuration with a plurality of PMs in one gap. Those PMs are arranged in such a way that their magnetizations are parallel. They are insulated from each other in order to prevent eddy currents. Interestingly, the PMs are explicitly specified as rare earth cobalt magnets. In DE3801542A1 (1988), a pot core is described with an air gap in the center containing the PM. A more recent patent is DE19816485C2 (1998), which claims a coil for a boost converter containing at least one air gap with a PM. The coil is further restricted to be a choke and the core is restricted to ferrite or steel and to the shape of a ring with a circular or rectangular cross-section. Another recent patent is US20090066454A1 (2008), which describes the PM as a magnetic powder mixed with adhesive bonding the two cores pieces. The powder consists of spherical magnetic particles made of rare earth alloys. The adhesive layer is specified with a thickness of less than $500\ \mu\text{m}$.

In the second type of biased inductors, the PMs are placed near the air gaps, i.e. in

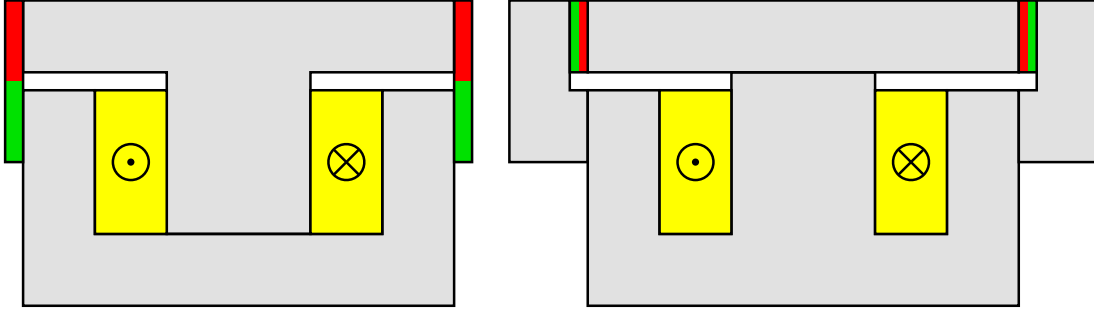


Figure 1.4: Examples of biased chokes with PM parallel to the air gaps.

parallel to the air gaps, to prevent the main flux from causing eddy currents in the PMs (see Fig. 1.4). Consequently, the advantage is a reduction of the eddy currents. On the other hand, such inductors often require non-standard core shapes and a higher design effort. An optimization example of such an inductor is presented in [15] and there also exist patents. In US5821844A (1995), several magnetic circuits are described with the PMs in parallel to the air gap, mostly in EI- or CT-core configurations. US20020039061 (2001) describes an inductor device, which can be part of a flyback transformer, in E-core configuration with the PMs adjacent to the air gap. However, the claims also refer to the planar excitation coils, and the PMs are restricted to hard ferrites. This patent could actually fit the *Payton* choke [7] (see Fig. 1.3).

The third type consists of distributed air gap cores, where basically two forms exist, as shown in Fig. 1.5. The first form is composed of laminated metal sheets, where one air gap exists per layer. The gaps are distributed in a region of the core instead of forming one air gap over the whole cross-section. Due to the lamination of the sheets and the fabrication of such cores, this type is not well suited for biasing with a PM. However, a PM could be placed outside onto the core. The second form consists of massive cores, which are usually comprised of two sections with two materials, one with a high permeability, and one with a low permeability. In this case, the low-permeability material is usually called distributed air gap material. Pressed powder cores are an example of such a material, featuring a relatively low permeability for a core material. Due to the compound, which can also contain synthetic material, there is air, or plastic, between the magnetic particles. This is why it is often referred to as distributed air gap material. In [6], an inductor with this type of core is presented, which has milled holes in order to shape the inductance characteristics. In [2], the *STS* choke [5] (see Fig. 1.2) is suspected to be of this type. The PM could be placed inside such a hole, or parallel to the whole distributed air gap core, as shown in Fig. 1.5(b). The main advantages of such designs are low stray fields and a good thermal performance, which is why they are commonly used in high frequency and high power applications.

Lastly, there is a configuration for non-gapped cores, called the *saturation gap* [2][3] (see Fig. 1.6). The PMs are placed in between two closed core configurations, creating a local saturation which should behave like an air gap, hence the name. It combines

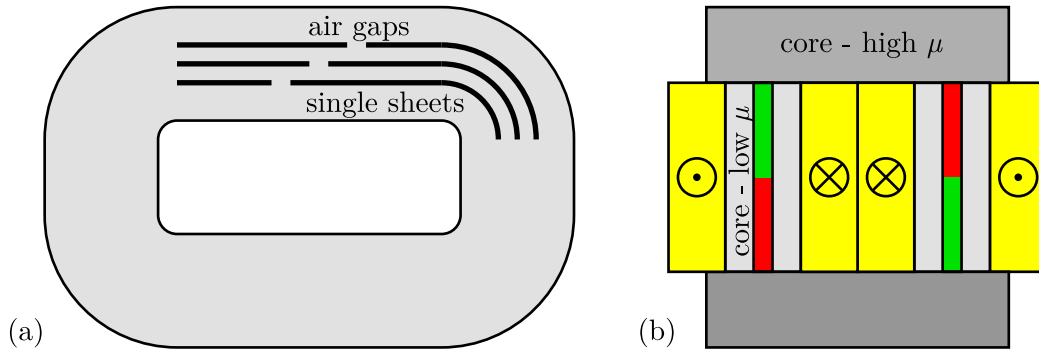


Figure 1.5: (a) Principle of distributed air gaps with laminated cores. (b) Example of a biased choke with a section of the core made of distributed air gap material with a lower permeability.

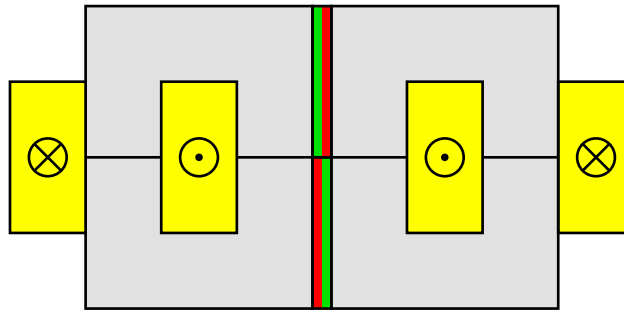


Figure 1.6: Biased choke based on the *saturation gap* [2].

the advantages of having the PMs outside the main flux and enabling the use of cores with standard shapes. Due to the lack of an air gap, the inductance characteristic is not as flat as for the first type over a broad range of electric current. Additionally, the design process is also estimated to require more effort. As the principle relies on the non-linearity and the saturation, the geometry and the material characteristics have to be modeled accurately.

1.3.2 Characterization of Magnetically Hard Materials

An overview of the different techniques to characterize magnetic materials can be found e.g. in [17] and [16], where [16] goes more into detail about specific methods. In general, magnetically hard materials can be characterized in a similar manner as magnetically soft materials. However, the main difference is that much higher field intensities are required to fully characterize, i.e. magnetize, hard materials. As a broad rule, the field intensity should be three to five times higher than the coercive field of the magnetic polarization of a PM [16], resulting in about 5 MA/m for rare earth magnets. For comparison, soft magnetic core materials saturate at field intensities in the order of 10^2 A/m. This also

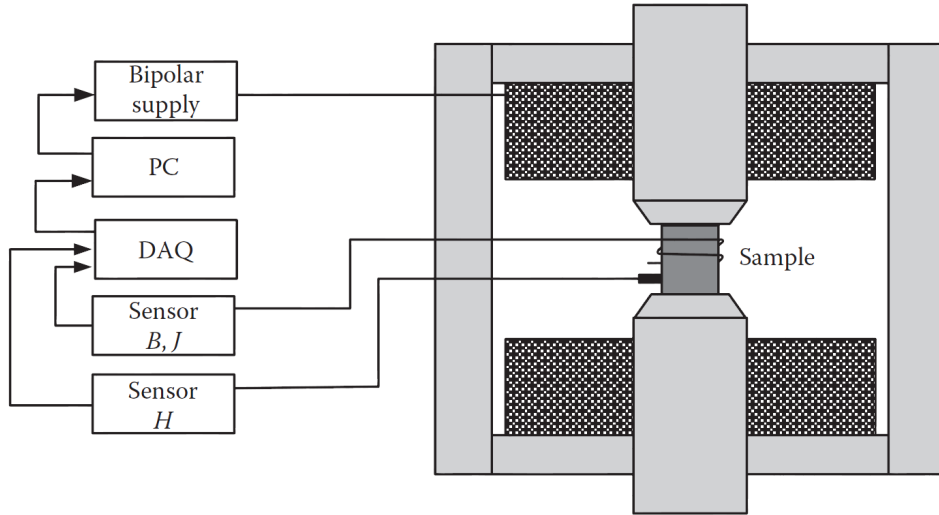


Figure 1.7: Typical testing system for hard magnetic materials [17].

leads to another difference, which is the distinction of the coercive field of the flux density and the coercive field of the polarization, which can be more than double. This is usually not needed with soft materials.

However, the coercivity can be a limitation for closed-circuit principles, since they use electromagnets to generate the external field, whose limit is the saturation of iron. Closed-circuit arrangements for a full characterization usually consist of massive iron cores with tapered, mostly exchangeable ends in the gap, where the sample under test is placed (see Fig. 1.7). Therefore, one part of the core is usually adjustable in position. As defined e.g. in the IEC 60404-5, restrictions are made to the sample geometry, or the core, depending on the point of view. Those restrictions are necessary to guarantee that the field inside the gap is as homogeneous as possible. Concerning the size and shape of the sample, there are not only minimum sizes as defined in standards, but there may also be shapes that make the use of a closed circuit impracticable. However, the closed-circuit hysteresigraph is common practice, standardized and well known, and it does not fundamentally differ from permeameters used for soft magnetic materials [16].

The second category is open-sample measurements, also called open-circuit. The main characteristic is that the field caused by the sample is not guided by magnetically soft material. That means that an external field is often generated by air coils or electromagnets with some distance to the sample. However, this is a very broad category, as it includes methods based on the measurement of force, torque and stray field. In the following, only two of the common and established methods are described, which are the vibrating sample magnetometer (VSM) and the pulsed field magnetometer (PFM). Additionally, a free-field method is briefly described, which was developed and is available at this institute.

The basic working principle of a VSM is the measurement of the magnetic moment by a pickup coil, where the sample is vibrating, i.e. varying its position, inducing

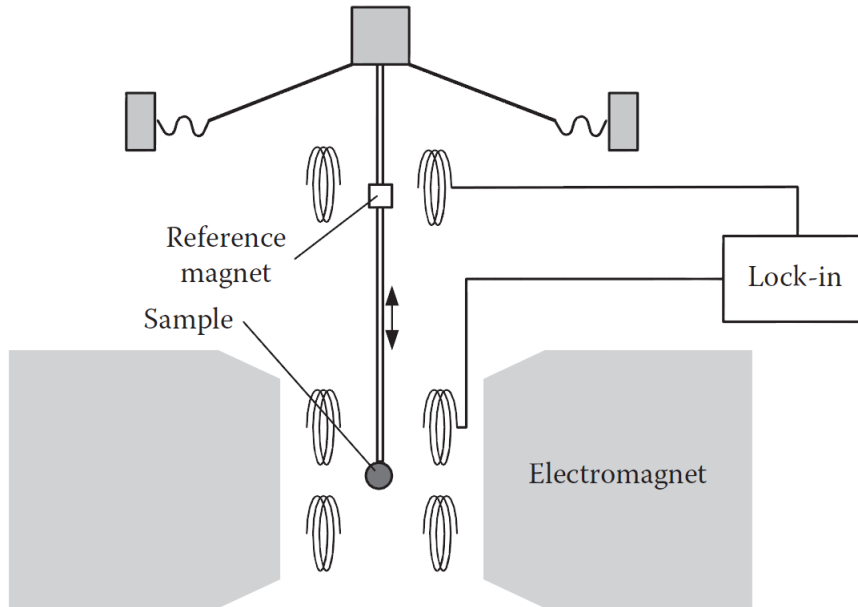


Figure 1.8: Principle of a VSM, in this case the *Foner* magnetometer [17].

a voltage in the static pickup coil. Usually, a set of pickup coils is used and there exist different arrangements of coils. The principle is depicted in Fig. 1.8, where a loudspeaker is used as mechanical actuator. In recent models, the vibration is usually generated by a piezoelectric actuator. Since this only yields small-signal results around the operating point of the sample, an electromagnet is used to generate an external field in order to measure hysteresis curves. According to [16], it has generally a high sensitivity and it is suited for small samples and even weakly magnetic or paramagnetic materials. However, the open-circuit measurements are not absolute in principle and therefore, reference samples are required. The electromagnet is a further limitation in terms of the maximum field, which prevents a full characterization of high-coercivity rare earth magnets with conventional VSMs. One alternative is a superconducting solenoid [20], which is quite expensive in acquisition and maintenance. Another alternative is presented in [21], where Halbach PM cylinders are used as an external field source.

In order to overcome the problems of the external field source, the high costs and long measurement times, the PFM was developed, which makes it attractive for industrial use (see e.g. [19]). The principle is to discharge a high capacitance onto the solenoid, where the sample under test is placed. This results in either a damped oscillatory field or a monotonically decaying field, reaching peak fields in the order of a few MA/m [16]. Due to the pulse-like excitation, the method suffers from eddy currents as well as the effect of magnetic viscosity. Those effects are addressed in several publications, e.g. [22], [23], [24], and there exist methods of compensation. Apart from that, the same rules apply as for the VSM regarding the electromagnet and the calibration by reference samples.

Finally, there is the magnetic coordinate measuring machine (MCMM), which was

1 Introduction

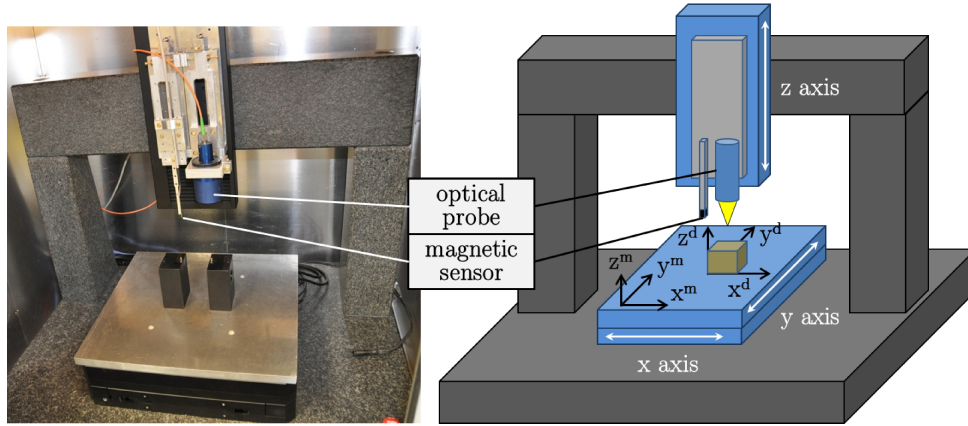


Figure 1.9: Photograph (left) and schematics (right) of the MCMM [25].

developed in course of a dissertation [25]. The MCMM consists of moving axes with both a Hall sensor and an optical probe, as depicted in Fig. 1.9. This enables measuring arbitrary magnetic fields and associating it with the geometry of a field source with high precision, which is especially important considering mechanical tolerances. This rather general concept opens up a wide range of possibilities, as e.g. testing PMs, electromagnets, pole wheels or calibrating coil arrays. Of course, the MCMM itself has to be calibrated. This can be achieved by using e.g. a single, long copper wire attached to a frame, which can be assumed as infinitely long and therefore, the field can be calculated analytically. The methods described in [26] and [27] are especially interesting for characterizing PMs. In [27], a method is described to determine the remanence of a PM if its stray field is measured. Both the permeability and the remanence affect the stray field in a similar manner and the resulting problem cannot be solved without assuming one of the two material parameters. This is why one of the quantities, in this case the permeability, has to be assumed or measured another way. The method is combined with finite element (FE) simulations to solve the optimization problem formed with the measured data. These simulations have to be carried out only once for each specific geometry and permeability.

As concluding remarks, the methods described above are usually able to fully characterize a PM, which also means to fully polarize it, depending on the source of the external field. This is not entirely true for the MCMM, which is not equipped with an electromagnet in its base configuration. However, it is also not necessary for the types of investigations presented in this thesis. As already mentioned, the new method presented in this thesis determines the state of the PM without measuring the full hysteresis loop, i.e. up to the saturation. The goal is to track the state of the PM after subjecting it to different external influences. The quality control of PMs could be another field of application.

1.4 Structure of the Dissertation

In order to perform accurate simulations of the choke and the measurement setup, the knowledge of the characteristic quantities and their physical origin is of importance. Therefore, Chapter 2 covers the electromagnetic field equations and some basics about magnetic materials. The characteristic quantities of PMs and chokes are briefly explained as well as how they can be calculated from the field quantities, which is especially important for finite element (FE) simulations.

In Chapter 3, the operating principle of a biased choke is discussed in more detail. The operating range is defined with respect to the PM and with respect to the characteristics of the choke. Details of the design and the functionality are pointed out, which are not covered by approximations of idealized models of chokes. Additionally, the effect of eddy currents is described and how they are distributed in the PM.

Chapter 4 describes the measurement setup and the method of determining the remanence and permeability of the PM samples. In order to draw conclusions from the measurements, it is necessary to examine a number of samples and to keep track of their properties during and after stress tests. This is just one of the reasons why this characterization method was developed. This chapter contains practical considerations for the design of a measurement setup, since the materials and the dimensions have a distinct impact on the functionality. It also contains the information on how the remanence and the permeability of a PM can be obtained when measuring only a part of the curve.

The application of the theory, tools and knowledge is presented in Chapter 5. The behavior of a biased E-core choke is analyzed and the PMs are subjected to different load scenarios in order to find out important factors for the application of PMs in magnetic circuits. The load scenarios include temperature as well as magnetic load. Additionally, the electric conductivity is addressed. Firstly, this covers the measurement of the conductivity, and secondly, the distribution of the eddy currents is analyzed by means of simulations and measures are presented to reduce the eddy currents significantly.

2 Quasistatic Electromagnetics

2.1 Maxwell's Equations

Maxwell's equations are a set of partial differential equations (PDE) describing electromagnetic fields. Maxwell combined and generalized the findings of Ampère, Faraday and Gauss, resulting in the following equations

$$\nabla \times \vec{H} = \vec{J} + \frac{\partial \vec{D}}{\partial t}, \quad (2.1)$$

$$\nabla \times \vec{E} = -\frac{\partial \vec{B}}{\partial t}, \quad (2.2)$$

$$\nabla \cdot \vec{D} = q, \quad (2.3)$$

$$\nabla \cdot \vec{B} = 0, \quad (2.4)$$

where \vec{H} denotes the magnetic field intensity in A/m, \vec{J} the electric current density in A/m², \vec{D} the electric displacement field, also called the electric flux density, in As/m² = C/m², \vec{E} the electric field intensity in V/m, \vec{B} the magnetic flux density in Vs/m² = T and q the free electric charge density in C/m³.

In order to solve Maxwell's equations and to consider the behavior of the electromagnetic field in different materials, the following constitutive equations are needed

$$\vec{J} = \gamma (\vec{E} + \vec{v} \times \vec{B}), \quad (2.5)$$

$$\vec{B} = \mu \vec{H} = \mu_0 \mu_r \vec{H} = \nu^{-1} \vec{H}, \quad (2.6)$$

$$\vec{D} = \epsilon \vec{E} = \epsilon_0 \epsilon_r \vec{E}, \quad (2.7)$$

where γ describes the electric conductivity in A/(Vm) = S/m, \vec{v} the velocity of free charges in m/s, μ the magnetic permeability in Vs/(Am), μ_0 the magnetic constant, also called the vacuum permeability, μ_r the dimensionless relative permeability, ν the reluctivity, which is the reciprocal of the permeability, and ϵ the electric permittivity in As/(Vm) with the vacuum permittivity ϵ_0 and relative permittivity ϵ_r , respectively.

2.2 Eddy Current Case

In order to solve the problems considered in this thesis, Maxwell's equations can be further specialized and restricted. We restrict the equations to the low frequency range, which means that electromagnetic wave propagation is neglected. This has the effect

2 Quasistatic Electromagnetics

that the displacement current term in (2.1) vanishes, which is Maxwell's extension of Ampère's law, and (2.1) reduces to

$$\nabla \times \vec{H} = \vec{J}. \quad (2.8)$$

Now, the magnetic vector potential \vec{A} is introduced, which is related to the magnetic flux density via

$$\vec{B} = \nabla \times \vec{A}. \quad (2.9)$$

Using the magnetic vector potential as unknown, (2.4) is satisfied because the divergence of a solenoidal field is zero

$$\nabla \cdot \vec{B} = \nabla \cdot (\nabla \times \vec{A}) = 0. \quad (2.10)$$

However, this leads to the solution not being unique since any gradient field $\nabla\varphi$ can be added to \vec{A} yielding the same flux density

$$\vec{B} = \nabla \times \vec{A} = \nabla \times (\vec{A} + \nabla\varphi). \quad (2.11)$$

Since a quasistatic electromagnetic field is mostly excited by current or voltage loaded coils, the right-hand side of Ampère's law (2.8) is split into an applied current density \vec{J}_a and an eddy current density \vec{J}_e , which results in a similar decomposition of the electric field. \vec{J}_e is expressed by the constitutive equation (2.5) assuming no moving bodies, which yields

$$\vec{J} = \vec{J}_a + \vec{J}_e = \vec{J}_a + \gamma \vec{E}. \quad (2.12)$$

As the applied current density is assumed to be known, only \vec{E} can lead to eddy currents. Thus, it is purely solenoidal and remains to be calculated by Faraday's law (2.2)

$$\nabla \times \vec{E} = -\frac{\partial \vec{B}}{\partial t} = -\nabla \times \frac{\partial \vec{A}}{\partial t}. \quad (2.13)$$

If \vec{A} is guaranteed to be solenoidal, this equation yields

$$\vec{E} = -\frac{\partial \vec{A}}{\partial t}. \quad (2.14)$$

Plugging (2.9), (2.12), (2.14) and the material equation (2.6) into Ampère's law (2.8) yields the quasistatic equation for electromagnetics

$$\gamma \frac{\partial \vec{A}}{\partial t} + \nabla \times (\nu \nabla \times \vec{A}) = \vec{J}_a. \quad (2.15)$$

2.3 Finite Element Formulation

The finite element method (FEM) is a numerical method to solve partial differential equations (PDE). It is an effective method to solve boundary value problems, since closed solutions mostly cannot be found for real problems. They often involve complex geometries containing multiple domains with different material parameters. Additionally, non-linear material behavior can be taken into account.

The first step is to derive the weak formulation of the quasistatic electromagnetic equation (2.15). For this purpose, it is multiplied by the test function \vec{A}' and integrated over the computational domain Ω

$$\int_{\Omega} \gamma \vec{A}' \cdot \frac{\partial \vec{A}}{\partial t} dV + \int_{\Omega} \vec{A}' \cdot \nabla \times (\nu \nabla \times \vec{A}) dV = \int_{\Omega} \vec{A}' \cdot \vec{J}_a dV. \quad (2.16)$$

Examining (2.16), the equation contains a first-order spatial derivative of the material parameter ν and a second-order spatial derivative of the unknown \vec{A} . In order to obtain the weak formulation, (2.16) is integrated by parts, which results in lowering the order of the derivatives by one and shifting it to the test function \vec{A}' . In this case, the integration by parts is based on the product rule

$$\nabla \cdot (\vec{F} \times \vec{G}) = \nabla \times \vec{F} \cdot \vec{G} - \vec{F} \cdot \nabla \times \vec{G}, \quad (2.17)$$

where \vec{F} and \vec{G} denote two general vector fields. Integrating the product rule (2.17) over Ω and applying the divergence theorem to the left-hand side yields

$$\int_{\partial\Omega} \vec{F} \times \vec{G} \cdot d\vec{S} = \int_{\Omega} \nabla \times \vec{F} \cdot \vec{G} dV - \int_{\Omega} \vec{F} \cdot \nabla \times \vec{G} dV. \quad (2.18)$$

Comparing the terms of (2.18) to (2.16), it can be found that \vec{F} corresponds to \vec{A}' and \vec{G} corresponds to $(\nu \nabla \times \vec{A})$. Additionally, (2.18) contains an integral over the surface of Ω , which corresponds to the natural boundary condition.

Before applying the integration by parts to (2.16), the boundary term is considered further. In this work, only Dirichlet and Neumann boundary conditions are of interest, which is usually called a mixed boundary condition. If specific components of \vec{A} or its normal derivative are set to zero, the magnetic flux density \vec{B} is either tangential or normal to the boundary according to (2.9). This means that these types of conditions can be applied in order to bound the computational domain in the far field and to specify a magnetic and geometric symmetry. To make the relation between the natural boundary term and the flux density clearer, the boundary term is rewritten using the properties of the scalar triple product and expressed in terms of \vec{B} and \vec{H}

$$\vec{A}' \times (\nu \nabla \times \vec{A}) \cdot \vec{n} = \vec{A}' \cdot (\nu \vec{B}) \times \vec{n} = \vec{A}' \cdot \vec{H} \times \vec{n}, \quad (2.19)$$

where \vec{n} denotes the surface normal to S . Thus, if \vec{B} is normal to the surface, i.e. parallel to \vec{n} , then $\vec{B} \times \vec{n} = \vec{0}$ (for a scalar ν) and the term vanishes. Additionally, when

2 Quasistatic Electromagnetics

using FEM, the test function is zero at a Dirichlet boundary, which is not necessarily the case for other methods as e.g. discontinuous Galerkin (DG). Consequently, setting the boundary term to zero leads to the magnetic field being normal to the surface wherever no Dirichlet condition is specified. On the part of the boundary Γ , where a homogeneous Dirichlet condition is specified, the flux density is parallel to the surface because $\vec{B} \cdot \vec{n} = 0$ leads to $\vec{n} \times \vec{A} = \vec{0}$. It should also be noted that those boundary conditions resemble the form of the interface conditions of the electromagnetic field. This means that the tangential component of \vec{H} and the normal component of \vec{B} are continuous on the interface Σ between two materials. It can be shown that the vector potential formulation satisfies those interface conditions [1].

To define the problem, a domain is considered as depicted in Fig. 2.1 involving two subdomains with different materials and showing the boundary Γ and the interface Σ [1]. In conclusion, the problem can be formulated as follows. Find $\vec{A} \in \vec{H}_0^\Sigma(\text{curl})$

$$\int_{\Omega} \gamma \vec{A}' \cdot \frac{\partial \vec{A}}{\partial t} dV + \int_{\Omega} \nabla \times \vec{A}' \cdot (\nu \nabla \times \vec{A}) dV = \int_{\Omega} \vec{A}' \cdot \vec{J}_a dV \quad (2.20)$$

for any $\vec{A}' \in \vec{H}_0^\Sigma(\text{curl})$ with the Sobolev space

$$\begin{aligned} \vec{H}_0^\Sigma(\text{curl}) = \{ \vec{u} \in (L^2(\Omega))^3 \mid \nabla \times \vec{u} \in (L^2(\Omega))^3, \\ \vec{u} \times \vec{n}|_{\Gamma} = \vec{0}, \\ [\vec{u} \times \vec{n}]|_{\Sigma} = \vec{0} \}. \end{aligned} \quad (2.21)$$

In order to obtain a system of algebraic equations, which is called the semi-discrete Galerkin formulation, the weak formulation (2.20) is discretized with Nédélec finite elements. This type of element defines the degrees of freedom on its edges. They are particularly useful for computational electromagnetics since they ensure only the tangential continuity of the unknown. The magnetic vector potential is approximated as

$$\vec{A} \approx \sum_{k=1}^{N_e} A_k^e \vec{E}_k, \quad (2.22)$$

where \vec{E}_k denotes the edge basis function of edge k , N_e the number of edges with an unknown degree of freedom and A_k^e the degree of freedom of edge k . A characteristic feature of edge elements is that the degree of freedom is a projection of the unknown quantity along the edge defined as

$$A_k^e = \int_{e_k} \vec{A} \cdot d\vec{s}, \quad (2.23)$$

where e_k denotes the line segment defining edge k . Applying the discretization (2.22) to the unknown \vec{A} and the test function \vec{A}' , the weak form (2.20) results in the following system of ordinary differential equations (ODE) in time

$$\mathbf{C} \dot{\underline{A}} + \mathbf{K} \underline{A} = \underline{f} \quad (2.24)$$

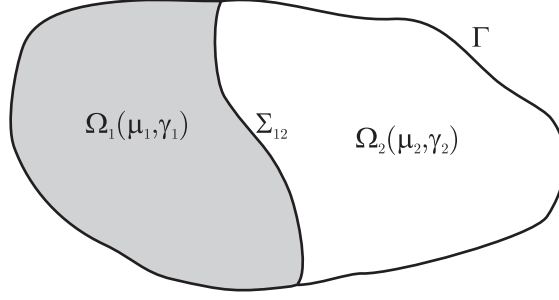


Figure 2.1: Considered domain with different materials [1].

with the damping matrix \mathbf{C} , the stiffness matrix \mathbf{K} , the vector of unknowns \underline{A} , its time derivative $\dot{\underline{A}}$ and the load vector \underline{f} . The algebraic vectors are denoted by underlines in order to distinguish them from physical vectors in \mathbb{R}^3 . According to FEM, the system of equations is assembled from the element matrices and vectors with the entries

$$\mathbf{C}^e = [C_{pq}], \quad C_{pq} = \int_{\Omega^e} \gamma \vec{E}_p \cdot \vec{E}_q \, dV, \quad (2.25)$$

$$\mathbf{K}^e = [K_{pq}], \quad K_{pq} = \int_{\Omega^e} \nu \nabla \times \vec{E}_p \cdot \nabla \times \vec{E}_q \, dV, \quad (2.26)$$

$$\underline{f}^e = [f_p], \quad f_p = \int_{\Omega^e} \vec{E}_p \cdot \vec{J}_a \, dV, \quad (2.27)$$

where Ω^e denotes the element volume.

2.4 Magnetic Material and Permanent Magnets

The magnetic properties of a material are determined by the total magnetic moment of the atoms and by the exchange interaction between the atomic moments. The magnetic moment of an atom is further caused by the sum of the magnetic moments of the electrons which consists of the spin angular moment and the orbital angular moment. This means that the electron causes a magnetic moment by moving around the nucleus and an additional moment by its spin. The exchange energy is part of the Landau-Lifshitz free energy, which describes the different contributions to the free energy of the material. It also describes the formation of domains, crystalline anisotropy, magnetostriction and saturation. It can be concluded that the magnetic properties strongly depend on the crystal structure and the geometric arrangement of the molecules. Therefore, they are also influenced by temperature, which affects the motion of the electrons and atoms.

The macroscopic magnetic properties are a consequence of these contributions. They are described by the constitutive equation (2.6) and can be further expressed by additional characteristic quantities as the magnetization \vec{M} and the magnetic polarization

2 Quasistatic Electromagnetics

\vec{P}_m , which are related by

$$\vec{B} = \mu_0 \mu_r \vec{H} = \mu_0 (\vec{H} + \vec{M}) = \mu_0 \vec{H} + \vec{P}_m. \quad (2.28)$$

Based on the macroscopic behavior, magnetic materials can be classified into different types.

- *Diamagnetic* materials show no permanent atomic moments and no interaction between the atoms. Their relative permeability is in the order of $\mu_r \approx 0.99$. Some examples are noble gases, metals like copper, gold and silver, sodium ions and organic compounds.
- *Paramagnetic* materials also neither have permanent magnetic moments of the atoms or interaction between them. Their relative permeability is $\mu_r \approx 1$. Important examples are metals like aluminium, tungsten and platinum and diatomic gases like O_2 .
- *Ferromagnetic* materials have permanent atomic moments and their interaction leads to a parallel alignment. They show a spontaneous polarization below the Curie temperature T_C and become paramagnetic above T_C . Values of their relative permeability μ_r range up to about 10^5 . Technically important examples are the metals iron, cobalt and nickel and rare earth elements as well as their compounds. This material class is very important for many technical applications and most of all, permanent magnets (PM), whose permeability is typically in the lower range.
- *Ferrimagnetic* materials show a similar behavior to ferromagnets. However, the interaction of their atoms leads to an antiparallel alignment which still results in a net magnetization. Examples are spinel ferrites, hexa- and orthoferrites and garnets. Their electric conductivity is very low, which makes them a very important material for e.g. inductors, transformers and loudspeakers.
- *Antiferromagnetic* materials exhibit an antiparallel alignment. They become paramagnetic above the Néel temperature T_N . The most important field of application of those materials are magnetic spin valves that make use of e.g. the giant magnetoresistance (GMR) or the tunnel magnetoresistance (TMR). Basically, they can be any compound of transition metals, e.g. manganese, cobalt or nickel oxide.

From a technical point of view, the more important classification of magnetic materials is made by the required magnetic field intensity to magnetize the material. They are categorized into *magnetically soft* or *magnetically hard* materials. Analogously to the electric field intensity, the magnetic field intensity corresponds to a magnetic voltage V_m which can be described by

$$V_m = \int \vec{H} \cdot d\vec{s}. \quad (2.29)$$

Hence, it is a measure of how easy or hard a material can be magnetized. The so-called coercivity or coercive field H_c is the characteristic quantity for distinguishing

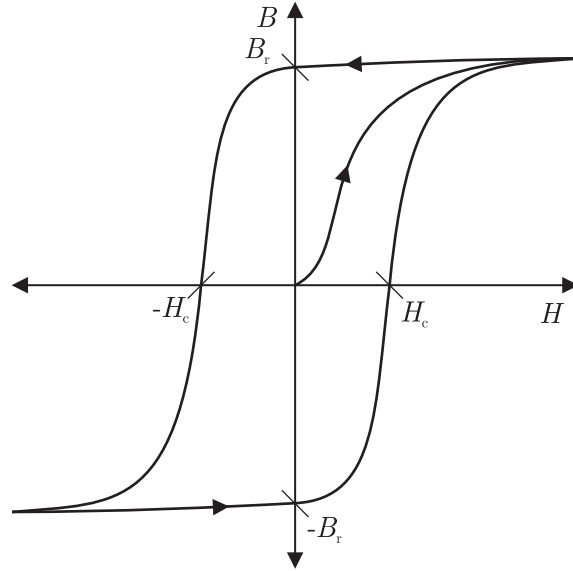


Figure 2.2: Hysteresis curve of a ferromagnetic material.

magnetically hard and soft materials. Another characteristic quantity is the remanence B_r , which describes the remanent polarization after magnetization at an applied field intensity of zero. A typical characteristic curve of a magnetic material is shown in Fig. 2.2. The flux density does not only depend on the instantaneous value of H but also on previous values, which is called hysteresis. Starting from $H = 0$, the domains start to align in the direction of the magnetic field and domain walls start moving. As all dipoles or domains are aligned in the same direction, the material is saturated and the permeability tends towards μ_0 . Reducing H to zero again, many domains stay aligned, which results in the remanence B_r . In order to decrease the flux density B to a negative value, a field intensity in the opposite direction has to be applied, with at least the value of the coercive field H_c .

It should be noted that there are different definitions of the permeability. The term permeability is often used to describe the differential permeability, which is the slope of $B(H)$. Considering the curve depicted in Fig. 2.2, the permeability according to (2.6) would have a singularity at $H = 0$ and $B = B_r$ due to a division by zero. Strictly speaking, the differential permeability tends to μ_0 if the material is saturated.

Additionally, more complex material models are needed in order to describe the hysteresis curve. A popular example is the Preisach model, which is a mathematical, phenomenological model describing hysteresis curves in a general context, not only in magnetics. For soft magnetic materials, the hysteresis curve is often approximated by a scalar function describing the mean curve of $B(H)$, as e.g. in [28]. In some situations, it can also be practical to approximate the permeability as a constant scalar, e.g. as the slope of the mean B versus H curve at $H = 0$. This significantly reduces the computation time, but at the same time the accuracy of the results is reduced, especially regarding the

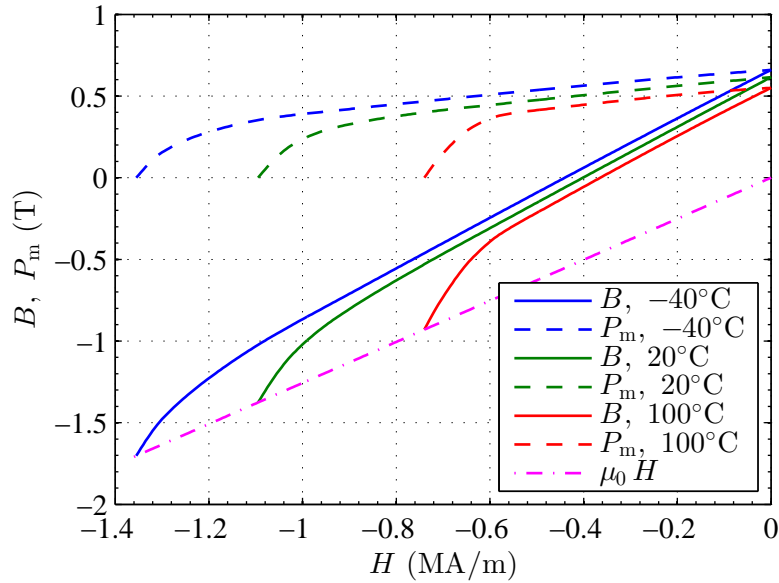


Figure 2.3: Characteristic curve of a neodymium magnet *NdFeB 55/100 pw* at different temperatures.

saturation. Neglecting the hysteresis also implies neglecting hysteresis losses, which are proportional to the area below the $B(H)$ curve, and consequently to the energy. They are part of the core loss, which also includes the Joule heating due to eddy currents.

Another important note is that Fig. 2.2 shows the flux density, which is not to be confused with the magnetization or the polarization, since they can show a strongly different slope depending on the values of the permeability compared to μ_0 (see (2.28)).

For materials with a low permeability, it is also important to distinguish between the coercive field of the flux density H_{cB} and the coercive field of the magnetic polarization H_{cJ} . In order to emphasize this, the characteristic curve of a magnetically hard material is shown in Fig. 2.3, more specifically a plastic-bonded neodymium magnet of type *NdFeB 55/100 pw* (see Tab. 2.1). It shows the B and P_m curves against H for different temperatures. For plotting the curves, several (H, P_m) value pairs were read from the data sheet and interpolated by cubic Hermite splines. The corresponding B values are calculated with relation (2.28). In order to reverse the polarization of the PM, a field intensity of H_{cJ} has to be applied, which is much higher than H_{cB} . Figure 2.3 also shows that the remanence is the same in terms of the magnetic polarization and the flux density.

Another characteristic quantity of a PM is the maximum energy product $(BH)_{\max}$, which is a measure of the stored energy per volume at the corresponding operating point. For a linear material behavior, it corresponds to double the energy density. Therefore, it is an approximation since the energy density is calculated in the general case as the integral of H with respect to a change dB . Still, it is a characteristic quantity enabling a convenient comparison between different magnets. However, the magnetic energy is

2 Quasistatic Electromagnetics

material	B_r (T)	H_{cB} (kA/m)	H_{cJ} (kA/m)	$(BH)_{\max}$ (kWs/m ³)
HF 30/26, hard ferrite, anisotropic, pressed	0.405	250	270	31.5
NdFeB 358/111, rare earth, anisotropic, sintered	1.39	907	1114	375
NdFeB 55/100, rare earth, isotropic, plastic-bonded, pressed	0.62	400	1100	65
Sm ₂ Co ₁₇ , rare earth, anisotropic, sintered	1.1	800	1800	220
AlNiCo 40/12, anisotropic, cast	0.85	120	127	40
AlNiCo 52/6, anisotropic, cast	1.3	55	56	52

Table 2.1: Characteristic values of several types of permanent magnets. Values obtained from material data provided by manufacturers of PM, *MS-Schramberg GmbH & Co. KG* and *Magnetfabrik Bonn GmbH*, as of June 2015.

not an easy topic, which is why [33] is referred to, which provides a comprehensible discussion about the stored energy and the energy in a magnetic circuit. An overview of the magnetic properties of selected PM types is given in Tab. 2.1. The values are either typical or minimal values as available. Additionally to the name of the material, the production technique and the directional dependency of the parameters are shown. Every type of PM has its advantages and disadvantages regarding the application. Rare earth magnets show a high energy product and coercivity, hard ferrites typically have the lowest electric conductivity, and the AlNiCo alloys show high maximum operating temperatures and remanence, but a low coercivity. The electric conductivity of rare earth magnets can also be reduced by mixing the compound with synthetic material, which also influences the magnetic properties, as can be seen with the plastic-bonded neodymium magnet.

Since the remanence is the key feature of a PM, it cannot be neglected, whereas for soft magnetic materials, modeling the mean $B(H)$ curve is often sufficient. In order to model the remanence without a complex hysteresis model, a convenient way is to describe the material law as

$$\vec{B} = \mu \vec{H} + \vec{B}_r, \quad \vec{H} = \nu (\vec{B} - \vec{B}_r), \quad (2.30)$$

where μ and ν model the differential material parameters if $B(H)$ describes a straight line. If μ is non-linear, the offset of the curve B_r also depends on H , resulting in $\partial B / \partial H \neq \mu$. The usage of this model instead of (2.6) also has to be considered when calculating other quantities like the magnetization (see (2.28)). However, using (2.30), non-linearities of ν and \vec{B}_r can be treated separately, e.g. when taking the temperature into account. It can also be used to model a part of the hysteresis [31]. Moreover,

2 Quasistatic Electromagnetics

the remanence can be added directly to the FE system of equations without having to compute intermediate quantities. Using (2.30) as material law, only the right-hand side of the FE formulation (2.24) is extended

$$\underline{f}^e = [f_p], \quad f_p = \int_{\Omega^e} \vec{E}_p \cdot \vec{J}_a \, dV + \int_{\Omega^e} \nabla \times \vec{E}_p \cdot (\nu \vec{B}_r) \, dV. \quad (2.31)$$

Hence, the representation of a PM as a source term is derived in terms of field quantities. Analogously to electric circuits, a PM can also be represented as a source in magnetic equivalent circuits. The real magnetic circuit is subdivided into parts each having a material parameter which is constant over its region. The subdivision is usually also made by geometric considerations. Each part, which is called the lumped element, is assumed to have a constant magnetic voltage (see (2.29)) along the path through the part and a constant magnetic flux Φ over its cross-section, which can be expressed as

$$V_{m,p} = \int_{l_p} \vec{H} \cdot d\vec{s} \approx H l_p, \quad (2.32)$$

$$\Phi_p = \int_{\Gamma_p} \vec{B} \cdot d\vec{S} \approx B \Gamma_p, \quad (2.33)$$

where Γ_p denotes the cross-section of part p and l_p the length of the path. This also means that \vec{H} is assumed parallel to \vec{B} within a part. With these quantities, the magnetic resistance is defined as

$$R_{m,p} = \frac{V_{m,p}}{\Phi_p} = \frac{l_p}{\mu_p \Gamma_p}, \quad (2.34)$$

where μ_p is the permeability in part p . As indicated by the characteristic quantities H_{cB} and B_r , a real PM cannot provide a constant B over the whole H range and vice versa. Therefore, it can be modeled as a non-ideal source, which can either be a magnetic flux or voltage source with the internal resistor $R_{m,PM}$, as depicted in Fig. 2.4. The internal resistor represents the geometric and material properties of the PM, whereas the ideal source represents the source term or excitation, analogously to the source term (2.31) for the field quantities. The values of the sources are related to the circuit quantities by

$$V_{m,PM0} = H_{cB} l_{PM}, \quad (2.35)$$

$$\Phi_{PM0} = B_r \Gamma_{PM}, \quad (2.36)$$

where l_{PM} is the dimension in direction of magnetization and Γ_{PM} the cross-section normal to the magnetization.

2.5 Inductance

The inductance is an important characteristic parameter of a magnetic circuit, especially if the frequency behavior is of interest. Since many magnetic circuits are used as e.g.

2 Quasistatic Electromagnetics

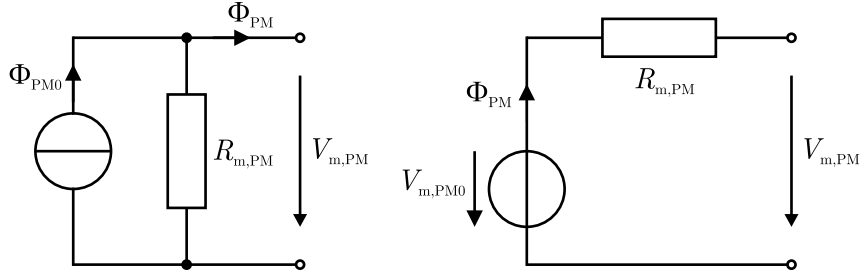


Figure 2.4: Magnetic equivalent circuit representations of a PM.

passive filters, short-term energy storage elements and actuators, it is crucial to be able to predict the inductance, which is a measure of the electric energy stored as magnetic energy. It allows for calculating the electric voltage drop in case of a coil excited by a known current or for calculating the current if a voltage is applied.

Let us consider an electric circuit with an inductor connected in series with a resistor and an ideal voltage source, as depicted in Fig. 2.5. Kirchhoff's voltage law results in the equation

$$u = Ri + L \frac{\partial i}{\partial t}, \quad (2.37)$$

where u denotes the electric voltage, i the current and L the inductance. As there are different definitions of the inductance, it is important to know which one is to be used in which situation. Usually, the inductance is calculated as the static inductance

$$L_s = \frac{\Psi}{i}, \quad (2.38)$$

where Ψ denotes the flux linkage defined as

$$\Psi = N \Phi \quad (2.39)$$

with the number of turns N of the coil and the flux Φ through the coil. This inductance is also often called secant inductance or large-signal inductance. It is a matter of definition, but strictly speaking, it is only correct if the circuit contains no permanent magnet (PM) and the material behavior is linear. In fact, it is a linear approximation which implies that the magnetic energy W can be calculated by

$$W = \frac{1}{2} L_s i^2. \quad (2.40)$$

The reason why this is an approximation can be examined by considering the relation between the coil current and the flux linkage in more detail. In Fig. 2.6, the behavior of the flux linkage is shown in the linear and in the non-linear case. From Fig. 2.6(a), the origin of the approximation of the magnetic energy (2.40) becomes clearer. The magnetic energy corresponds to the area beneath the $i(\Psi)$ curve. As the flux linkage is a straight line through the origin, the magnetic energy equals the area of a triangle which

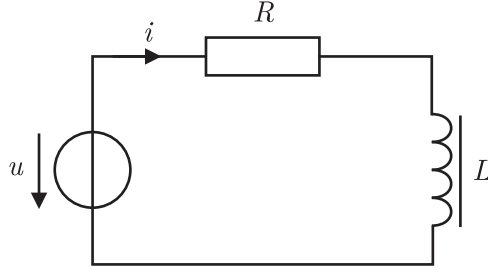


Figure 2.5: Inductance in series with a resistor and a voltage source.

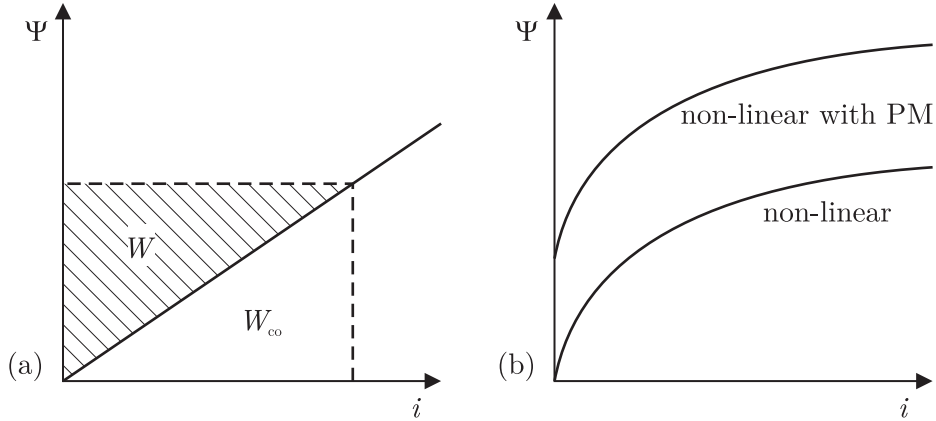


Figure 2.6: Flux linkage against coil current for (a) a linear circuit and (b) non-linear circuits with and without a permanent magnet.

can be calculated by (2.40) and is equal to the magnetic co-energy W_{co} . This is no longer the case if the non-linear curves in Fig. 2.6(b) are considered. If the material parameter is non-linear, the area beneath the curve is no longer a triangle. If the circuit contains a PM, the flux linkage is not necessarily zero at $i = 0$, which leads to a singularity if the inductance is calculated by (2.38).

The non-linear case includes either a non-linear material parameter or a PM. This means that even in case of a linear material parameter, the relation of Ψ and i is still non-linear if there is a PM in the circuit. In these cases, the differential inductance has to be used which is defined as

$$L_d = \frac{\partial \Psi}{\partial i} \quad (2.41)$$

and which provides a measure of the storable magnetic energy per electric current at every time instant. With the differential inductance, the current or voltage is correct in any case regarding the electric circuit. Plugging L_d into the considered circuit equation (2.37) yields

$$u = Ri + \frac{\partial \Psi}{\partial i} \frac{\partial i}{\partial t} = Ri + \frac{d\Psi}{dt}, \quad (2.42)$$

which shows that the voltage drop over the inductor is equivalent to the total time

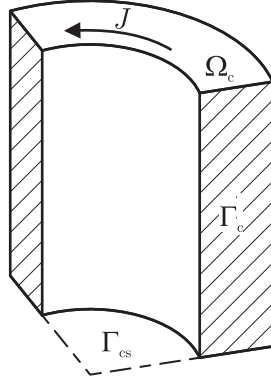


Figure 2.7: Cut through a cylindrical coil with the different cross-sections Γ and the current density J . The volume Ω_c refers to the whole hollow cylinder in this case.

derivative of Ψ if the differential inductance is used.

In order to make use of the benefits of FE simulations, which take into account the geometric and material properties of a magnetic circuit, the flux linkage has to be calculated with quantities available during the computations, i.e. the magnetic vector potential in this case. Hence, the definitions of the flux linkage and the magnetic flux are considered to obtain

$$\Psi = N \Phi = N \int_{\Gamma_{cs}} \vec{B} \cdot d\vec{S} = N \oint_{\partial\Gamma_{cs}} \vec{A} \cdot d\vec{s}, \quad (2.43)$$

where Γ_{cs} denotes the cross-section of the flux passing through the coil. To provide a better overview of how the coil is modeled, a cut of a cylindrical coil is depicted in Fig. 2.7. The current i is assumed to be equally distributed over the winding cross-section Γ_c , which leads to a current density \vec{J} with a constant magnitude over the coil volume Ω_c . This is an accurate approximation of a coil with many turns, since the skin effect can be neglected in a single turn regarding its contribution to the magnetic field. In general, it can be difficult to find the right contour to evaluate the integral in (2.43). Therefore, the flux is averaged over the whole coil and normalized to the cross-section of the coil [1], which leads to

$$\Psi = \frac{N}{\Gamma_c} \int_{\Omega_c} \vec{A} \cdot \vec{e}_J dV, \quad (2.44)$$

where \vec{e}_J denotes the unit vector of the current density. With (2.44), the flux linkage can be calculated during FE simulations. For coils excited by an ideal current source, Ψ is just a result of post-processing, i.e. it is not coupled to the FE system of equations. In this case, the voltage drop can be calculated by taking the time derivative of (2.44).

If the coil is loaded by a voltage source as depicted in Fig. 2.5, the flux linkage has to be incorporated into the FE system of equations. Using (2.44), the circuit equation

2 Quasistatic Electromagnetics

(2.42) can be added to the FE system (2.24) resulting in

$$\begin{bmatrix} \mathbf{C}_A & \underline{0} \\ \underline{f}_{iA}^T & 0 \end{bmatrix} \begin{bmatrix} \underline{\dot{A}} \\ \dot{i} \end{bmatrix} + \begin{bmatrix} \mathbf{K}_A & -\underline{f}_{iA} \\ \underline{0}^T & R \end{bmatrix} \begin{bmatrix} \underline{A} \\ i \end{bmatrix} = \begin{bmatrix} \underline{0} \\ u \end{bmatrix}, \quad (2.45)$$

where \mathbf{K}_A and \mathbf{C}_A denote the original matrices from (2.24) and the coupling vector is composed of the element load vectors

$$\underline{f}_{iA}^e = [f_p], \quad f_p = \frac{N}{\Gamma_c} \int_{\Omega^e} \vec{E}_p \cdot \vec{e}_J dV. \quad (2.46)$$

3 Biased Chokes

As described in the introduction, the main idea of biasing an inductor is to shift its operating characteristic to higher coil currents. This enables utilizing a higher range of the magnetization curve of the core material in applications with an unipolar load. This means that the coil current shows a high DC component additionally to the AC component. The higher usable range of the flux density opens up new possibilities for the optimization of the inductance or the volume of the inductor. In this chapter, several aspects of the operating characteristics are considered by means of practical examples as well as influences that are not described by the ideal relation (1.1).

3.1 Operating Characteristics

The most important design parameters of a biased inductor are the flux density in the core and the overall inductance. In the following example, the effects of biasing a choke are shown regarding the operating characteristics and compared to the unbiased version of the choke. Since the saturation of the core material significantly affects the inductance, the non-linear behavior of the core is taken into account.

To demonstrate the effect of biasing, a simple choke is considered consisting of 2 U-shaped ferrite cores, as depicted in Fig. 3.1, put together and separated by an air gap. The most obvious strategy to bias this magnetic circuit is to place PM inside the air gaps in such a way that they cause a flux which opposes the flux caused by the coil. The idea is that, except for the biasing, the insertion of the PM inside the air gap should not lead to significant changes because the permeability of a PM with a high energy product is typically in the range of the permeability of air, i.e. $\mu_r \approx 1$. However, in order to obtain an accurate model, the permeability of the PM has to be specified correctly. This is due to the fact that inductors with an air gap use this gap for energy storage, additionally to its linearizing effect. This means it has a comparably high, constant magnetic resistance and contributes largely to the inductance due to the approximation

$$L \approx \frac{N^2}{R_m}. \quad (3.1)$$

For circuits containing a PM, (3.1) also yields an approximation of the maximum inductance.

Another effect of a large air gap is that stray fluxes cannot be neglected, as shown in e.g. [28]. Therefore, they are also taken into account in form of the resistors R_{S_k} parallel to the main parts of the air gaps, which are modeled as the resistors $R_{\text{gap}k}$ and which have the same cross-section as the core. In order to obtain a general and flexible model,

3 Biased Chokes

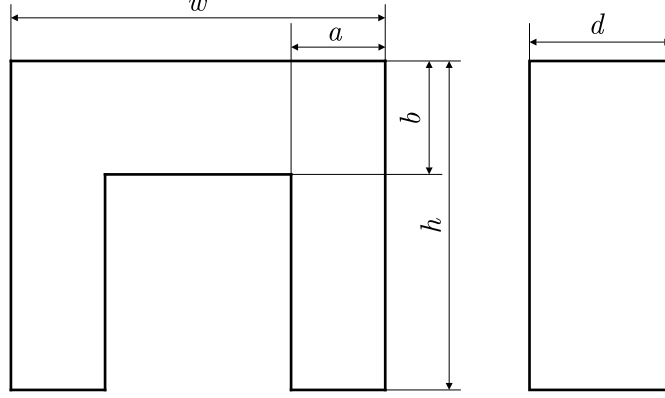


Figure 3.1: Drawing and definition of the dimensions of one core of the U-core choke.

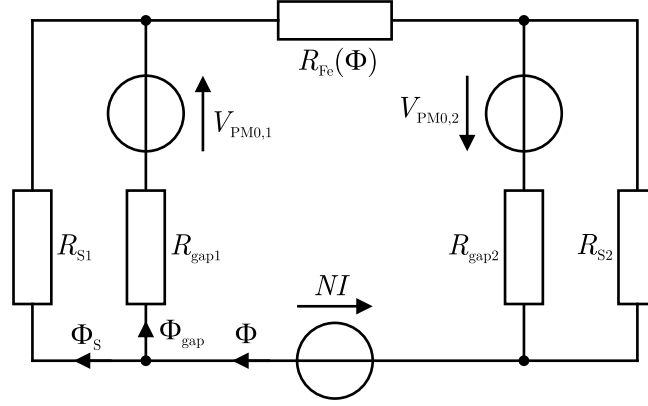


Figure 3.2: Magnetic equivalent circuit of the U-core choke with 2 air gaps.

the two gaps are modeled separately, as depicted in Fig. 3.2, which would also allow, e.g., inserting only one PM. The PM are modeled as non-ideal magnetic voltage sources opposing the voltage applied by the coils. If considering all cases with and without a PM, the air gap resistances $R_{\text{gap}k}$ can take the values R_{PM} or R_{air} , which are defined by

$$R_{\text{PM}} = \frac{l_{\text{gap}}}{\mu_{\text{PM}} \Gamma_{\text{gap}}}, \quad R_{\text{air}} = \frac{l_{\text{gap}}}{\mu_0 \Gamma_{\text{gap}}} \quad (3.2)$$

with the cross-section $\Gamma_{\text{gap}} = a d$. Without a PM, the magnetic voltage $V_{\text{PM}0,k}$ is set to zero.

In order to take the non-linearity of the core into account, its characteristic curve is modeled as described in [28]

$$B(H) = \frac{H}{c_1 H + c_2} + \mu_0 H, \quad (3.3)$$

where c_1 and c_2 are fitting parameters. From (3.3), the reluctivity can be calculated analytically, which has the limit $\nu_0 = 1/\mu_0$ for $B \rightarrow \infty$. With the known reluctivity, the

3 Biased Chokes

magnetic resistance of the core can be described as

$$R_{\text{Fe}}(\Phi) = \nu_{\text{Fe}}(|B_1|) B_1 l_1 + \nu_{\text{Fe}}(|B_2|) B_2 l_2, \quad (3.4)$$

where $l_1 = 4h - 2b$ and $l_2 = 2(w - a)$. Analogously to l_1 and l_2 , B_1 and B_2 represent the flux densities in the parts of the core grouped by their two different cross-sections. They are calculated as $B_1 = \Phi/\Gamma_{\text{gap}}$ and $B_2 = \Phi/\Gamma_{\text{Fe}}$ with $\Gamma_{\text{Fe}} = b d$.

With all the resistors defined, Kirchhoff's circuit law leads to the system of equations

$$\begin{bmatrix} R_{\text{Fe}}(\Phi) & R_{\text{gap1}} & R_{\text{gap2}} & 0 & 0 \\ 0 & -R_{\text{gap1}} & 0 & R_{\text{S1}} & 0 \\ 0 & 0 & -R_{\text{gap2}} & 0 & R_{\text{S2}} \\ -1 & 1 & 0 & 1 & 0 \\ -1 & 0 & 1 & 0 & 1 \end{bmatrix} \begin{bmatrix} \Phi \\ \Phi_{\text{gap1}} \\ \Phi_{\text{gap2}} \\ \Phi_{\text{S1}} \\ \Phi_{\text{S2}} \end{bmatrix} = \begin{bmatrix} N I - V_{\text{PM0,1}} - V_{\text{PM0,2}} \\ V_{\text{PM0,1}} \\ V_{\text{PM0,2}} \\ 0 \\ 0 \end{bmatrix}. \quad (3.5)$$

For the following results, the parameters are chosen as $w = 33$ mm, $a = 8.3$ mm, $b = 10$ mm, $h = 29$ mm, $d = 25$ mm, $l_{\text{gap}} = 1.5$ mm, and $N = 56$. The fitting parameters of the core material are chosen as $c_1 = 2.04 \text{ m}^2/(\text{Vs})$ and $c_2 = 59.45 \text{ Am}/(\text{Vs})$, which approximates the behavior of the ferrite *3C90* manufactured by *Ferroxcube*. The coil current is varied in constant steps of $\Delta I = 1$ A from $I = -30$ A to $I = 30$ A. For the simulation with PM, the parameters of the material *NdFeB 55/100 pw* (see Tab. 2.1) are taken and a linear relative permeability of $\mu_r = B_r/H_{\text{cB}}/\mu_0 = 1.2335$ is assumed. The stray resistors R_{Sk} are chosen as $(1 - 0.35)/0.35 R_{\text{gapk}}$, which results in 35% stray flux compared to Φ and which is a realistic value for this choke [28].

The flux density in the core is shown in Fig. 3.3, where B_{Fe} indicates that it is calculated with Γ_{Fe} . The differential inductance, as shown in Fig. 3.4, is calculated by (2.41) using the central difference quotient, and the forward and backward difference for the first and the last value, respectively. From these two main design parameters, the effect of biasing can be observed. For a better overview, the black, dashed lines mark the range of the current, where the maximum inductance is obtained and where it is nearly constant, which is from about $I = 8$ A to $I = 20$ A. Due to the higher permeability of the PM compared to air, the flux density curve shows a slightly higher slope, which also results in higher inductance. It is also shown that a choke of the same dimensions, but without a PM, would not satisfy the requirements in the specified current range. In order to obtain a suited inductor for the same current range, the length of the air gap l_{gap} as well as the depth d have to be doubled, which results in doubled cross-sections Γ_{Fe} and Γ_{gap} , and consequently in a doubled volume (neglecting the contribution by l_{gap}). To satisfy the requirement, the constant inductance range has to be enlarged, which means enlarging the air gap, but in turn, the larger air gap leads to a lower inductance due to (3.1). Therefore, the cross-section has to be enlarged too due to (1.1). It should be noted that solely a change of the cross-section does not lead to a change of the B vs. I characteristic, since only the flux is affected, but not the flux density.

Another important aspect is the operating range of the PM, as it is limited by the coercive field H_{cJ} . If the field intensity approaches H_{cJ} or, depending on the shape of the magnetization curve, it approaches the knee of the operating characteristic (see Fig. 2.3),

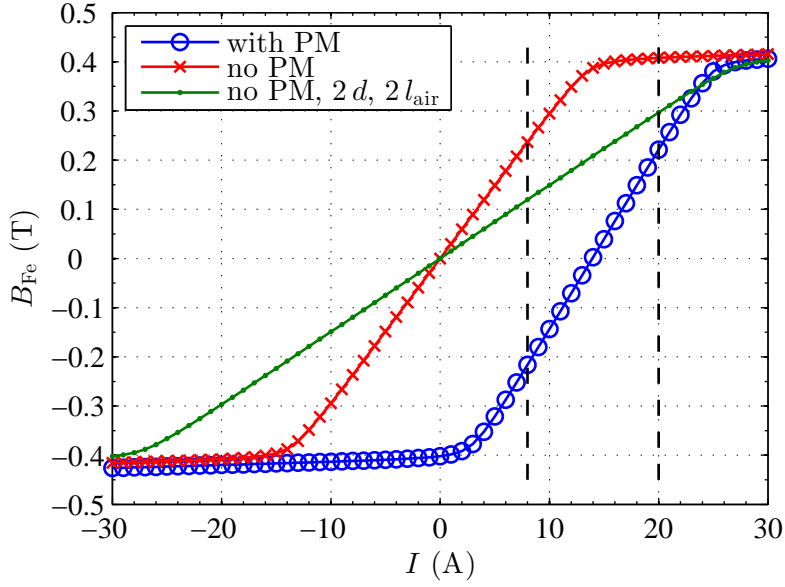


Figure 3.3: Magnetic flux density in the core of the U-core choke against coil current with PM, without PM, and with doubled cross-section and air gap.

the linear description of the permeability is not accurate any more. More importantly, the PM can lose some of its remanence or be demagnetized. The H vs. B range of the PM from the above example is shown in Fig. 3.5. In this case, the PM is safe from being demagnetized by the coil, since it has a large $(BH)_{\max}$ and H_{cJ} . It is even protected by the saturation of the ferrite, which means that demagnetizing it would require extremely large currents that are unlikely to occur. If another type of PM is used, e.g. a hard ferrite *HF 30/26* (see Tab. 2.1) with a low electric conductivity but also a lower $(BH)_{\max}$, the volume of the choke has to be increased again. In this case, the PM needs a higher gap length l_{gap} so that it can provide enough magnetic voltage to counter the coil, and d has to be increased to preserve the inductance, which can be observed when comparing the inductance characteristics in Fig. 3.6. Additionally, it is not protected by the saturation of the core any more, as can be seen in Fig. 3.7, since its $H_{cJ} = 270 \text{ kA/m}$ is reached before the core saturates. In contrast to the neodymium magnet, H_{cJ} approximately equals H_{cB} , which means that negative B values should be avoided. It should also be noted that the design of the choke with the hard ferrite still presents a low value for l_{gap} , since H_{cJ} is near the minimum H caused by the maximum current at room temperature. This would not be a practical design but serves as an example for comparison. Besides, the description of the *HF 30/26* with a linear permeability is not valid any more for $H < -H_{cB}$ or $H > 0$. This is also an example where the design is limited by H_{cJ} , or $(BH)_{\max}$, and the inductance covers a larger range than needed, which means that only a part of the potential B_{Fe} range is utilized.

3 Biased Chokes

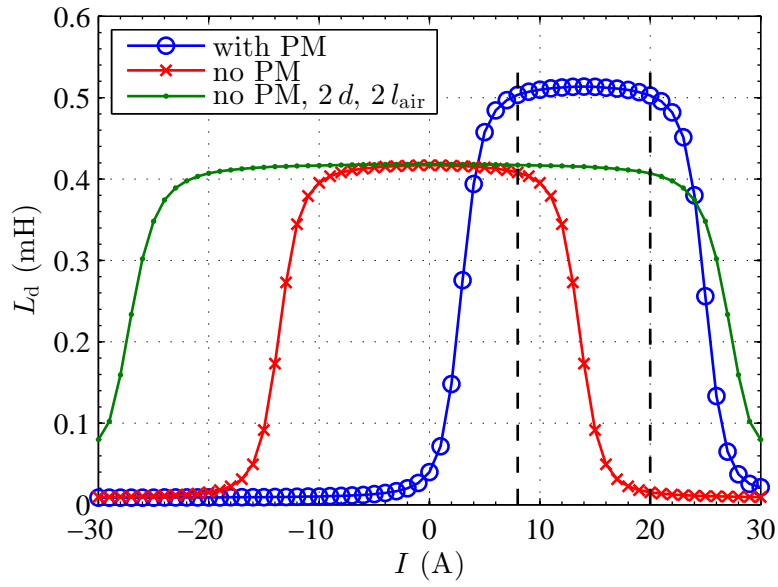


Figure 3.4: Differential inductance of the U-core choke against coil current with PM, without PM, and with doubled cross-section and air gap.

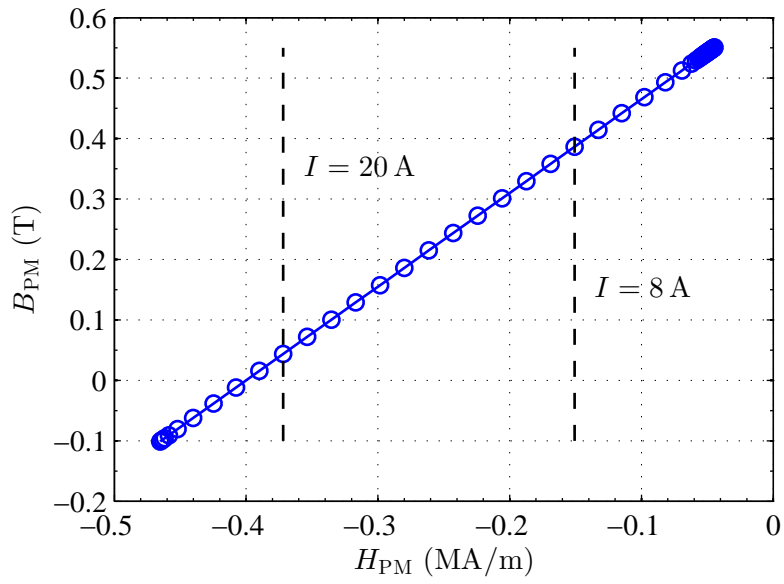


Figure 3.5: Operating characteristics of one PM in the U-core choke at given coil current.

3 Biased Chokes

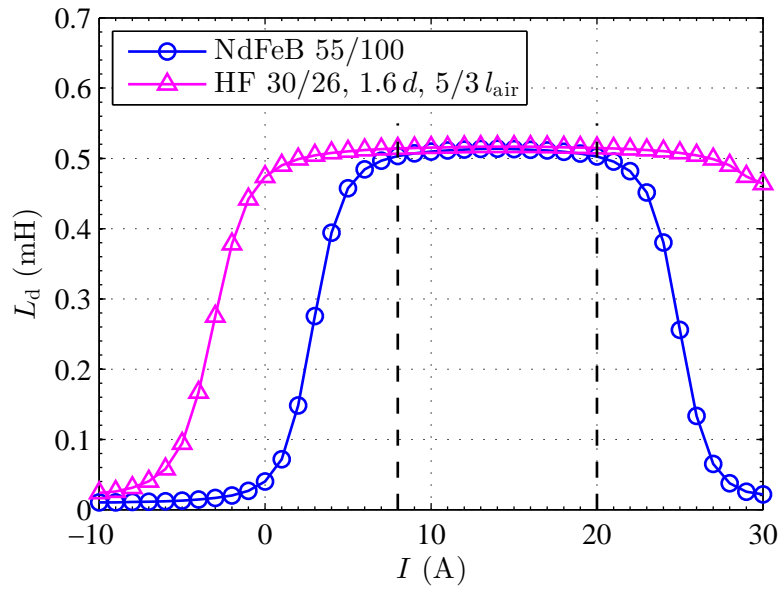


Figure 3.6: Differential inductance of the U-core choke against coil current for 2 different types of PM and dimensions.

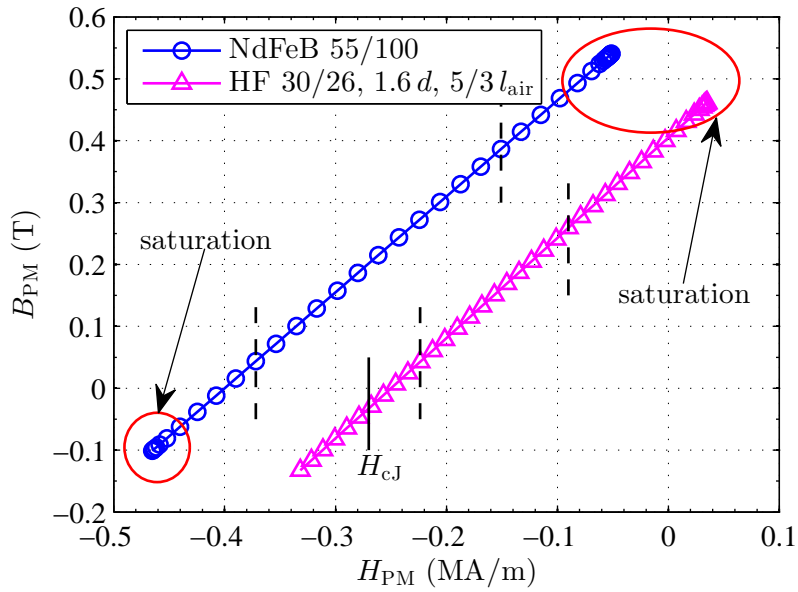


Figure 3.7: Operating characteristics of one PM in the U-core choke for 2 different types of PM and dimensions yielding the same maximum inductance.

3.2 Influence of the Electric Conductivity

When exposing a PM to an alternating magnetic field, the electric conductivity of the PM is a very important property to be considered. It is directly responsible for eddy currents according to Faraday's law (2.2). The electric conductivity causes a damping of the quasistatic equation (2.15), since it is multiplied by the first time derivative of the vector potential. More importantly, the eddy currents cause Joule heating just as any current through a conductive medium. Since the characteristic quantities of PM usually degrade with rising temperature (see e.g. Fig. 2.3), the eddy currents can lead to a malfunction in the application because the design requirements might not be met any more at an elevated temperature. High power applications often require PM with a high $(BH)_{\max}$ in order to achieve a small design size and low mass, but the most powerful magnets, such as rare earth magnets, usually have a high electric conductivity, too.

In order to show the effects on the characteristic quantities of a choke, the example from the previous section is considered. A 3D model of the U-core choke is considered and the results are calculated by FEM, which requires a higher effort for modeling and calculation on the one hand, but has several advantages on the other hand. The field is calculated with the real geometry taken into account, which includes the stray flux and eliminates the need of identifying resistors. The results are more accurate, since the spatial distribution of the field quantities is taken into account. This also means that the distribution of the eddy current density can be visualized. To study the eddy currents while taking the non-linearity of the core material into account, transient simulations are carried out, i.e. solving the system of ODEs (2.24). Two different cases are considered, where a sinusoidal excitation is once applied to reach both positive and negative saturation, and once only in the designed region between $i = 8$ A and $i = 20$ A. In the following, they are referred to as full excitation and designed excitation. The coil current is of the form $i(t) = \hat{I} \sin(2\pi f t) + I_0$, where $\hat{I} = 15$ A and $I_0 = 20$ A in case of the full excitation, and $\hat{I} = 6$ A and $I_0 = 14$ A in case of the designed excitation. For both excitations, the frequency $f = 50$ kHz is chosen. The model is depicted in Fig. 3.8 without the surrounding air and without parts of the coil to give a better overview. As there is a PM in both air gaps, the geometric symmetry can be exploited to model only an eighth of the volume. The geometric symmetry planes are the xy , xz and yz planes, whereas the normal component of \vec{B} is zero on the xy plane and the surface of the surrounding air.

The differential inductance for the full excitation is shown in Fig. 3.9. The initial value of the magnetic vector potential is calculated from a static simulation at I_0 , and its time derivative is initialized with zero. Therefore, the simulation needs some time to reach a steady state, which is why 2 periods of f are simulated. The time step is chosen as $\Delta t = 0.2 \mu\text{s}$, i.e. $T/100$ at $f = 50$ kHz, in order to obtain a small error due to time integration and a good resolution for visualizing the results. The electric conductivity of the PM is once set to zero and once set to $\gamma = 26.3262$ kS/m. This specific value originates from measurements, which is explained in Section 5.3. The corresponding flux density in the geometric center of the PM is shown in Fig. 3.10. It can be observed that the damping leads to a phase difference, which results in a hysteresis-like behavior

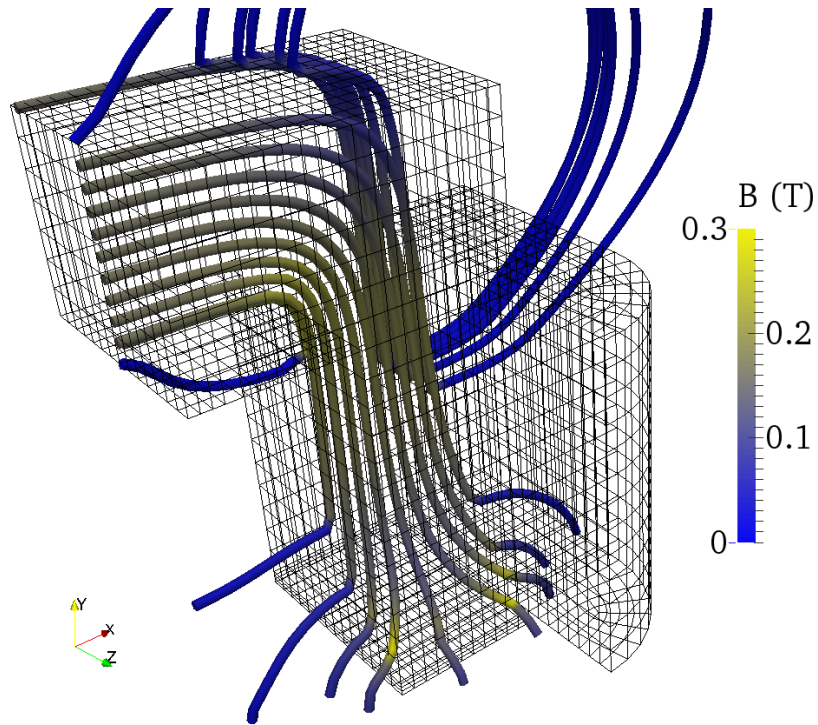


Figure 3.8: Mesh of the U-core choke and flux lines colored by $\|\vec{B}\|$ at $t = 27 \mu\text{s}$ with the designed excitation.

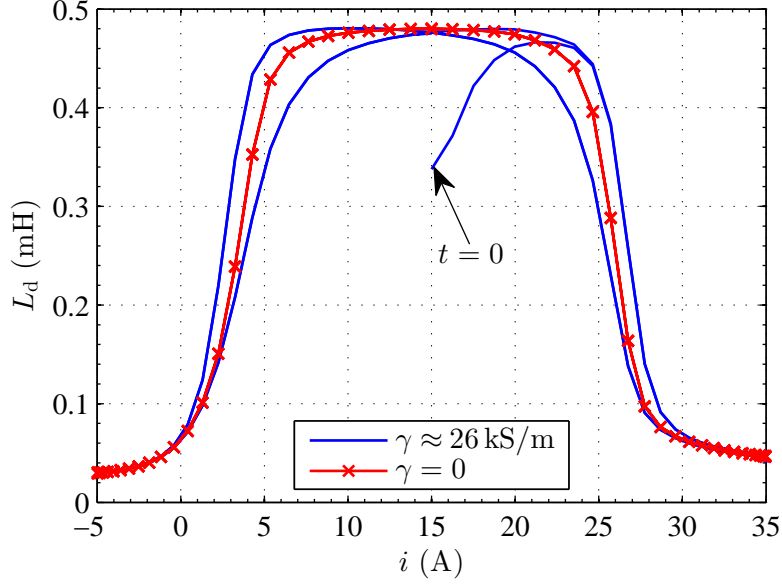


Figure 3.9: Differential inductance of the U-core choke against coil current with and without electrical conductivity in the PM at full excitation.

with respect to the coil current. A similar effect can be observed with the designed excitation, as shown in Figures 3.11 and 3.12. The phase difference causes singularities when calculating L_d , as can be seen at $i = 8$ A and $i = 20$ A in Fig. 3.11. These originate from Δi being close to zero at the extrema of the excitation, and Δi and $\Delta \Psi$ not reaching zero at the same time.

Lastly, the eddy currents are investigated for the designed excitation, since a full excitation would not make sense in an application. The distribution of the eddy current density is shown in Fig. 3.13. As the flux density mainly has a y component, i.e. pointing to the core, the eddy currents circulate in the xz plane. Concerning the heating, the power of the eddy currents has to be calculated, since it is proportional to the Joule heating. The instantaneous power is calculated from the FE simulations as

$$P_{\text{eddy}}(t) = \int_{\Omega} \vec{J}_e \cdot \vec{E}_e dV = \int_{\Omega} \gamma \frac{\partial \vec{A}}{\partial t} \cdot \frac{\partial \vec{A}}{\partial t} dV \quad (3.6)$$

and is displayed in Fig. 3.14. Usually, the mean value of the instantaneous power over a certain period of time is referred to as power. For periodic signals, it is calculated as

$$\bar{P} = \frac{1}{T} \int_{t_0}^{t_0+T} P(t) dt. \quad (3.7)$$

The integral is approximated by the trapezoidal rule and yields $\bar{P}_{\text{eddy,PM}} \approx 53.56$ W over the last period of $i(t)$, i.e. the last $20 \mu\text{s}$. This is already a considerable value compared

3 Biased Chokes

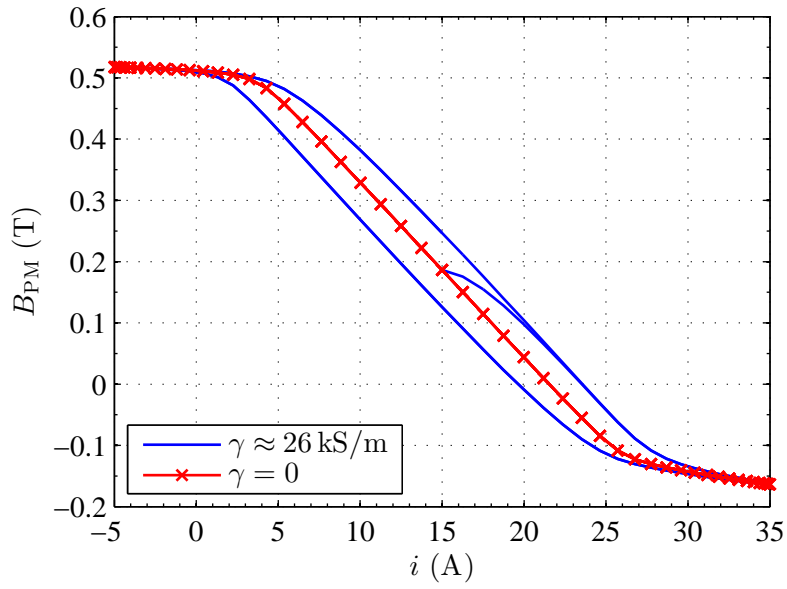


Figure 3.10: Operating characteristics of one PM in the U-core choke with and without electrical conductivity in the PM at full excitation.

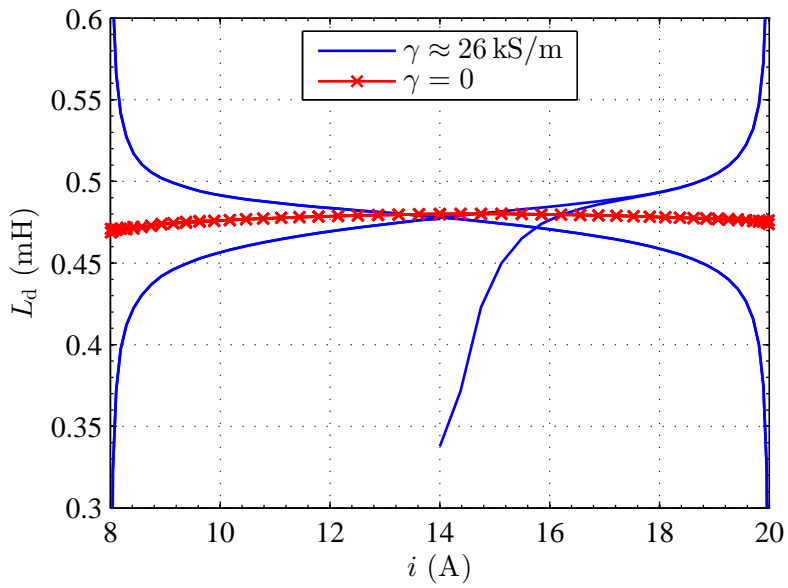


Figure 3.11: Differential inductance of the U-core choke against coil current with and without electrical conductivity in the PM for the designed current range.

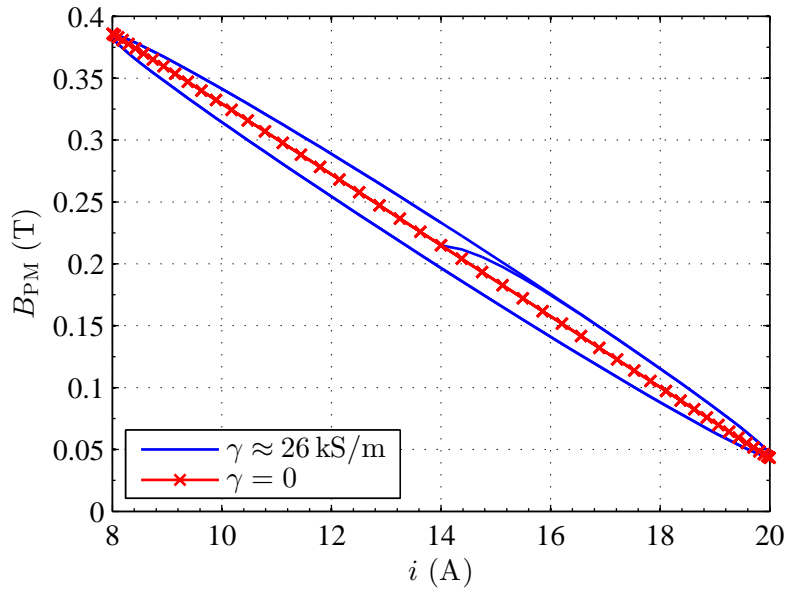


Figure 3.12: Operating characteristics of one PM in the U-core choke with and without electrical conductivity in the PM for the designed current range.

to e.g. an incandescent light bulb. The power shown is already corrected according to the symmetries, i.e. the result obtained by (3.6) is multiplied by 4, since only a fourth of the volume of one PM is modeled.

3 Biased Chokes

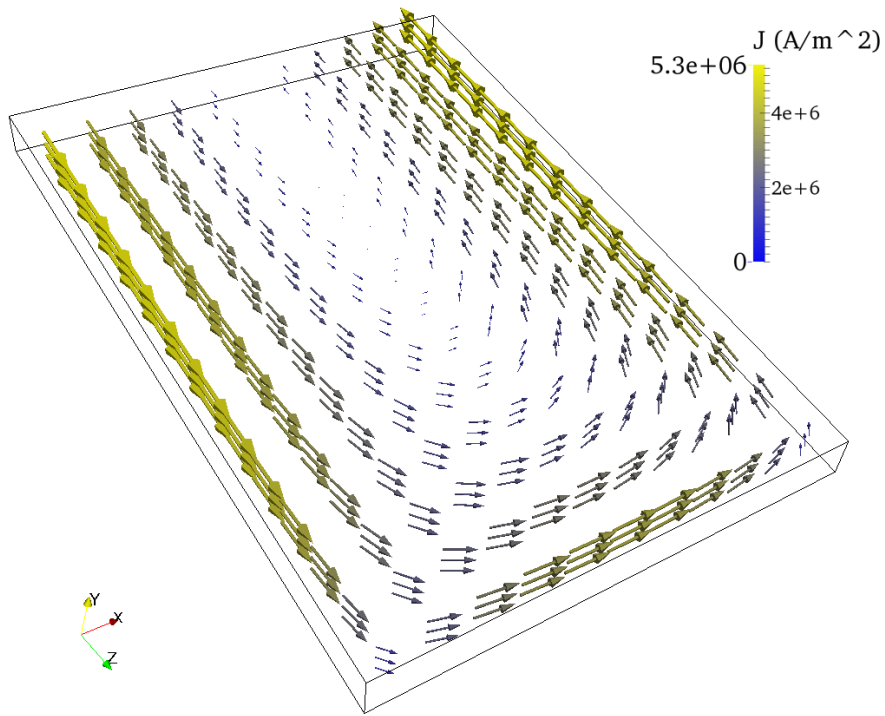


Figure 3.13: Eddy current density at $t = 40 \mu\text{s}$ in one PM of the U-core choke excited in the designed current range.

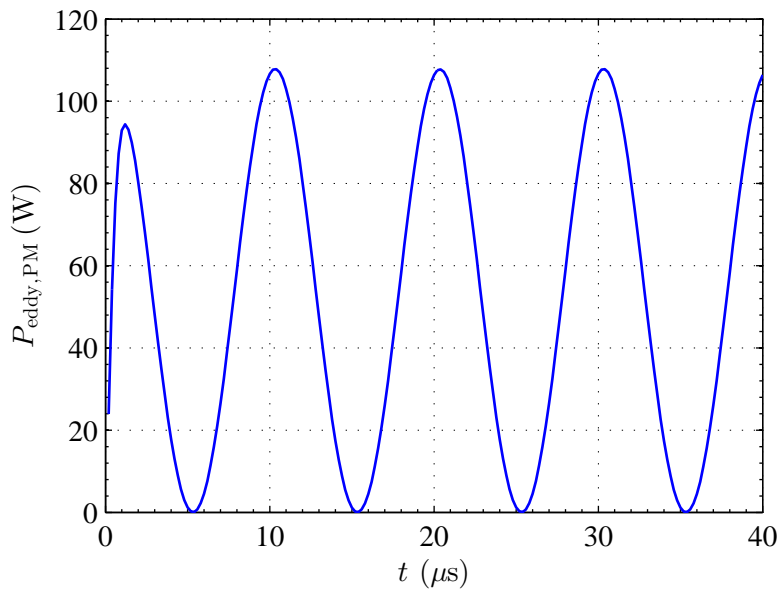


Figure 3.14: Instantaneous power of the eddy currents in one PM of the U-core choke excited in the designed current range.

4 Characterization of Magnetic Properties

The common procedure for the characterization of magnetically hard materials is defined in the IEC 60404-5 (see Chapter 1, Fig. 1.7). However, the bulky setups lead to large inductances, which makes a complete characterization not feasible at higher frequencies. Additionally, the samples under test should have a smallest dimension of 1.5 mm, whereas the standard suggests a minimum dimension of 5 mm. The samples are magnetized in the direction of this shortest edge. As mentioned in the previous chapter, such geometries are needed to fit the application. In order to characterize those samples and to keep track of the development of their main properties after and during stress tests, a non-standard method has to be applied. It is important to characterize the samples as used in the application, since the magnetic properties can vary due to imperfections, geometric tolerances and non-ideal magnetizations. For these reasons, the magnetic behavior can differ from standard sample geometries, like e.g. cylinder-shaped samples.

The use of highly specialized hardware, e.g. vibrating sample (VSM) and pulsed field magnetometers (PFM), is mentioned in Chapter 1 and applied in e.g. [8] or [19]. These measurement setups usually differ from the actual applications, e.g. dynamic loudspeakers, biased inductors, or electric machines. Those applications have in common that the magnetic flux through the PM mainly or partly has an alternating component. As shown in the previous chapter, the PM has to be operated in its linear region, i.e. where the permeability can be described as a linear function. Otherwise, there is the risk of demagnetization or the requirements are not met any more. In this region, the most important characteristic properties of a PM are its remanence and permeability. Actually, the complete hysteresis curve is not of interest for the application. It is of interest how much flux density the PM can provide as a source, or its source characteristics, more generally. Combining the operating range from the application and the restriction to the main properties, it is interesting to contemplate a method to determine those main quantities by measuring only a part of the characteristic curve of the PM. The main advantage is that less field intensity is needed, which means less electric current through the coils and less power, which is beneficial with respect to the cost of the equipment. Inversely to the measurement, it can also be used to magnetically load the PM and perform stress tests, apart from the application.

Therefore, a method is developed to characterize the permeability and remanence of a PM from a part of its measured operating curve. The applicability is demonstrated by measurements with a measurement setup tailored to the samples of a specific geometry, which does not mean that the actual method is restricted to one geometry. Nevertheless, practical considerations are presented regarding the design of the setup. Moreover, the effects of eddy currents are discussed, since the PM are operated at frequencies up to 20 kHz in applications such as loudspeakers and power inverters.

The method aims at determining the operating point in the magnetic circuit with the sample under test. The main difficulty is that the direct measurement of characteristic quantities is not possible in most cases. The magnetic flux density can be measured by e.g. a Hall probe, but it is not possible to place a sensor inside a PM without destroying it or at least influencing the field distribution. Therefore, the magnetic field quantities are mostly measured by coils, which can only pick up alternating fields. Hence, only the change of the quantities is known, but not their point of origin, which is the operating point. The presented approach utilizes a magnetic equivalent circuit to determine the remanence of a PM, which requires the operating point. In contrast to the remanence, the permeability can be calculated directly from the alternating quantities.

The measurement setup is based on a closed-circuit measurement principle. Since the magnetic core material has a high permeability, a negligible electric conductivity, but a low saturation, the computer-aided design of the setup becomes important. As the quantities are split into alternating and direct components, the magnetic circuit leads to more unknowns than equations. Therefore, FE simulations are even required for calibration. The calibration offset is the only quantity obtained from simulations, whereas the rest of the unknowns is identified directly from the measurements. Similarly to many inverse problems in material characterization, see e.g. [27], [32], this approach is a combination of measurements and simulation. The principle and some practical information were already presented in [29] and [30]. In this thesis, an extended and more detailed description of the method is provided.

4.1 Design of a Measurement Setup

Similarly to the IEC 60404-5, the measurement setup is based on a closed magnetic circuit with excitation coils. However, it features two air gaps equal in length, as depicted in Fig. 4.1. A Hall probe is placed inside one air gap in order to be able to measure the direct component of the magnetic flux density. The main flux, the flux through the PM, and the flux alongside the PM are measured by sensing coils. The sensing coil alongside the PM encloses only air, which allows for directly measuring the mean magnetic field intensity close to the PM. The field intensity is ideally the same inside the PM and close to the PM if using a core wider than the sample. As the standard principle, the measurement setup utilizes the tangential continuity of H to indirectly measure H inside the PM. Another feature of the setup is that it is designed for the operation at temperature up to and above the maximum operating temperature of the PM.

The material of two U-cores is chosen as a ferrite material, i.e. the same as used in the application. On the one hand, this material is suited for higher frequencies. On the other hand, it limits the magnetic flux density in the circuit due to its low saturation compared to the remanence B_r of the PM. As shown in Chapter 3, the saturation provides a protection of the PM. For the measurement, this means that only a part of the PM characteristic can be measured. Additionally, the coercive field, or the $(BH)_{\max}$, shifts the window, where H can be measured. The measurable range is defined, where H is

4 Characterization of Magnetic Properties

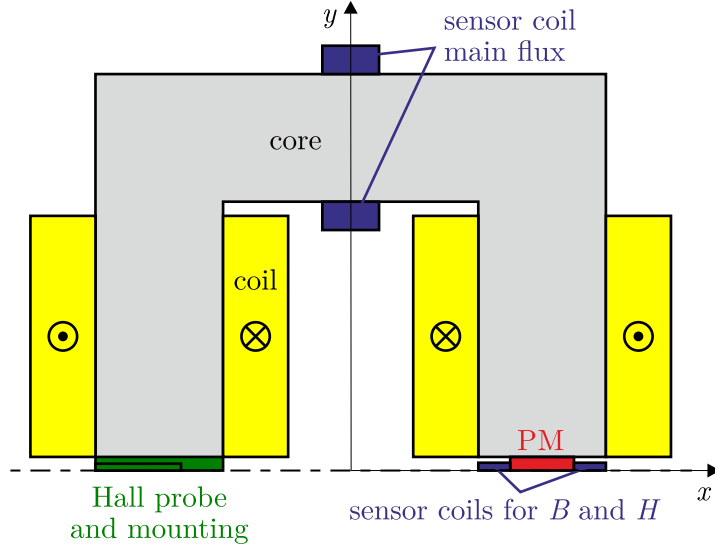


Figure 4.1: Draft of the cross-section of the measurement setup with the xz plane as symmetry plane.

the same in the PM and close to it. With the chosen core material, B_r is outside this window, i.e. the measured H differs from H_{PM} at $H = 0$. However, this is neither a reason for the development of the identification method, nor a limitation of the method.

Due to the saturation of the core combined with the measurement of H , FE simulations are important for the design of the setup. The saturation and the remanence determine both the operating range and the measurable range. Additionally, the stray flux becomes considerably high in setups with relatively large air gaps, as shown in e.g. [28]. 2D simulations would reduce the modeling and computational effort, but they do not take into account the stray field in the third direction. In this case, they yield about 10% more flux through the core compared to 3D results, which is not acceptable. The 3D model is shown in Fig. 4.2 with details of the mesh and without the surrounding air volume.

As mentioned, the measurement of H in the PM is basically the most important criterion for the design. Thus, the air gap with the sample under test is of special interest regarding the distribution of the field intensity, as shown in Fig. 4.3. This gap can also be seen in the photograph in Fig. 4.4 without the upper core. On the left-hand side, the Hall probe and the mounting are visible and the measurement coils for B and H on the right-hand side. The mounting is made of polyether ether ketone (PEEK) to withstand higher temperatures. Additionally, it determines the height of the gap and makes the alignment of the cores easier. The samples under test are neodymium magnets of the type *NdFeB 55/100 pw*, as also used in the previous chapter. The dimensions are the same, i.e. $8.3 \text{ mm} \times 25 \text{ mm} \times 1.5 \text{ mm}$, and the same ferrite material is used too, i.e. *3C90*. In order to find a geometry suitable for the measurement of H , the width of the core w_C is varied as multiples of the width of the PM $w_{PM} = 8.3 \text{ mm}$. The z

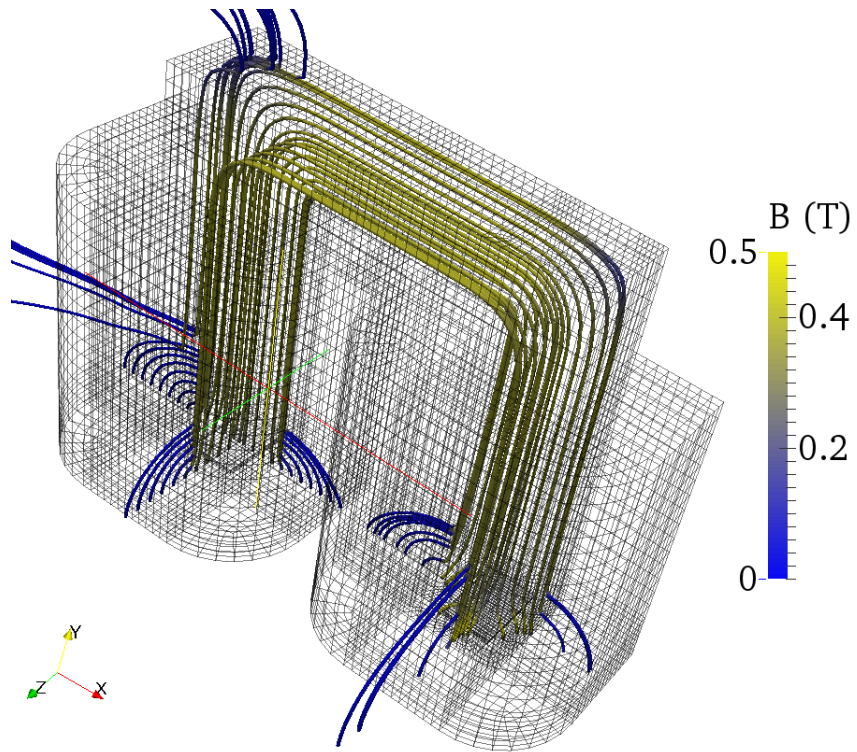


Figure 4.2: Mesh of the model of the measurement setup and simulated flux lines colored by $\|\vec{B}\|$ at a static excitation current of $I = 8$ A.

4 Characterization of Magnetic Properties

dimension of the core is specified as $25 \text{ mm} + w_C - w_{\text{PM}}$, which results in a constant width of the air gap around the PM in x and z direction. The total width and height of one U-core is chosen as $4 w_C \times 4 w_C$. The advantage of a larger core is that there is more space for placing a sensing coil and there is a larger area with a homogeneous field distribution. The disadvantage is that the inductance rises with increasing w_C . Since the dimensions are rather small, the manufacturing of the sensing coils has to be taken into consideration. The coils depicted in Fig. 4.4 each have 10 turns and can be dismantled to be calibrated in a Helmholtz coil. Due to the relatively high stray flux, the coils must have enough turns to reduce the error from the wiring, apart from improving the signal-to-noise ratio. Therefore, the wiring is additionally twisted. Hence, choosing a core width is not a purely mathematical optimization problem, but it is also a matter of design and manufacturing. From the results of $w_C = k w_{\text{PM}}$, $k \in \{1, 1.5, 2, 4, 6\}$, $k = 2$ is chosen, for which the distribution of the y component of \vec{H} along the x axis is shown in Fig. 4.5 for different static excitation currents. The excitation is distributed over 4 coils with 28 turns each. Since they are connected in series, this results in a total of $N = 112$ turns. From these results, a range for the measurement of H can be determined. Larger cores yield similar results, whereas the designs with $k \in \{1, 1.5\}$ are not practicable due to the rapid decrease of $\|\vec{H}\|$ with increasing distance from the PM.

For the same situation, the difference between the field intensity in the center of the PM and the center of the surrounding airgap is shown in Fig. 4.6 against the coil current. The center of the PM is located at $(x_2 + x_3)/2$ and the value of H alongside the PM is calculated as the mean of H at the positions $(x_1 + x_2)/2$ and $(x_3 + x_4)/2$, according to Fig. 4.3. This difference, which determines the measurable range, can be investigated for different combinations of core and PM materials. For a better comparability, the difference is plotted against H in the PM and normalized to the coercive field of the PM. The first combination represents the designed measurement setup. For the second combination, a PM with a higher $(BH)_{\text{max}}$ is chosen. The effect is that there is no point at which the measured H equals H_{PM} . Therefore, a core material with a higher saturation is chosen for the third combination. *KM 60* denotes the material *KoolMu 60* produced by *Magnetics*, which is a powder-core with a negligible electric conductivity. However, its high saturation is traded off for a low permeability, which also leads to a difference between the field intensities. For the fourth case, a soft magnetic cobalt iron alloy is considered, namely *VACOFLUX 50* manufactured by *Vacuumschmelze GmbH & Co. KG*. It features a very high permeability and a high saturation, but also a high electric conductivity. Therefore, the typical values of 0.35 mm laminated sheet-cores are used for the simulation. The good magnetic properties of this core material lead to a large measurable range for the PM with a high $(BH)_{\text{max}}$.

The flux density in the PM is another important aspect of the design, considering the magnetic load of the PM. As for the application, the flux density is considered with respect to the coil current, as shown in Fig. 4.8. The linear permeability model of the PM is still valid, since B_{PM} neither exceeds B_r nor falls to a value corresponding to H_{cJ} in the B against H curve (see Fig. 2.3).

Finally, the inductance of the setup is of interest regarding tests at higher frequencies. The differential inductance of the measurement setup is shown in Fig. 4.9. For the

4 Characterization of Magnetic Properties

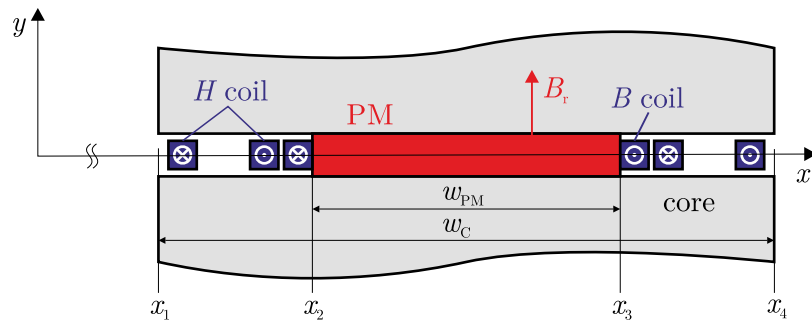


Figure 4.3: Cross-section of the gap with the sample under test, the measurement coils and definition of x_1 to x_4 for the evaluation of the design.

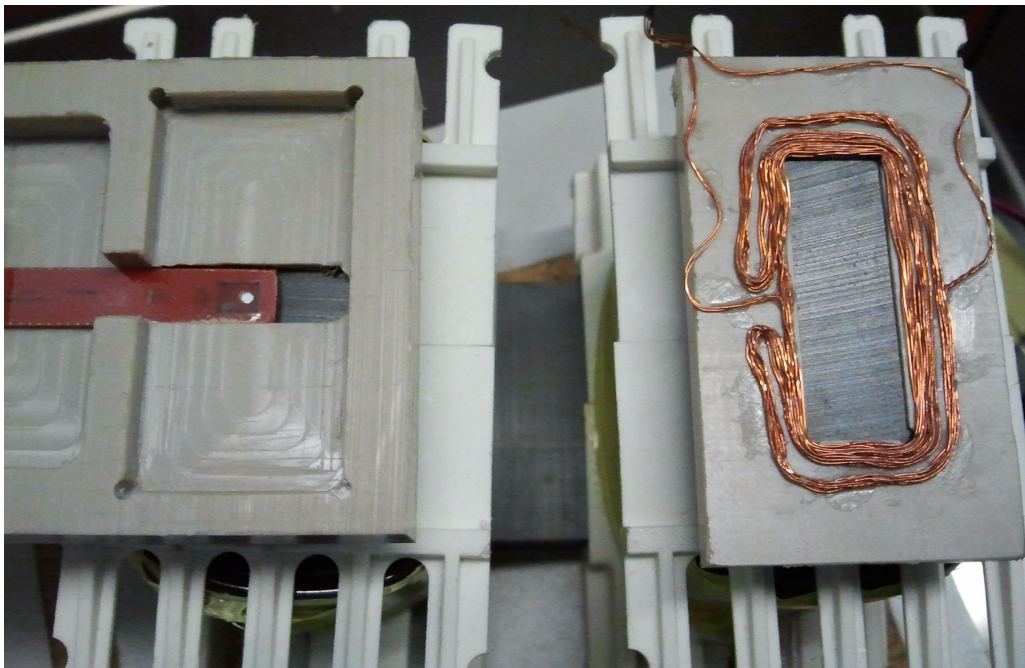


Figure 4.4: Photograph of the measurement setup with the upper core removed.

4 Characterization of Magnetic Properties

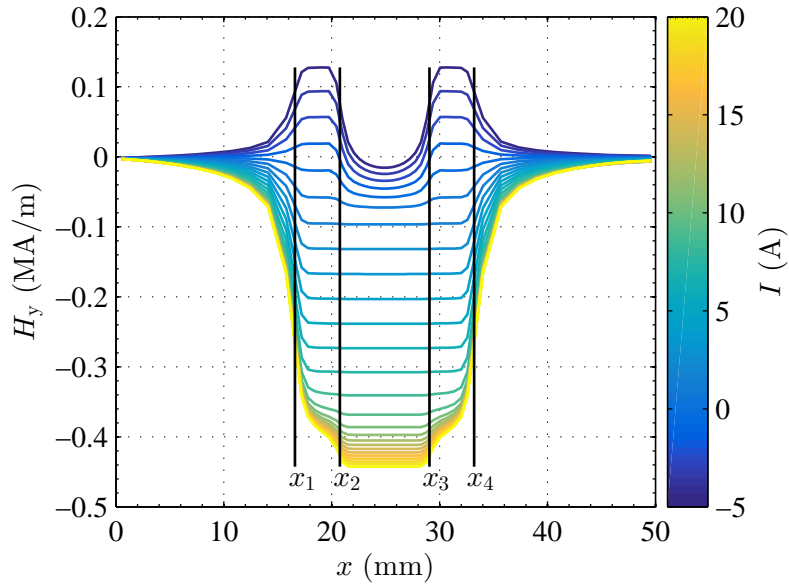


Figure 4.5: Simulated distribution of the y component of \vec{H} along the x axis for different static excitation currents I .

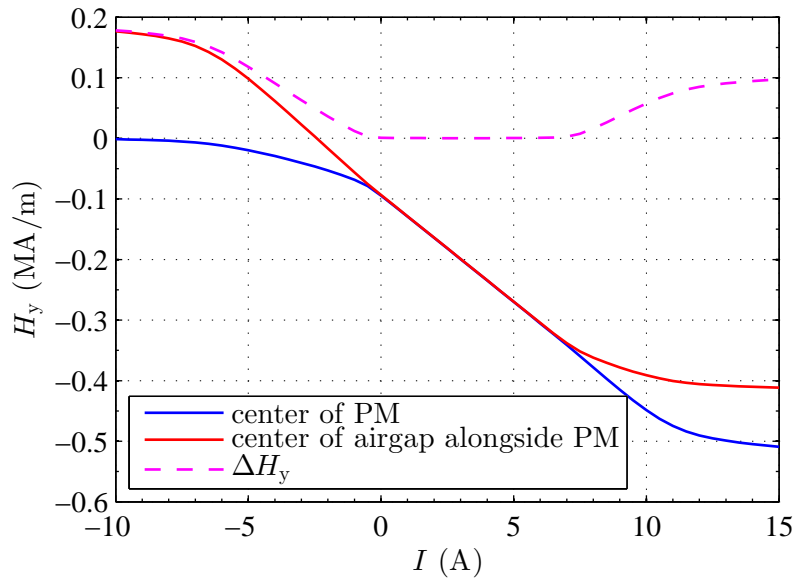


Figure 4.6: Simulated y component of \vec{H} in the PM and alongside the PM against different static excitation currents I with the core material *3C90* and a PM of type *NdFeB 55/100 pw*.

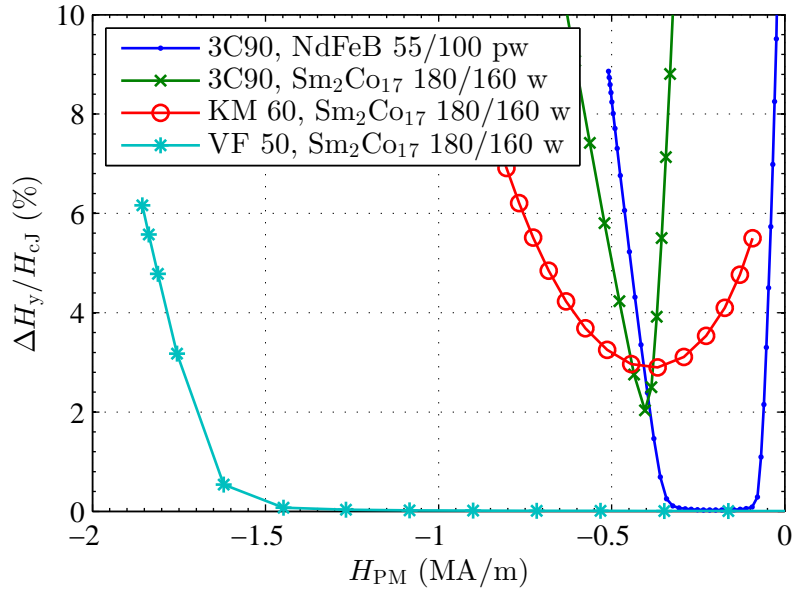


Figure 4.7: Difference of H_y in the PM and alongside the PM for different core and PM material combinations.

calculation, (2.41) is approximated by the central difference and by the forward and backward difference at the beginning and end, respectively. For the results of Figures 4.8 and 4.9, a coil current of $i = 17.5 \text{ A} \sin(2\pi 1 \text{ Hz } t) + 7.5 \text{ A}$ was specified. The use of the forward and backward difference is the reason for the artifacts at $i = 7.5 \text{ A}$ in Fig. 4.9. The plausibility of the maximum inductance can be checked with relation (3.1) and the results of the U-core choke in Chapter 3. Neglecting the longer mean path through the core and the permeability of the PM, the measurement setup has a doubled cross-section and twice as many turns compared to the U-core choke. The doubled cross-section leads to a halved magnetic resistance and the influence of the number of turns is quadratic, which yields an inductance about eight times as large as the one of the U-core choke.

4.2 Identification Procedure

The first information is obtained by the three sensing coils measuring the main flux through the core, the flux through the PM, and the flux in the air gap surrounding the PM. They are calculated as

$$\hat{\Phi} = \frac{1}{N} \int_0^{t_{\text{end}}} (u(t) - \bar{u}) dt, \quad (4.1)$$

where $\hat{\Phi}$ denotes the alternating component of Φ , u the induced electric voltage, \bar{u} the mean value of the induced voltage over the whole time span and N the number of turns

4 Characterization of Magnetic Properties

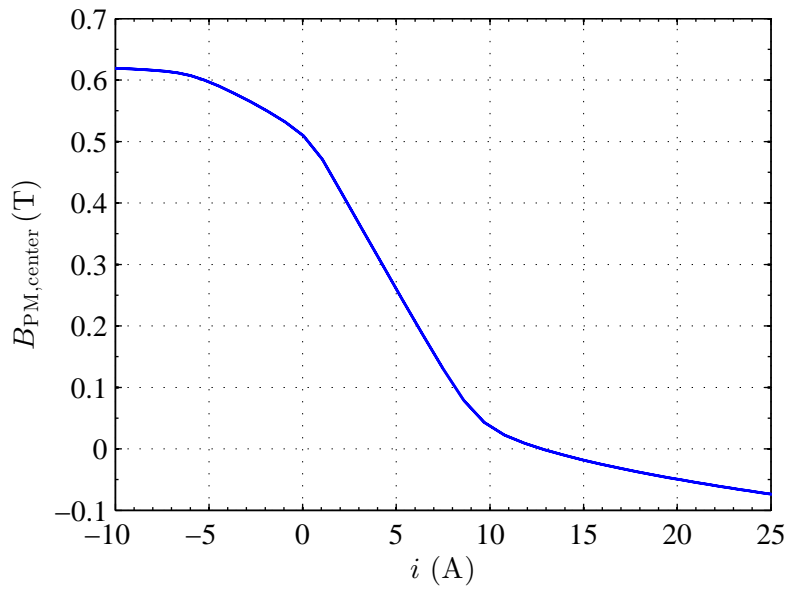


Figure 4.8: Magnetic flux density in the geometric center of the PM against the coil current i .

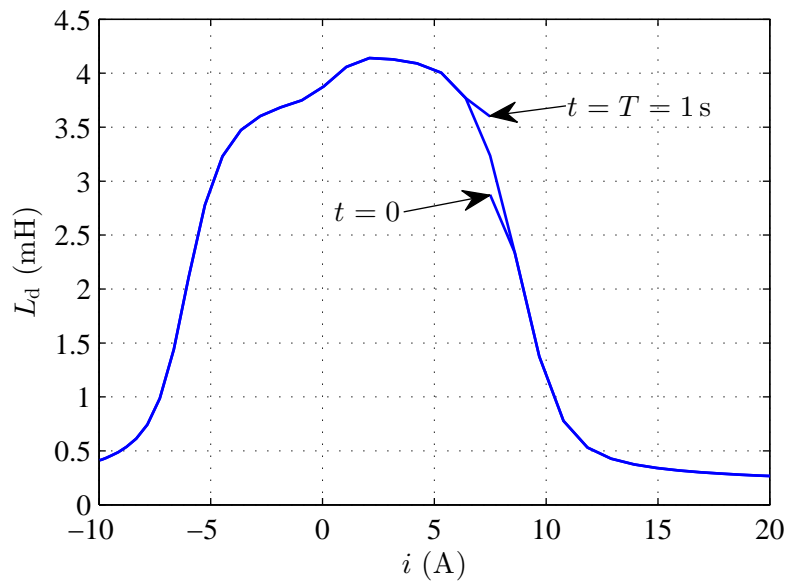


Figure 4.9: Differential inductance of the measurement setup against the coil current i .

4 Characterization of Magnetic Properties

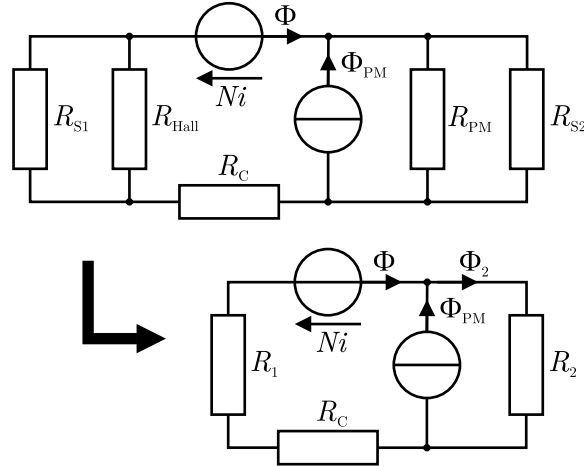


Figure 4.10: Magnetic equivalent circuit of the measurement setup and effective resistors R_1 and R_2 for the identification procedure.

of the corresponding coil. The subtraction of \bar{u} prevents a drift of the result, since the alternating quantities are generally not centered around zero and not purely sinusoidal due to saturation effects. The integral is approximated by the trapezoidal rule for the time-discrete measurement data.

In order to determine the operating point, a magnetic equivalent circuit is considered as depicted in Fig. 4.10. The PM is modeled as a non-ideal flux source with the internal resistance R_{PM} and stray fluxes are modeled by the resistors R_{S1} and R_{S2} . R_{Hall} describes the air gap with the Hall probe, and the core is represented by R_C . The excitation coils are modeled as an ideal magnetic voltage source Ni .

The first step is to determine the permeability of the PM, which can be measured directly by the two sensing coils around the sample. Since the H coil encloses only air, the field intensity can be obtained from the flux as $\hat{H}_2 = \hat{\Phi}_{Hcoil} / (\mu_0 A_{Hcoil})$. Concerning the notation, \hat{H}_2 denotes the alternating component of H_2 , which is the field intensity in the magnetic resistor R_2 . Γ_{Hcoil} and Γ_{Bcoil} denote the effective cross-sections of the coils, which are calibrated in a Helmholtz coil. According to the standard IEC 60404-5, the flux through the PM is corrected because the coil does not perfectly enclose the PM, which results in the mean flux density

$$\hat{B}_{PM} = \frac{\hat{\Phi}_{Bcoil} - \mu_0 \hat{H}_2 (\Gamma_{Bcoil} - \Gamma_{PM})}{\Gamma_{PM}}. \quad (4.2)$$

From \hat{B}_{PM} and \hat{H}_2 , the permeability of the PM can be determined directly. However, the operating point is still unknown, which is why μ is calculated from a 1st order polynomial fit as $\hat{B}_{PM} = \mu \hat{H}_2 + B_0$. The offset B_0 has to be taken into account for the fit, but it is not considered for further calculations, for similar reasons as \bar{u} has to be subtracted in (4.1). Since the measurement of H is tied to the linear region of the core, all quantities are assumed to be linear in the valid range of H . Regarding the signals

4 Characterization of Magnetic Properties

for \hat{B}_{PM} and \hat{H}_2 , sinusoidal functions are considered, which have an offset, but which are undistorted by the saturation. If the excitation is of this form, it can be utilized to fit sinusoidal functions to the measured signals and only data in the valid range of H is used for the fit. However, as mentioned, the operating point is still unknown. Therefore, prior knowledge of the valid range of H cannot be applied in this case, because only alternating quantities are available. Before the polynomial fit of μ , the phase difference between \hat{H}_2 and \hat{B}_{PM} has to be corrected first, which can be achieved by searching for their zero-crossings. The same applies to $\hat{\Phi}_{\text{Bcoil}}$ and \hat{H}_2 in (4.2).

The next step in identifying B_r is to calculate the magnetic resistors from the alternating quantities as

$$R_{\text{tot}} = R_1 + R_2 + R_C = \frac{N \hat{I}}{\hat{\Phi}}, \quad R_2 = \frac{\hat{H}_2 l_2}{\hat{\Phi}}, \quad (4.3)$$

where l_2 denotes the effective length associated with R_2 , i.e. the height of the PM and the air gap. The advantage of identifying those effective resistors is that the setup is identified without making assumptions about most of the geometry and materials, especially the core material. Unlike the identification of μ , only the amplitudes of the sinusoidal signals are needed, whereas the phase difference is not of interest. Since only alternating quantities are involved in (4.3), the static (time-independent) flux source can be neglected (see Fig. 4.10). However, it is this flux source we are interested in, and the resistors can be used for identifying it. For this purpose, the total main flux Φ has to be calculated, not only its alternating component. This can be achieved by utilizing the relation between the main flux and the flux density measured by the Hall probe. However, the relation between the alternating components is linear, which is not the case for the total flux including the static component. Therefore, this relation is formulated as

$$\alpha = -\hat{\Phi}/\hat{B}_{\text{Hall}}, \quad \Phi = \alpha B_{\text{Hall}} + \beta, \quad (4.4)$$

where β is a calibration offset obtained from 3D FE simulations, which is explained in more detail after the explanation of the identification of B_r . Since the direct component has to be modeled including this offset, there are too many unknowns to solve the magnetic equivalent circuit. In general, β depends on the remanence, the coil current and the permeability. The factor α can simply be identified from the amplitudes.

With the help of relation (4.4), the static main flux can be calculated as

$$\Phi_0 = \alpha B_{\text{Hall}}|_{i=0} + \beta|_{i=0} = \alpha B_{\text{Hall}}|_{i=0} + \beta_0. \quad (4.5)$$

If using a periodic excitation, it can be obtained by e.g. taking the mean at several zero crossings of i . Finally, the flux source, i.e. the PM and its B_r , can be identified as

$$\Phi_{\text{PM}} = -\frac{\Phi_0 R_{\text{tot}}}{R_2}, \quad B_r = \frac{\Phi_{\text{PM}}}{\Gamma_{\text{PM}}}. \quad (4.6)$$

In the following, the calibration offset is explained in more detail. Considering (4.5), β is actually only needed at $i = 0$ for the identification. For all presented results, it is

4 Characterization of Magnetic Properties

modeled as the 2nd order polynomial

$$\beta_0(B_r) = a_2 B_r^2 + a_1 B_r + a_0 \quad (4.7)$$

and is fitted from simulation results for several values of B_r around the nominal remanence of the samples. These values have to include variations from the magnetization process as well as lower values, which are expected to occur after stress tests and during temperature variations. From the simulations, the main flux is calculated on the cross-section enclosed by the corresponding sensing coil at $i = 0$. The flux density B_{Hall} can be taken from the center of the air gap, since the flux density is constant over nearly the whole air gap. If the flux is considered at different values of i , the factor α can also be calculated by fitting a first-order polynomial to the obtained value pairs of B_{Hall} and Φ . The calculated α can be compared to measured values of α for reasons of verification. During the identification procedure, α is identified from the measurements, which means that it takes into account the real geometry and material parameters from the measurement, in contrast to β . Therefore, only β remains as kind of an external calibration parameter. The parameter α usually shows a linear behavior, since the relation between the fluxes through the air gap and through the core is nearly constant, even if the core saturates, as shown e.g. in [28]. β also shows a nearly linear behavior with respect to the remanence, if the core is not highly saturated at multiple locations. Using a non-linear model like (4.7) for β , the calculation of the fluxes and B_r (4.5) and (4.6) can be combined in order to formulate the problem of finding B_r as finding the root of

$$f(B_r) := \frac{R_{\text{tot}}}{R_2 \Gamma_{\text{PM}}} (\alpha B_{\text{Hall}}|_{i=0} + \beta_0(B_r)) + B_r. \quad (4.8)$$

This problem can be solved e.g. by applying Newton's method using the nominal remanence as a starting value. In case of the 2nd order polynomial (4.7), the calculation of the derivative needed for Newton's method is simple or even unnecessary, since there is a closed-form solution.

According to (4.7), the offset at $i = 0$ is assumed to depend only on the remanence. As mentioned, it also depends on the permeability in general, since it can be understood as offset flux of the circuit. However, the influence of the permeability of the PM is very low in this specific setup, as can be seen in Fig. 4.11. Taking into account the dependence on μ affected the presented results by merely a maximum of 0.05 %.

4.3 Application and Verification

As described in Sections 4.1 and 4.2, the measurement setup is used to characterize plastic-bonded neodymium magnets combined with the presented identification procedure. In order to demonstrate the effect of the valid range of H , a sample is identified applying a higher excitation current than needed, which leads to an identified characteristic curve as shown in Fig. 4.12. It is important to note that the saturation effects shown do not correspond to a saturation of the sample. They are the result of the measurable range of H . The load resistor R_L is calculated from the equivalent circuit shown

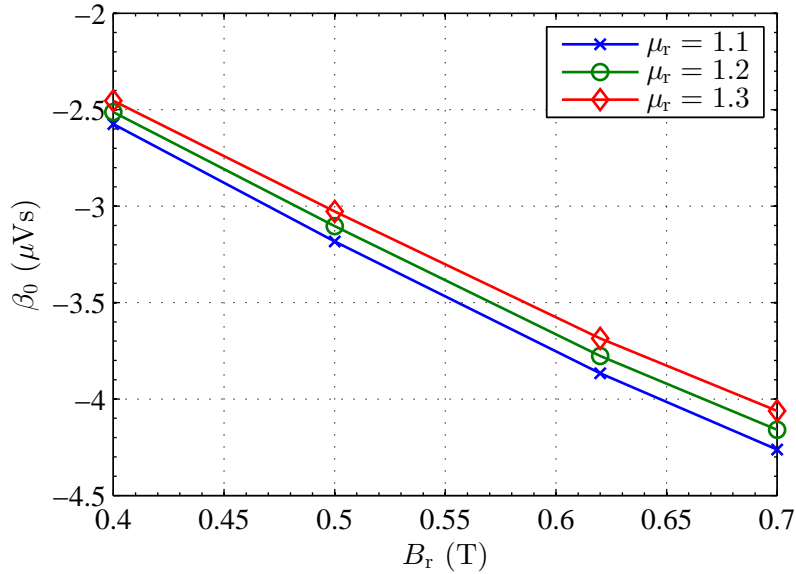


Figure 4.11: Calibration offset β_0 obtained from 3D FE simulations at different remanences and permeabilities.

in Fig. 4.10. This is the resistance which the PM would be loaded by, if the setup was linear at $i = 0$. The load resistor and the operating point are good examples of how the identification method works. In principle, the method pretends that the circuit is linear. In order to calculate R_L , the effective resistor R_2 is split up into the resistors R_{PM} and R_{S2} from the original circuit and the result is calculated as $R_L = (R_1 + R_C) \parallel R_{S2}$.

Although the electric conductivity of the samples is low compared to sintered PM, the effects of higher frequencies are investigated, not least because the eddy currents in the PM are not the only reason for phase differences in the measurement system. After all, the measurement setup must also be viewed as an electric circuit, where the current and the voltage are shifted due to the inductance. However, the eddy currents are a problem for the characterization in general. As an example, a correction of eddy currents is discussed in [22] for the pulsed field magnetometry (PFM) based on the field at different pulse durations. In this measurement setup, the identification of the effective resistors without the phase shift is expected to have a similar effect of correction.

The following experiment demonstrates the application at different frequencies. The excitation current is of the form $i = \hat{I} \sin(2\pi f t) + I_0$, where \hat{I} denotes the amplitude. The alternating part is required for the sensing coils to work, and the offset I_0 is responsible for reaching the measurable range of H . Additionally, the current has to have zero crossings for the evaluation. For the following results, currents with different frequencies are applied with constant $I_0 = 2.25$ A and $\hat{I} = 2.75$ A for all cases. The results are shown in Tab. 4.1, where 2 kHz marks the voltage limit of the power amplifier in use, due to the high inductance of the setup. Nevertheless, the identification yields consistent results up to 2 kHz. The effects on the measurement signals are shown in Figures 4.13 and 4.14,

4 Characterization of Magnetic Properties

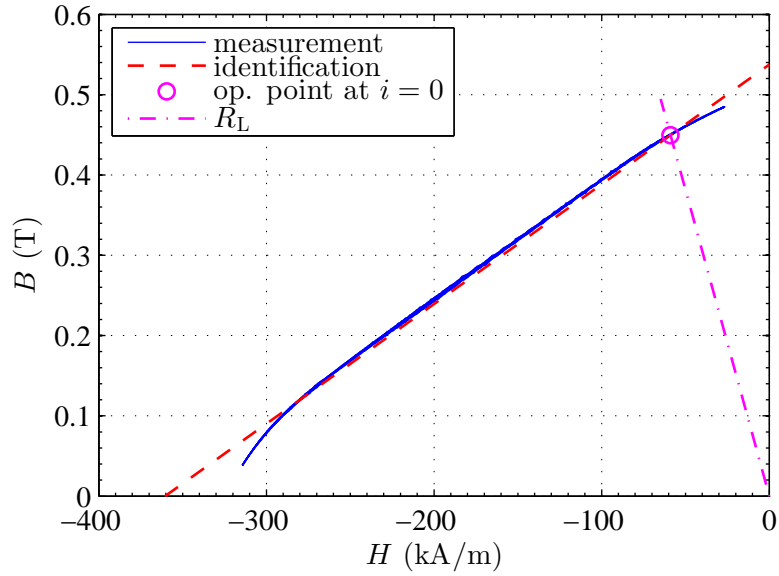


Figure 4.12: Example characterization of a neodymium sample showing the limits of the measurable range of H .

f (Hz)	μ_r	B_r (mT)
0.5	1.1866	535.38
1	1.1848	535.75
10	1.1855	533.78
100	1.1882	534.43
1000	1.1858	532.55
2000	1.1855	535.65

Table 4.1: Results of one sample for different frequencies.

which display the characteristic curves of the identified magnetic resistors at 1 Hz and 2 kHz. Due to neglecting the phase shifts, the identification yields the correct resistor characteristics.

Thus far, the influence of the temperature has not been considered. As mentioned, the parts of the measurement setup are selected to withstand temperatures above the maximum operating temperature of the samples. Therefore, a series of measurements at higher temperatures is presented, where the whole measurement setup was placed inside a thermal box. In this case, the measured signals of the sensing coils reveal more about the functionality of the measurement setup and the identification method, as shown in Fig. 4.15. At higher temperatures, the magnetic properties of the ferrite core degrade, too. Since the method requires a measurable range of H and at least a small linear region, there is also a maximum temperature for the setup. A small linear region can still be observed at 150.5°C, where reliable results are obtained. For comparison, the

4 Characterization of Magnetic Properties

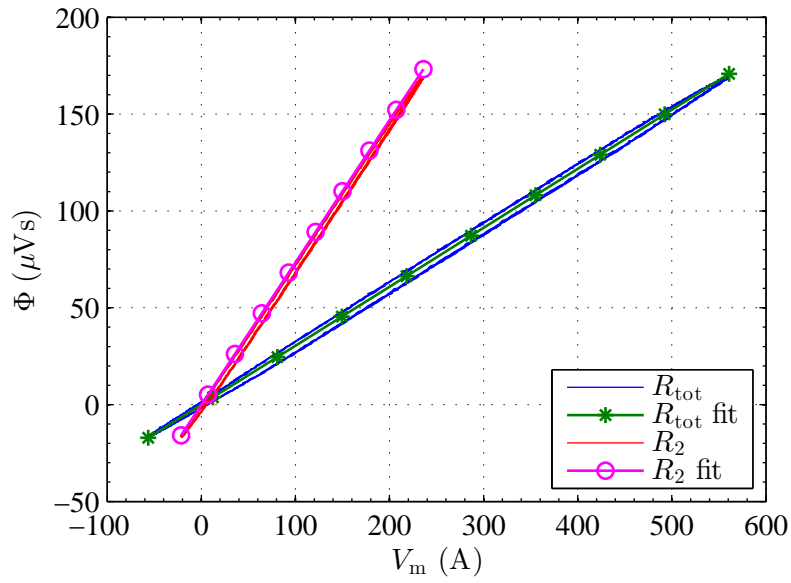


Figure 4.13: Identified magnetic resistors at 1 Hz.

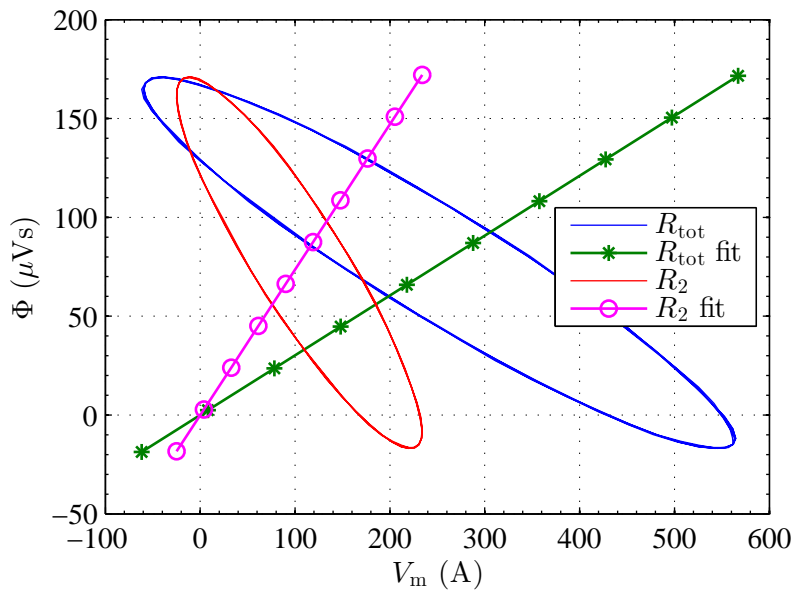


Figure 4.14: Identified magnetic resistors at 2 kHz.

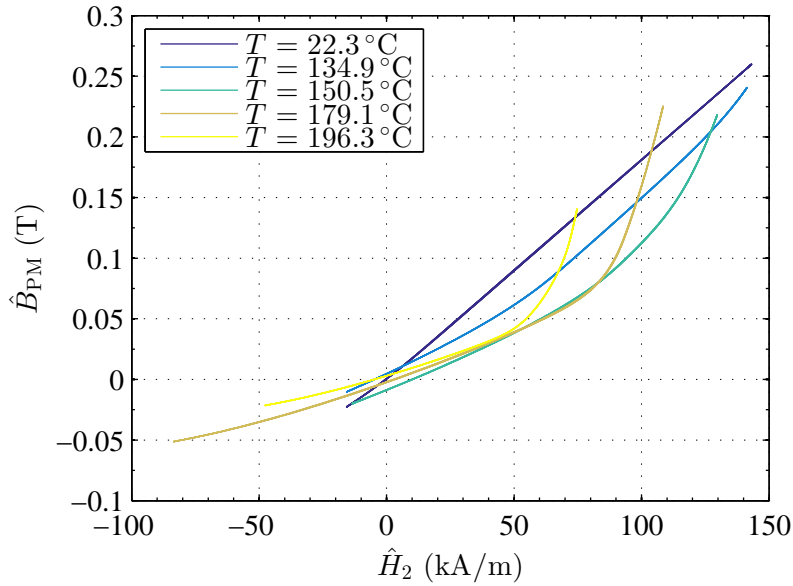


Figure 4.15: Measured characteristics of the PM at higher temperatures.

maximum operating temperature of the PM specified by the manufacturer is 130°C and its Curie temperature is 310°C . A high temperature leads to a similar effect as a material mismatch between core and PM material, as described in Section 4.1. Since this was a short-term test, the properties of the sample were only slightly affected irreversibly. Thus, the limitation must be caused by the ferrite.

4.3.1 Verification by Simulation

In order to verify the identification method, the procedure is applied to simulated data. The different fluxes are calculated at the cross-sections enclosed by the sensing coils and, as in reality, only their alternating component is used as input. An example result is shown in Fig. 4.16, for which a series of static simulations is used in order to exclude eddy currents. The identified μ and B_r are about 1% higher than specified in the simulation, i.e. the nominal values from the data sheet. The example confirms that only a small part of the characteristic curve is needed for the identification, on condition that the valid H range is reached.

4.3.2 Verification by Reference Measurements

In order to compare the results to another principle and for verification, measurements are taken with another principle. For this purpose, the magnetic and coordinate measuring machine (MCMM) [27] is used, which is designed for high-precision, contactless measurements of magnetic fields as well as the geometry in 3D, as described in Chapter 1. In [27], a method is described to determine the remanence of a permanent magnet

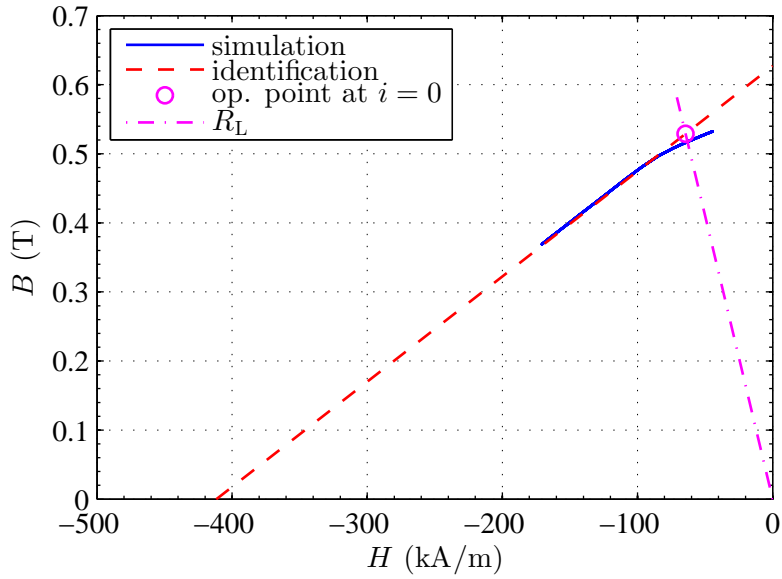


Figure 4.16: Identification procedure applied to simulated data from a series of static 3D FE simulations.

by means of free-field measurements, in contrast to the closed-circuit principle presented in this thesis. It is based on solving an inverse problem combined with FE simulations. For the simulations, the permeability of the PM has to be assumed, which also has a considerable influence on the stray field of a PM in air, similarly to the remanence. For this reason, the results are compared in an experiment which influences the magnetic properties of the sample irreversibly. For the evaluation with the MCMM, the system matrices are once set up with a constant permeability, and once with the permeability measured by the developed identification procedure (see Section 4.2).

Five samples were heated to 200 °C for the durations of 2 h, 12 h, 24 h and 48 h subsequently, which results in an accumulated time of 2 h, 14 h, 38 h and 86 h. They were characterized in between those periods at room temperature in order to exclude reversible effects. The MCMM was used to measure the remanence of one of the samples at only 3 points in time at 0 h, 38 h and 86 h, since it is a relatively time-consuming procedure. In contrast, one measurement with the presented method is a matter of seconds, since only a few periods of the excitation frequency are needed. The identified remanences are shown in Fig. 4.17 and the corresponding permeabilities in Fig. 4.18. As indicated in the legends of the plots, the samples are numbered in order to trace their history, which becomes relevant in Chapter 5. Concerning the results, the high temperature leads to irreversible changes of the remanence as well as the permeability. The remanence decreases, whereas the permeability tends to increase. The deviation of the remanence of the sample cross-checked by the MCMM is shown in Fig. 4.19. It varies if compared to the results with the assumed constant permeability, whereas it tends to stay constant if compared to the MCMM evaluation with the measured permeability. Although there is

4 Characterization of Magnetic Properties

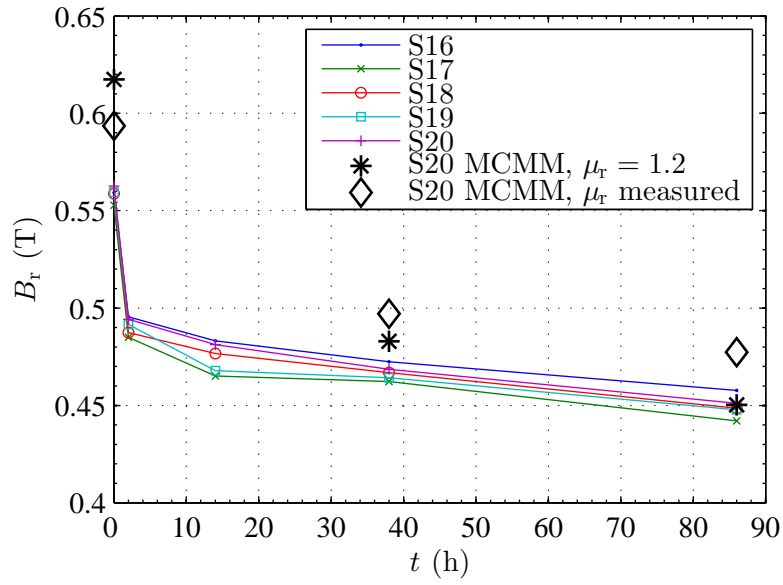


Figure 4.17: Remanence of five samples between heating periods to 200 °C characterized at room temperature.

a constant deviation of 5% to 6%, the influence of the permeability is conclusive. The remaining deviation might result from the different measurement principles, as a PM might behave differently in a closed magnetic circuit with a high permeability.

4 Characterization of Magnetic Properties

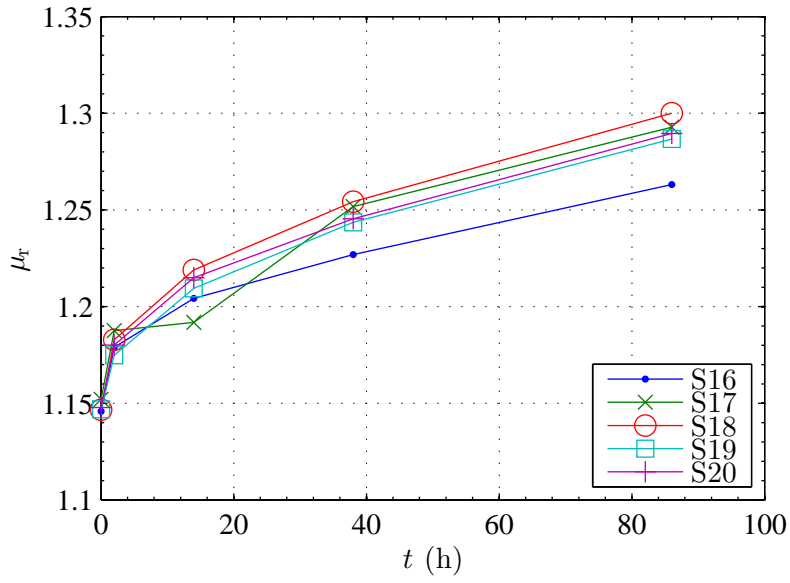


Figure 4.18: Permeability of five samples between heating periods to 200 °C characterized at room temperature.

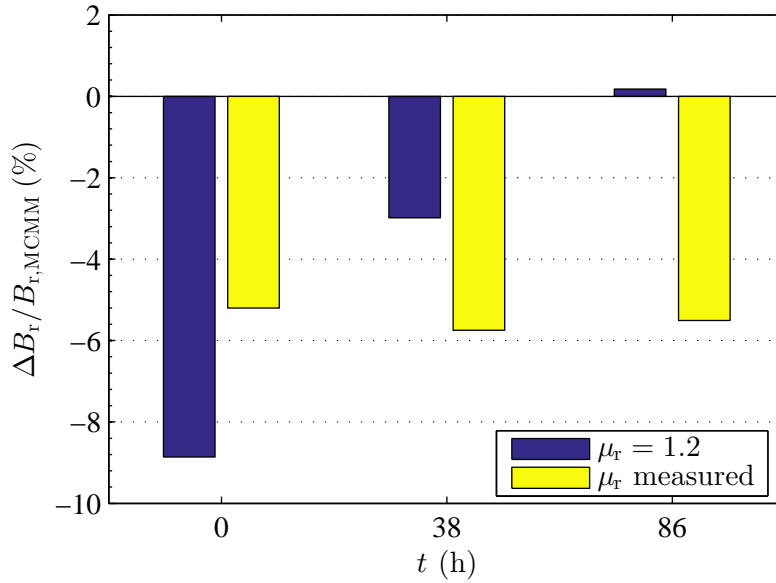


Figure 4.19: Deviation of the remanence of sample S20 from the MCMM. The permeability is once assumed as nominal and once measured, i.e. taken from the results shown in Fig. 4.18.

5 Application

In order to be able to make predictions and to physically understand the behavior of the magnets, different load conditions stressing the PMs have to be investigated. The idea of an application-oriented characterization is not new, see e.g. [8], where the authors studied reversible and irreversible effects of the temperature on sintered PMs. However, the PMs considered in this work are manufactured by pressing a powder mixed with synthetic material to lower the electric conductivity. Due to the plastic material, these PMs are not suited for temperatures as high as sintered PMs. Additionally, another influence is investigated, namely the magnetic load, which is a key feature of the application.

When performing different tests on numerous samples, it is important to keep track of the history of the samples. Hence, the samples are numbered and additionally identified by a letter. The samples used in Sections 5.2.1 and 5.2.2 are identified by the letters P and S and they are new samples of one batch respectively. They are further used throughout the chapter in Sections 5.2.4 and 5.3. Additionally, another type of samples is used in the long-term tests in Section 5.2.4. Those samples, denoted by U, basically have an unknown history. They were used for basic tests of chokes and were not stored separately, but in their chokes. An overview of the measurements, including the history of the samples, is provided in Section 5.2.4, where effects of the history can be observed.

As described in Chapter 3, the PMs are used in biased chokes, although most of the tests are performed on the magnets themselves, or in combination with the measurement setup described in Chapter 4. Apart from verification and extraction of the most important operating characteristics, the simulations are used for predicting the behavior of the application. The investigated application is an E-core choke, as e.g. described in [28], whose cross-section is basically the one of a doubled U-core choke described in Chapter 3 (see Fig. 3.1). This means that the inner leg of the E-core is double as wide as one outer leg. The computational mesh is shown in Fig. 5.1 without the surrounding air, and with symmetries with respect to the xy , the xz and the yz plane. The calculated flux lines are visualized at $t = 14.5 \mu\text{s}$, where the excitation is $i(t) = 4 \text{ A} \sin(2\pi 20 \text{ kHz } t) + 16 \text{ A}$. Compared to the U-core choke, it is also doubled in the third dimension, i.e. the choke consists of a total of four E-cores. This means that the cores doubled in z direction are 2 distinct parts, which is taken into account by adding a thin layer of air parallel to the xy plane.

5.1 Operating Range

Before performing stress tests, it is important to know the operating range of the PMs in the application as well as in the measurement setup. This can be accomplished very precisely by means of FE simulations. Most importantly, the flux density in the

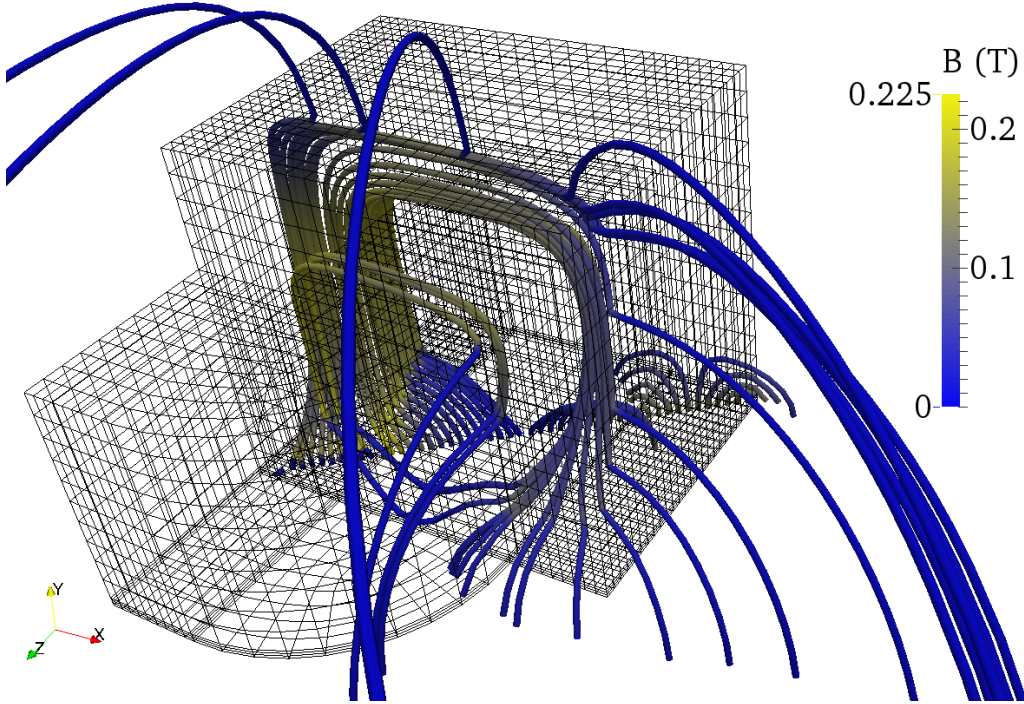


Figure 5.1: Mesh of the E-core choke and simulated flux lines colored by $\|\vec{B}\|$.

PM can be analyzed with respect to the excitation coil current, which determines the magnetic load and enables determining which current corresponds to which flux density in each setup in order to compare them. The flux density in the inner PMs of an E-core choke is shown in Fig. 5.2 for the defined worst-case excitations of the form $i(t) = \hat{I} \sin(2\pi 20 \text{ kHz} t) + I_0$. The excitation of the choke with the higher number of turns of $N = 56$ even leads to loading the PM up to the 3rd quadrant, i.e. a negative flux density. However, as the PM features a higher H_{cJ} than H_{cB} , this excitation is not critical with respect to the polarization (see Fig. 2.3 and Tab. 2.1).

The differential inductance of the setups is another important design quantity, especially regarding the frequency of the excitation current and the electric power source. An overview of the different chokes compared to the measurement setup is given in Fig. 5.3. For reasons of comparability, all results are calculated with the same number of turns. The U-core is only interesting for testing due to its lower inductance and therefore the lower electric power needed at higher frequencies. However, its B versus i characteristics differ from the E-core choke, where the inner and outer PMs are loaded differently, which has to be taken into account when comparing those two types. Its inductance is about a quarter, since it corresponds to a quartered E-core choke, as described in the introduction of the chapter. For the tests and measurements, several different numbers of turns were used. However, the mostly used numbers are $N = 41$ and $N = 56$ for the chokes, and $N = 56$ and $N = 112$ for the measurement setup. The inductance of the measurement setup with $N = 112$ can be seen in Fig. 4.9.

5 Application

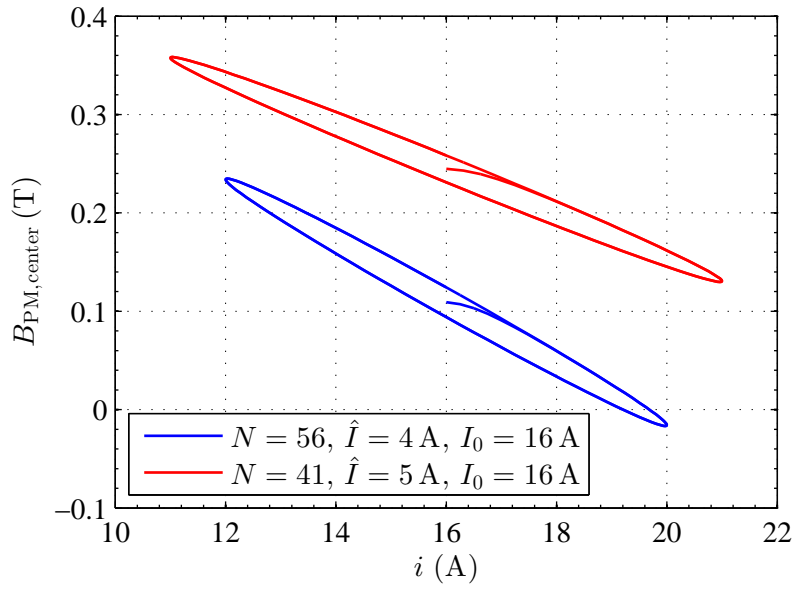


Figure 5.2: Simulated flux density in the inner PMs of the chokes for the worst-case excitations.

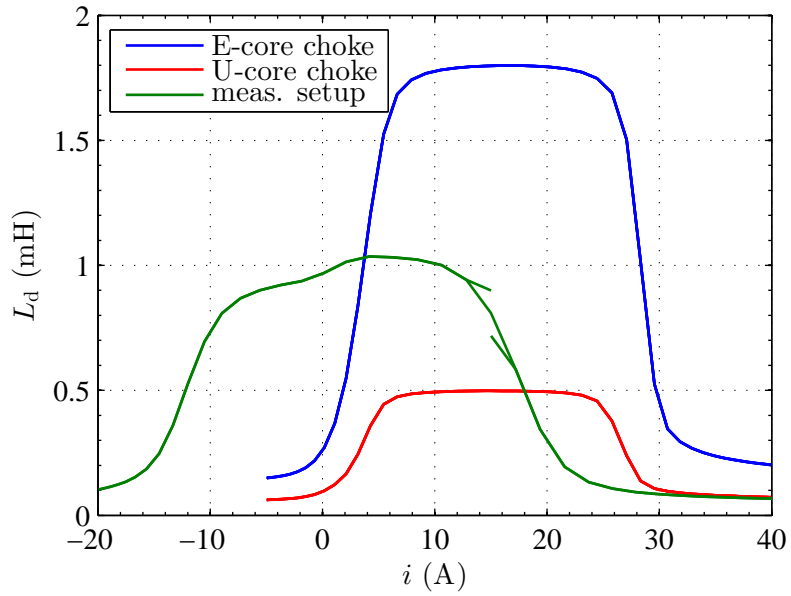


Figure 5.3: Overview of the simulated differential inductances of the chokes and the measurement setup with $N = 56$.

5 Application

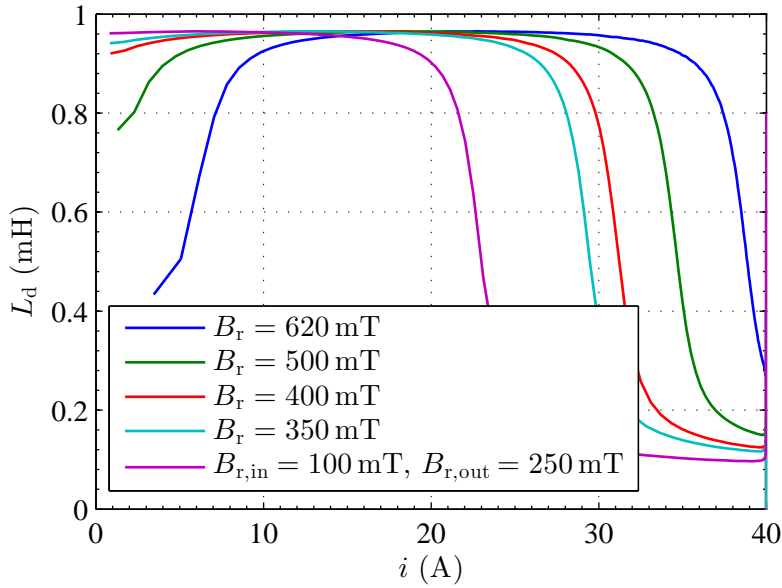


Figure 5.4: Simulated differential inductances of the choke with different remanences.

Since the remanence of the PM affects the offset of the current in the inductance characteristics, the choke is simulated with different remanences, as shown in Fig. 5.4. In order to verify these simulations, the excitation is chosen similar as in the corresponding measurement setup. The chokes were tested with so-called power choke testers. The principle is to load a high capacitance, which is connected to the inductor under test via a switch. The advantages of such a measurement principle are that very high currents can be reached and the effort and cost are less compared to a sinusoidal excitation with a sophisticated power amplifier. The disadvantages are that the capacitance forms a resonant circuit with the inductor and the excitation is step-like, which shows a wide amplitude spectrum. However, the capacitance is not considered in the simulations, but the excitation is specified as a voltage step function. The ohmic resistance of the coil is specified as $40 \text{ m}\Omega$, which is about the mean value of the chokes investigated. Even though the capacitance is not considered, the current shows an interesting behavior against time, as depicted in Fig. 5.5. The sharp change of the inductance causes a sudden increase of the slope of the current. As shown with the different remanences of inner and outer PMs, the asymmetric distribution of the remanences does not have the same effect. Finally, the simulated inductance is also compared to a measurement of a choke with new PMs in Fig. 5.6. Considering the geometric and magnetic tolerances of the whole choke, it is a good result. The changes of the inductance are about at the same current values.

5 Application

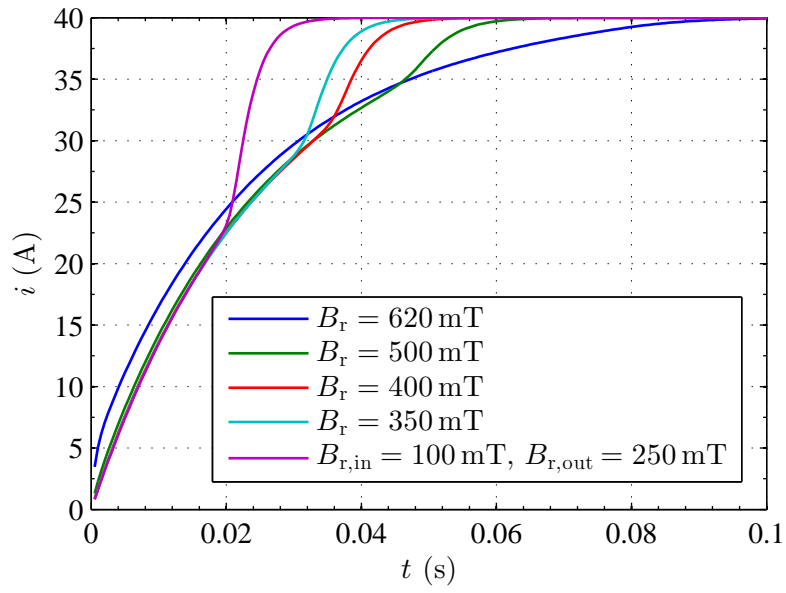


Figure 5.5: Simulated coil current during a choke test with different remanences.

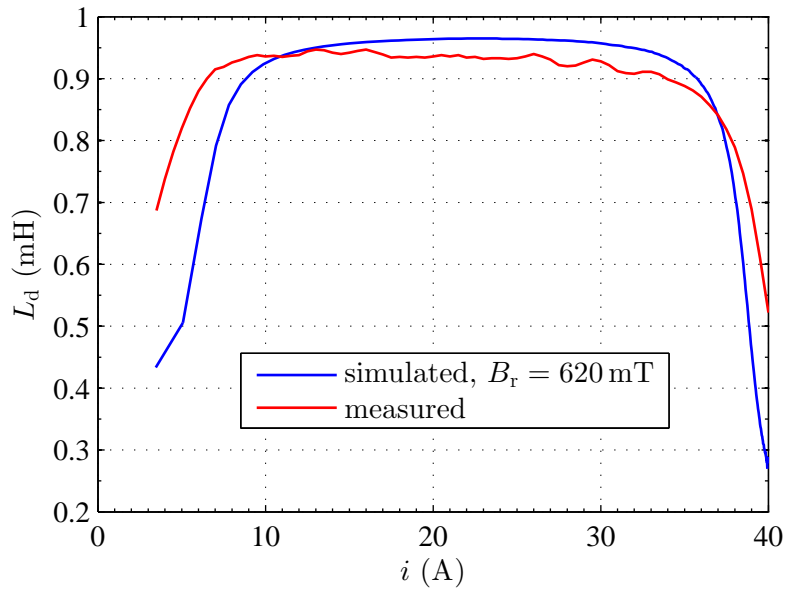


Figure 5.6: Simulated and measured differential inductance of one choke with $N = 41$.

5.2 Stress Tests

In order to investigate the influence of certain load conditions and to separate the influence of individual loads, several different tests are performed. The main loads are firstly the temperature and secondly the magnetic load. Additionally, the tests have to be distinguished by their duration, i.e. short-term or long-term. A rise of the temperature can result from Joule heating due to eddy currents as well as the excitation current in the turns of the coil, and it also depends on the ambient temperature. In order to simulate either different ambient temperatures or to simulate a predefined temperature, e.g. the maximum operating temperature of the PM, a setup as depicted in Fig. 5.7 is used. In this picture, the measurement setup is placed inside a thermally isolated box with an inlet and an outlet for a controlled air stream. The whole setup is shown in Fig. 5.8, which also includes the data acquisition system and the environmental simulator. This simulator is able to generate an air stream of controlled temperature and flow and it also allows for connecting a thermocouple for controlling the temperature at a specific location. The controllable temperature of this device ranges from -90°C to 225°C .

5.2.1 Temperature Cycle up to Maximum Operating Temperature

In these short-term tests, single samples are placed in the measurement setup in the thermal box. The temperature is measured near the PM and at several temperatures, the remanence is measured. A typical cycle is shown in Fig. 5.9, where the change of remanence is displayed against temperature. Those cycles are basically performed as fast as possible, but still the shown measurement took about 7 h for both cycles due to the settling time and the thermal time constants of the setup. The temperature is varied from -20°C to 130°C , which is the maximum operating temperature specified by the manufacturer. As shown, this sample underwent 2 consecutive cycles and it did not lose any more remanence after the first cycle. Consequently, these tests aim at the reversible and the (irreversible) initial remanence losses of new samples. Such initial losses are also mentioned in e.g. [8].

The remanence of all samples is shown in Fig. 5.10 against the temperature. The purpose of this plot is to provide an overview of the range of the measured values. A more detailed analysis is given in Fig. 5.11, which shows the difference of the remanence of all samples after one cycle at room temperature. The change of the remanence is calculated by $\Delta B_r = B_{r,\text{start}} - B_{r,\text{end}}$, which results in positive values for a loss. The measurements yield an initial loss in the range of a few percent.

5.2.2 Magnetic Load at Maximum Operating Temperature

The PMs are magnetically loaded at the maximum operating temperature, since this is expected to have the maximum effect. The samples are placed in the measurement setup, which is used for the excitation and for the measurements alternately. This means that the excitation is active during nearly the whole time of the measurement, only interrupted by the measurement procedure for a few seconds at some instants during

5 Application

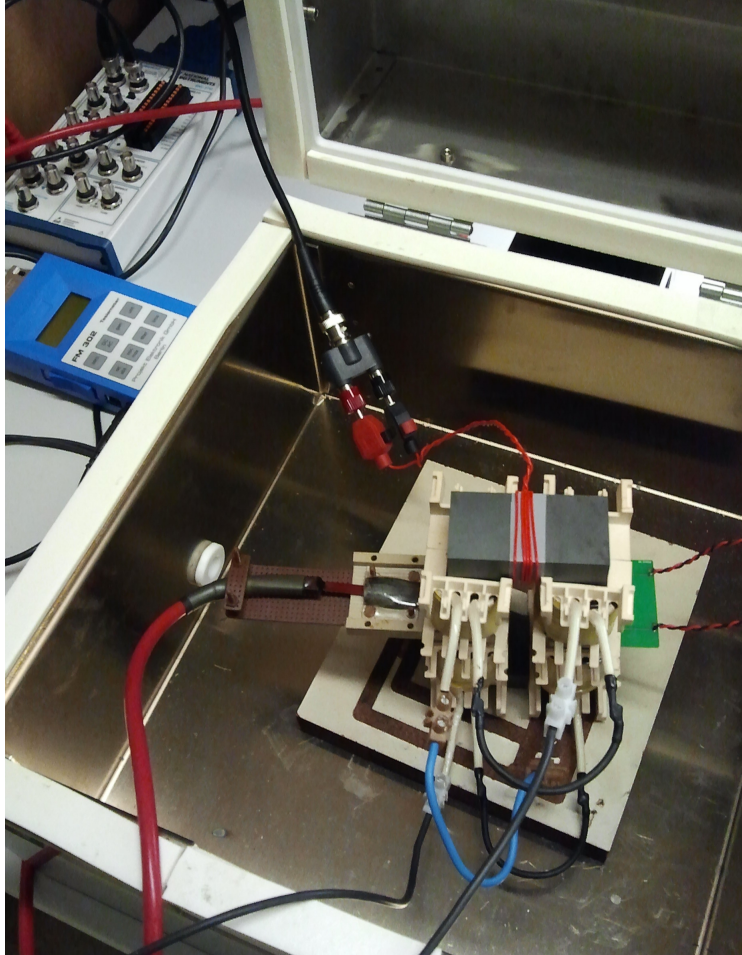


Figure 5.7: Photograph of the measurement setup in a thermal box.

5 Application



Figure 5.8: Photograph of the measurement system including the environment simulator.

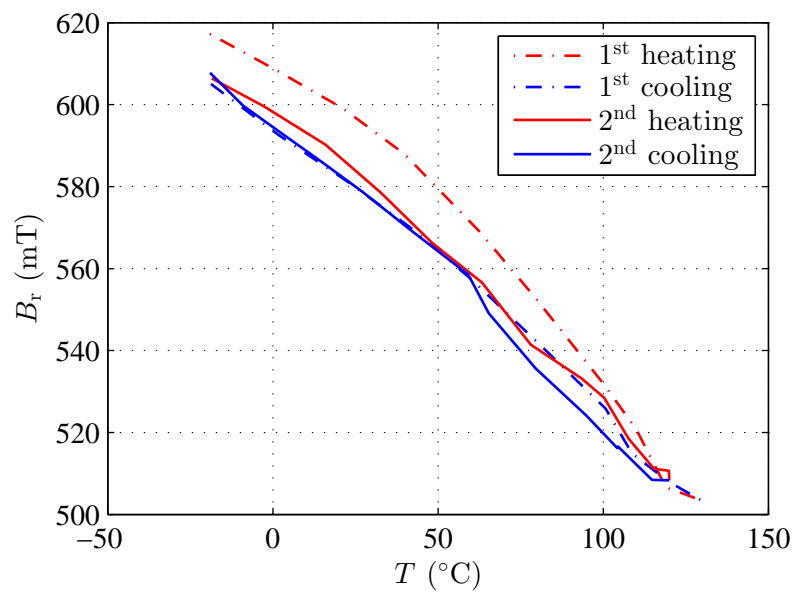


Figure 5.9: Remanence against temperature of sample P1 during 2 consecutive cycles.

5 Application

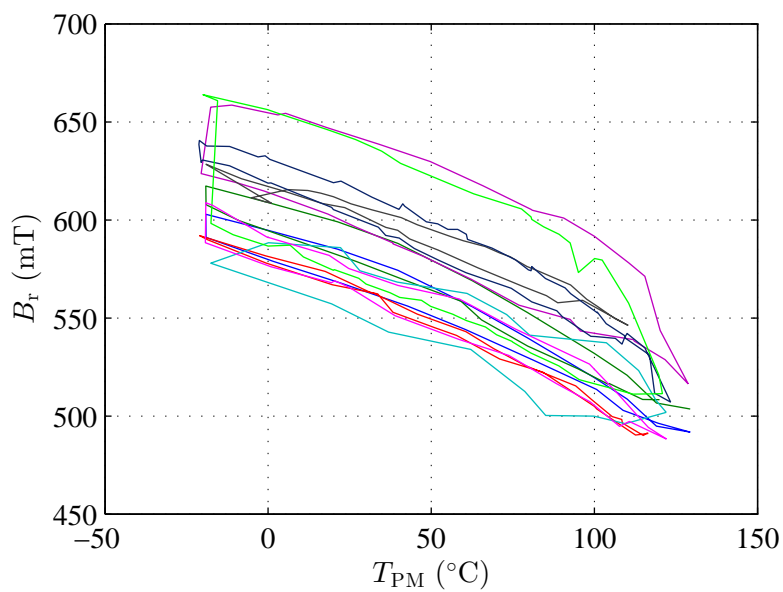


Figure 5.10: Overview of the measured remanence of samples P1 to P8 during temperature tests.

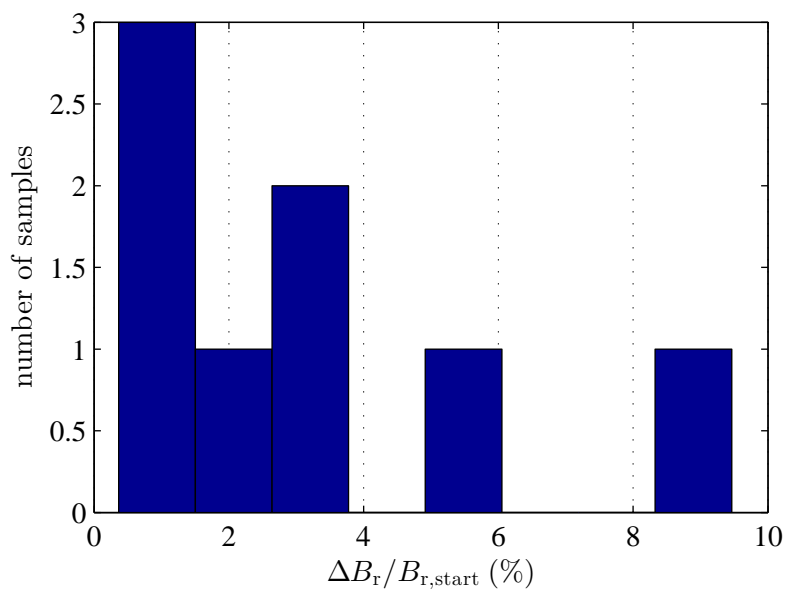


Figure 5.11: Relative difference between the remanence at the start and the end of the cycle of samples P1 to P8.

5 Application

sample	f (Hz)	I_0 (A)	\hat{I} (A)	N
S1	1000	0	13	56
S2, S3	500	4	9	56
S4, S5	500	1	15	56
S7, S8	500	0	16	56
rest	50	0	15	112

Table 5.1: Overview of the excitation current for the different samples.

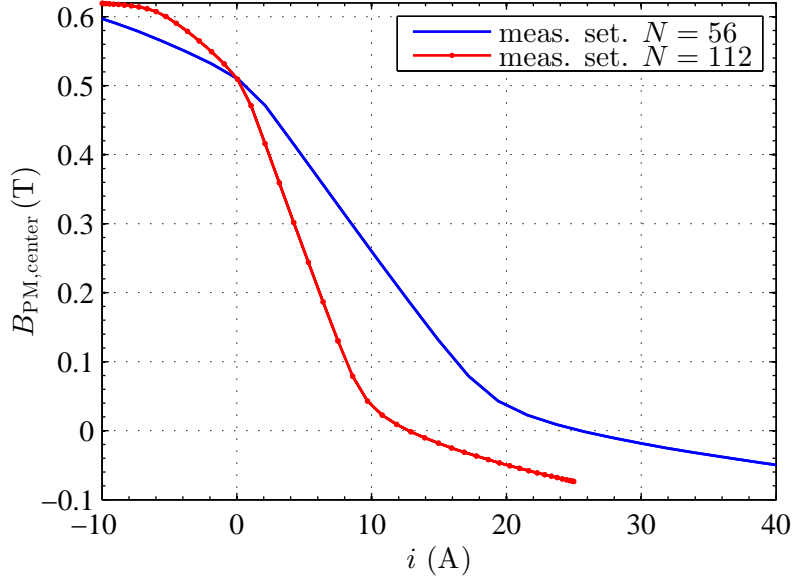


Figure 5.12: Simulated flux density in the center of the PM in the measurement setup.

the measurement. The environment simulator is used to raise the temperature to a value of 130°C instead of solely the excitation, since it takes less time and the temperature can be kept at a defined value more easily. During the first tests, different configurations were used for the excitation in order to find an excitation, which can be provided by the power source for a longer period of time. Due to the design of four-quadrant linear power amplifiers, they have to dissipate a high amount of heat when operated at low power factors in one quadrant, which limits their long-term capabilities. The excitation currents of the form $i(t) = \hat{I} \sin(2\pi f t) + I_0$ are listed in Tab. 5.1. For a better overview, Fig. 5.12 shows the corresponding flux density in the PM for a remanence of 620 mT. After the first tests, the decision was made to increase the number of turns in order to reach the 3rd quadrant of the PM characteristics, thus lowering the frequency, whereas the measurement setup is mainly heated by the environment simulator.

The typical procedure of the tests is shown in Fig. 5.13, where the temperature and the remanence are plotted against time. As mentioned, the PMs are magnetically loaded

5 Application

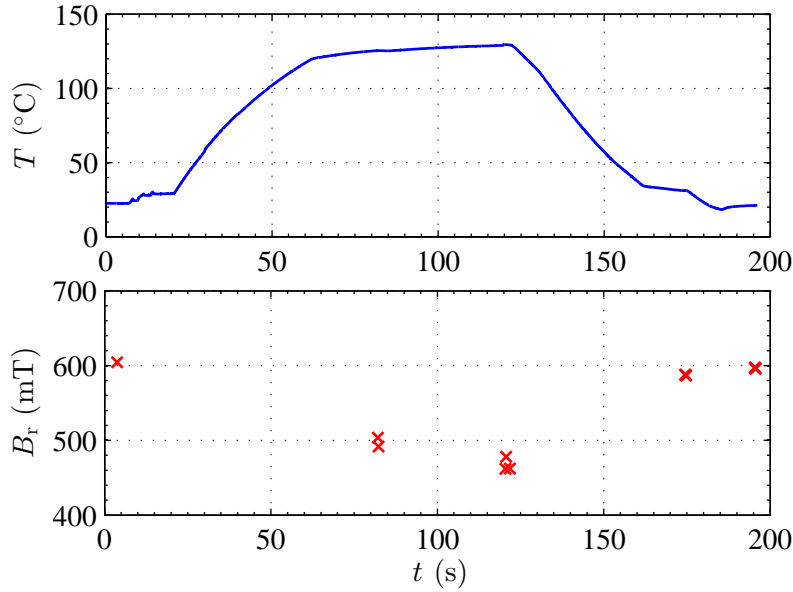


Figure 5.13: Remanence and controlled temperature during the test of sample S1 with excitation.

during the whole test. The remanence is measured at the beginning, at the end and at several time instants in between. The measurement setup is kept at 130 °C for 1 h. As for the tests without excitation, the difference between the remanence at the start and at the end of the test is shown in Fig. 5.14. Interestingly, the PMs show a difference in the same range as after the cycles without excitation (see Fig. 5.11). Although it seems that there are two peaks in the histogram of Fig. 5.14, no correlation is found between the different excitations and the peaks. The number of 16 samples is comprised of samples S1 to S13 and 3 samples composed of 8 parts as described in Section 5.4.

5.2.3 Special Tests

Special tests are performed to exclude or confirm certain effects. First, one sample is magnetically loaded at maximum operating temperature for a longer period of time. The temperature and remanence of the sample are shown in Fig. 5.15. The excitation is active over the whole time of 7.6 h, where the temperature is at 130 °C for about 5.5 h. In this test, the PM shows an initial loss of 4.7%, which is the loss of the remanence from the beginning to the end of the procedure at room temperature, and which is in the same range as previously measured losses as described in Sections 5.2.1 and 5.2.2.

Another test aims at ensuring that the measured remanence is not influenced by the value of the current at which the excitation stops at higher temperatures. Therefore, the remanence is measured multiple times with different end conditions for the excitation current. The sinusoidal current is stopped at different slopes, i.e. phases. In previous measurements, the excitation was turned off at a random phase, whereas the excitation

5 Application

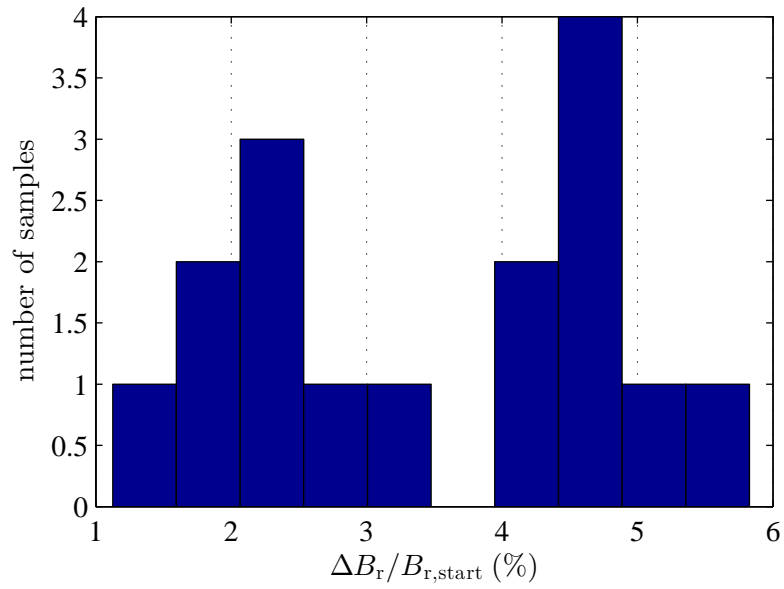


Figure 5.14: Relative difference between the remanence at the start and the end of the magnetic load at 130°C of 16 samples.

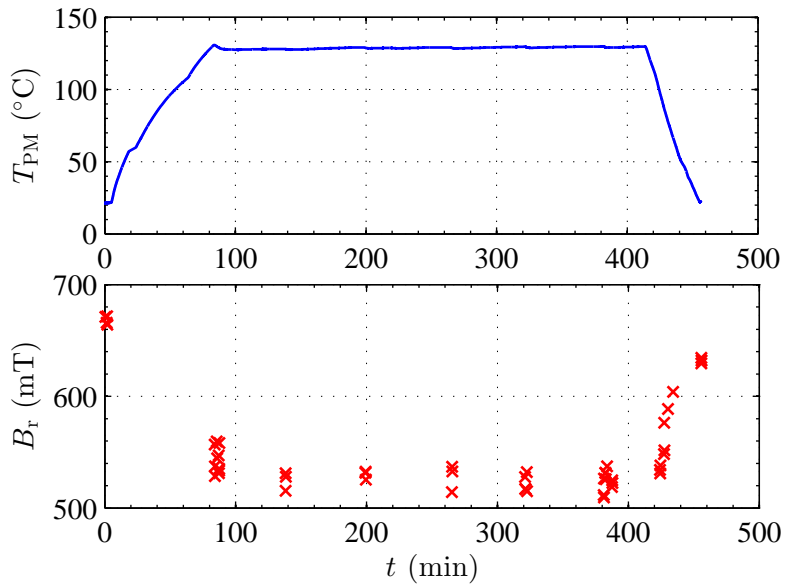


Figure 5.15: Controlled temperature and remanence during a longer test of sample S13 with excitation.

5 Application

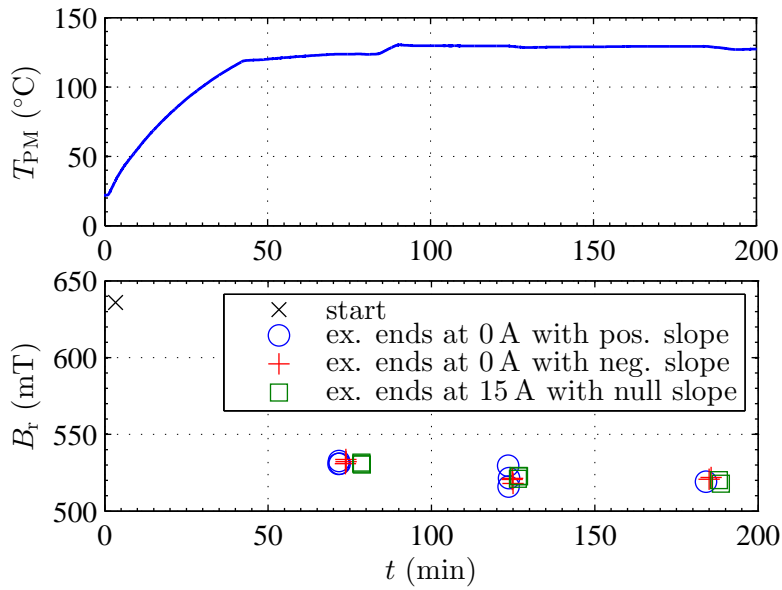


Figure 5.16: Temperature and remanence during a test of sample S14 with different end conditions for the excitation.

is shut down in a controlled way in this test. The results of these measurements are shown in Fig. 5.16. As shown, the end condition does not seem to have an influence.

5.2.4 Long-Term Tests at Elevated Temperatures

Since the previous tests are rather short-term, the PM are heated to specific temperatures for longer periods of time. In order to test more samples at the same time, they are attached to a steel block and exposed to elevated temperatures without the measurement setup, since the setup can only hold one sample. After one heating period, they are characterized at room temperature and put into the environment simulator again to continue the heating. These are the same tests as used for the verification of the measurements in Section 4.3.2 and shown in Figures 4.17 and 4.18, where the PMs were heated to 200 °C.

The resulting remanence and permeability of a test at 130 °C, which is the maximum operating temperature of the samples, are shown in Figures 5.17 and 5.18. These samples have an unknown history, except that they were used in basic tests of chokes and were stored for about one year. Still, they show a small initial loss, which indicates that they have not suffered from a very high temperature. Additionally, the permeability also follows the rising trend, though not as fast as the samples at 200 °C shown in Fig. 4.18. Considering the range between 38 h and 86 h, it is roughly 10 times slower.

This also pertains to the next set of samples heated to 130 °C, whose results are shown in Figures 5.19 and 5.20. However, the difference is that these samples were already loaded magnetically at 130 °C as described in Section 5.2.2, and stored for about one

5 Application

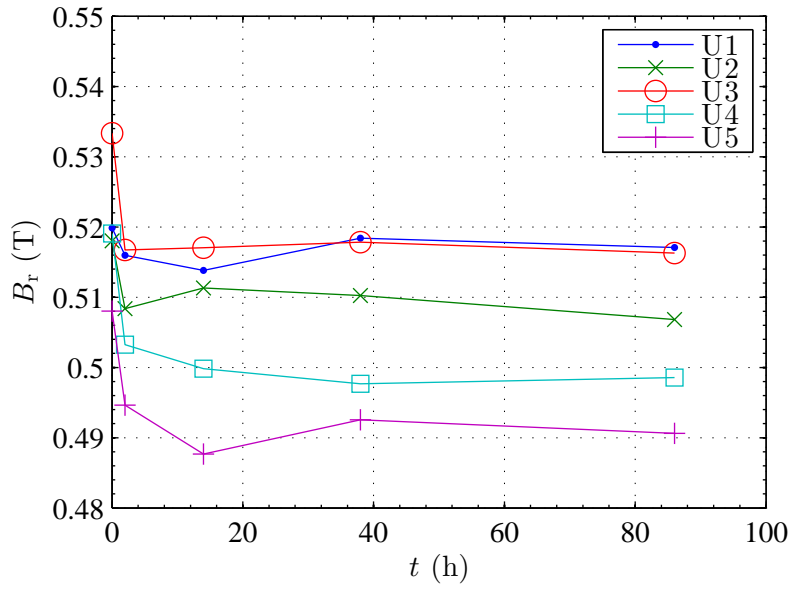


Figure 5.17: Remanence of samples U1 to U5 between heating periods to 130 °C characterized at room temperature.

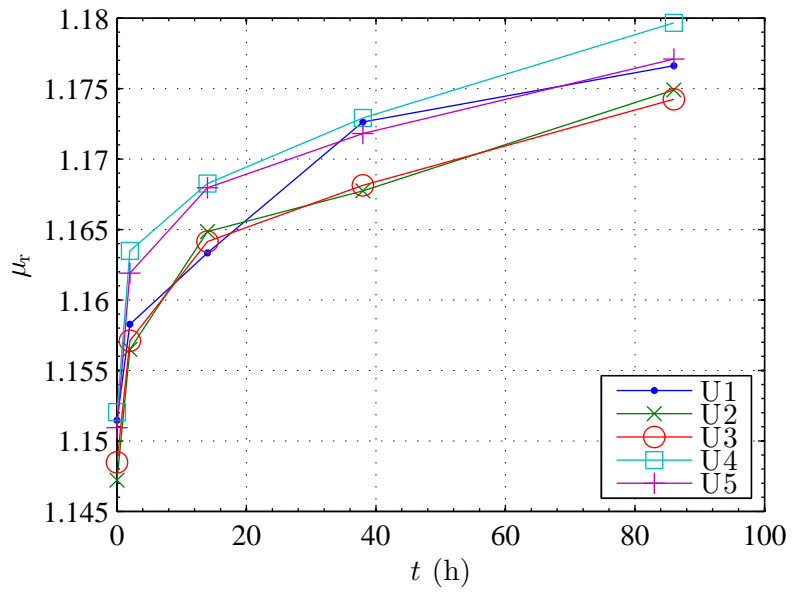


Figure 5.18: Permeability of samples U1 to U5 between heating periods to 130 °C characterized at room temperature.

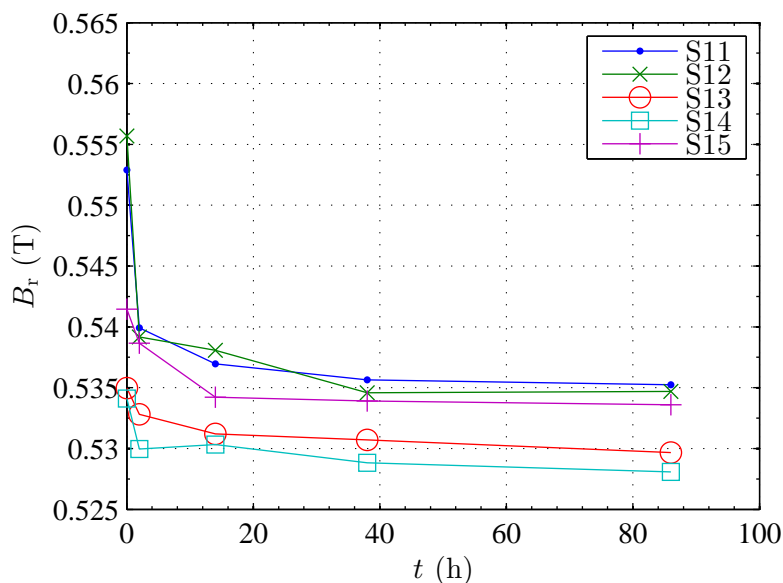


Figure 5.19: Remanence of samples S11 to S15 between heating periods to 130 °C characterized at room temperature.

year before the long-term tests. This also applies to the series at 150 °C (see Figures 5.21 and 5.22) and the series at 180 °C (see Figures 5.23 and 5.24). Since the history of the individual samples has an effect on the results, a general, condensed presentation of the results makes less sense than for the previous short-term tests (see Sections 5.2.1 and 5.2.2), where the results are summarized in a histogram. Therefore, the results are evaluated in form of a table in Tab. 5.2. It contains the difference of both the remanence and the permeability between the start and the end of the test, i.e. before and after the accumulated 86 h of thermal load. Both differences are calculated by subtracting the starting value from the end value. The difference in remanence is specified relatively to the corresponding starting value, which is not done for μ_r , since it is already related to μ_0 . For both quantities, the slope at the end of the test is shown, i.e. the difference quotient between $t = 38$ h and $t = 86$ h. This quantity is mainly used to give an impression of the scale of the effect and to provide an additional quantity for comparison at different temperatures. The slope of μ_r is scaled as $\%_0/\text{h}$, which means that a value of 1 corresponds to a change by one μ_0 in 1000 operating hours. As mentioned, its main purpose is for comparison, since it seems to be still subject to change after only 86 h. Finally, in the last column, the history of the samples is noted.

In general, the results show roughly the same trends, which is a decrease of the remanence and an increase of the permeability. The new samples lost about 20 % of their remanence over the 86 h at 200 °C. The samples show a similar behavior and their remanence and permeability values are grouped if they share the same history, which can be well observed with the samples S6 to S10 at 180 °C (see Figures 5.23 and 5.24) as well as the samples S16 to S20 at 200 °C (see Figures 4.17 and 4.18). On the other hand,

5 Application

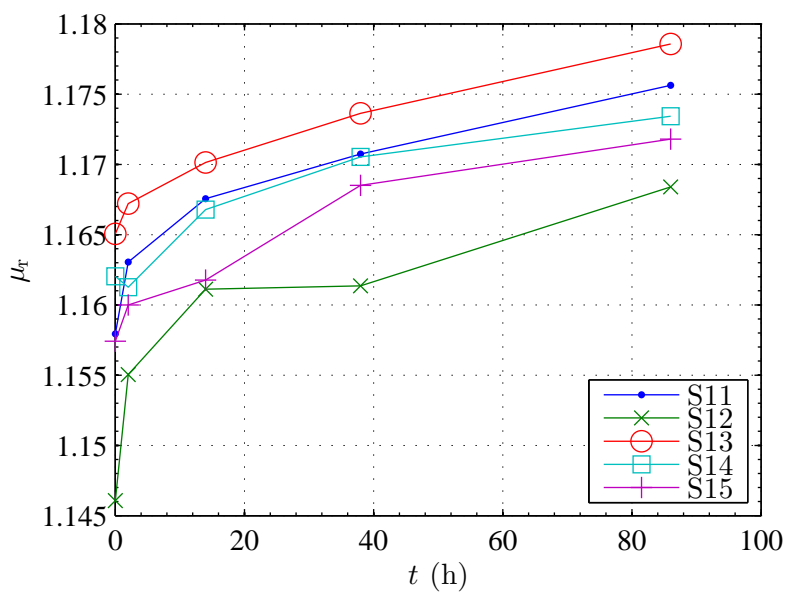


Figure 5.20: Permeability of samples S11 to S15 between heating periods to 130°C characterized at room temperature.

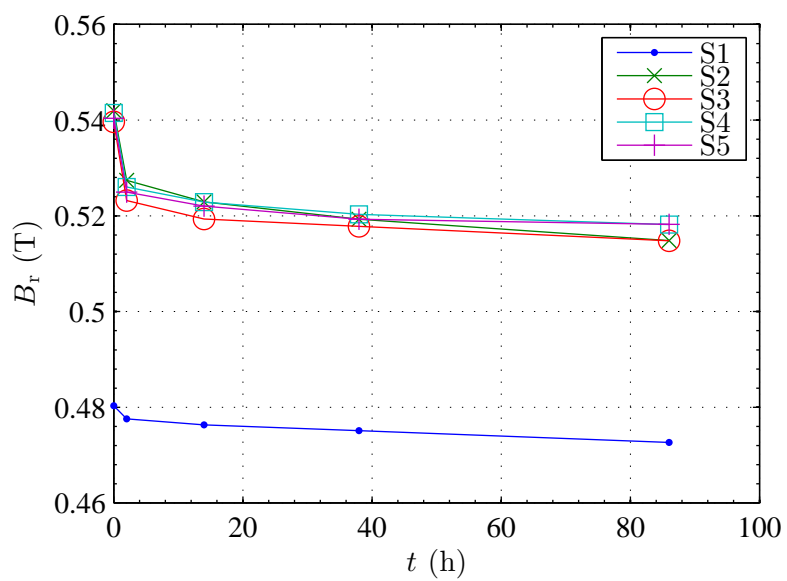


Figure 5.21: Remanence of samples S1 to S5 between heating periods to 150°C characterized at room temperature.

5 Application

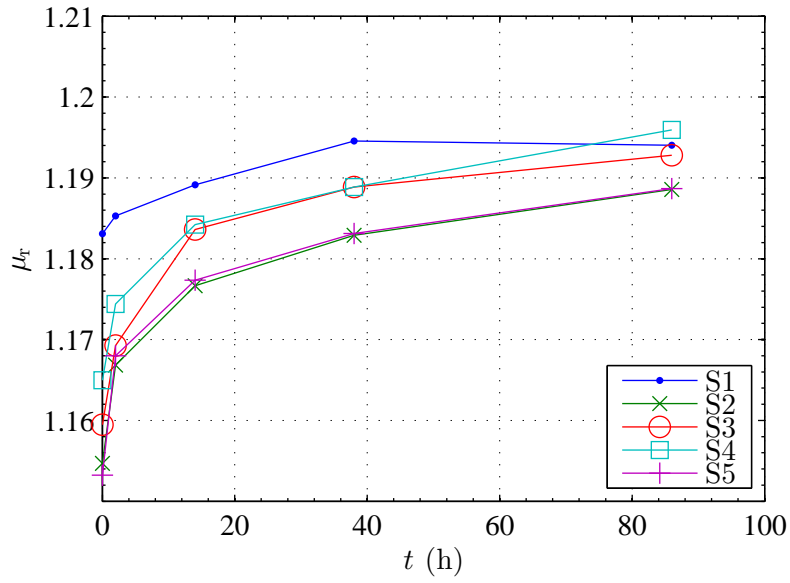


Figure 5.22: Permeability of samples S1 to S5 between heating periods to 150°C characterized at room temperature.

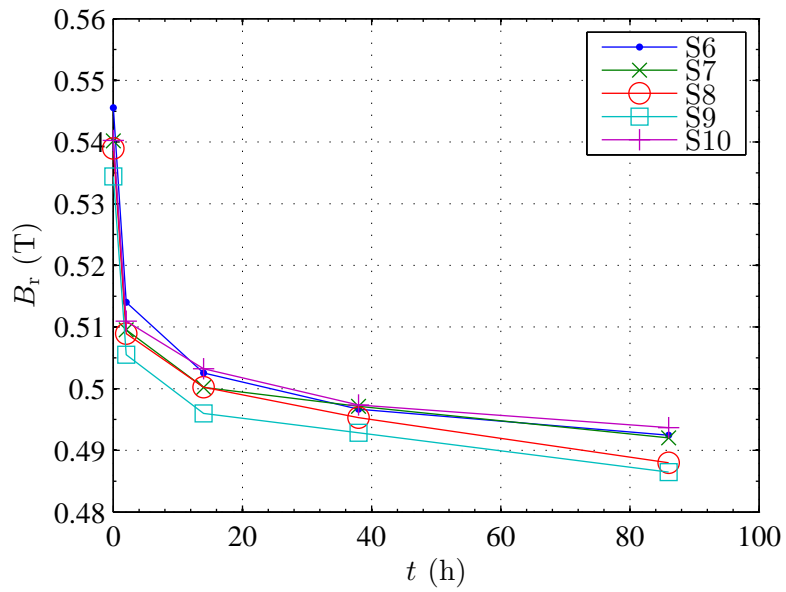


Figure 5.23: Remanence of samples S6 to S10 between heating periods to 180°C characterized at room temperature.

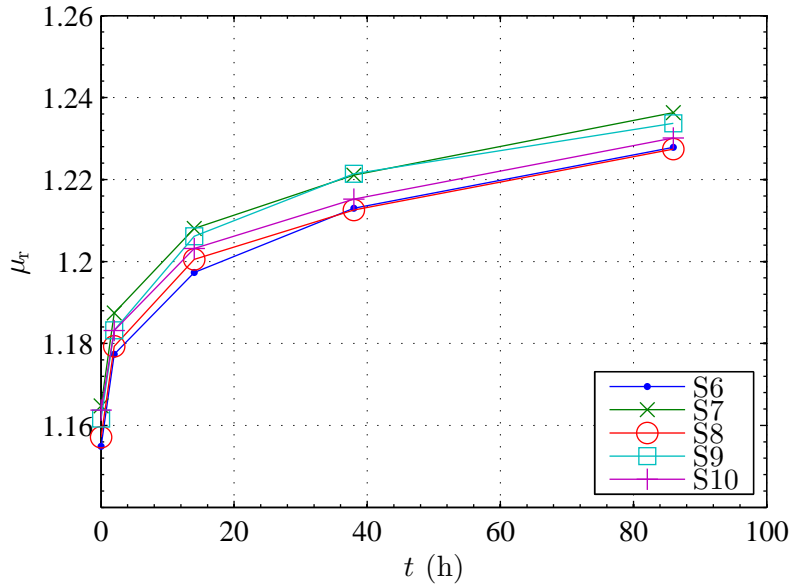


Figure 5.24: Permeability of samples S6 to S10 between heating periods to 180 °C characterized at room temperature.

correlations can be found for samples with a different history. The samples S13 and S14 at 130 °C show a lower loss of remanence and a lower increase of the permeability, since they were used for special tests. S15 also shows lower changes, since its magnetic load test (denoted by (a)) was carried out for about 3 h in total, whereas the typical duration of the test was about 2 h including heating and cooling. Samples S13 to S15 also have a lower remanence from the start (see Fig. 5.19). In this regard, sample S1 might be most noticeable (see Fig. 5.21). Due to several previous experiments, it has a comparably low remanence from the start and loses only 1.6 %. Its permeability seems to fall again in the end, although the value might be too low to draw conclusions. However, the measurement after 86 h at 150 °C is not an outlier, since S1 was characterized again after the tests with S6 to S10, yielding the same results.

5.3 Electric Conductivity

The electric conductivity of the samples is measured before the stress tests by means of four-terminal sensing, since this is a very simple and reliable technique. A photograph of the measurement setup is shown in Fig. 5.25. The sample is connected to an electric current source with two notched aluminium blocks and the voltage is measured with two electrodes on the surface of the sample. The measurements are performed at different currents of $I = \{0.25, 0.5, 0.75, 1\}$ A and different distances of $l = \{5.08, 10.16, 15.24\}$ mm

5 Application

T (°C)	sample	$\frac{\Delta B_r}{B_{r,start}}$ (%)	$\left(\frac{\Delta B_r/\Delta t}{B_{r,start}}\right)_{end}$ (ppm/h)	$\Delta\mu_r$	$\left(\frac{\Delta\mu_r}{\Delta t}\right)_{end}$ (%/h)	history
130	U1	-0.5	-53	0.025	0.083	unknown
	U2	-2.2	-137	0.028	0.149	
	U3	-3.2	-61	0.026	0.127	
	U4	-3.9	35	0.028	0.140	
	U5	-3.4	-80	0.026	0.110	
130	S11	-3.2	-15	0.018	0.102	(a)
	S12	-3.8	4	0.022	0.147	(a)
	S13	-1.0	-41	0.014	0.103	(b)
	S14	-1.1	-29	0.011	0.061	(a), (c)
	S15	-1.5	-12	0.014	0.069	(a)
150	S1	-1.6	-107	0.011	-0.011	(a), (d)
	S2	-5.0	-171	0.034	0.118	(a)
	S3	-4.6	-117	0.033	0.082	(a)
	S4	-4.3	-82	0.031	0.147	(a)
	S5	-4.1	-41	0.035	0.115	(a)
180	S6	-9.7	-160	0.073	0.309	(a)
	S7	-8.9	-197	0.072	0.318	
	S8	-9.5	-283	0.070	0.309	
	S9	-9.0	-248	0.072	0.256	
	S10	-8.6	-142	0.066	0.311	
200	S16	-18.2	-551	0.117	0.753	new
	S17	-20.0	-761	0.141	0.855	
	S18	-19.7	-683	0.153	0.953	
	S19	-20.0	-612	0.140	0.899	
	S20	-19.8	-647	0.142	0.919	

Table 5.2: Results of the long-term tests after 86 h at temperature T . (a) denotes the excitation tests at 130 °C from Section 5.2.2. (b) and (c) denote the longer excitation test and the slope test, respectively, from Section 5.2.3. (d) denotes the high temperature test of the measurement setup from Section 4.3.2.

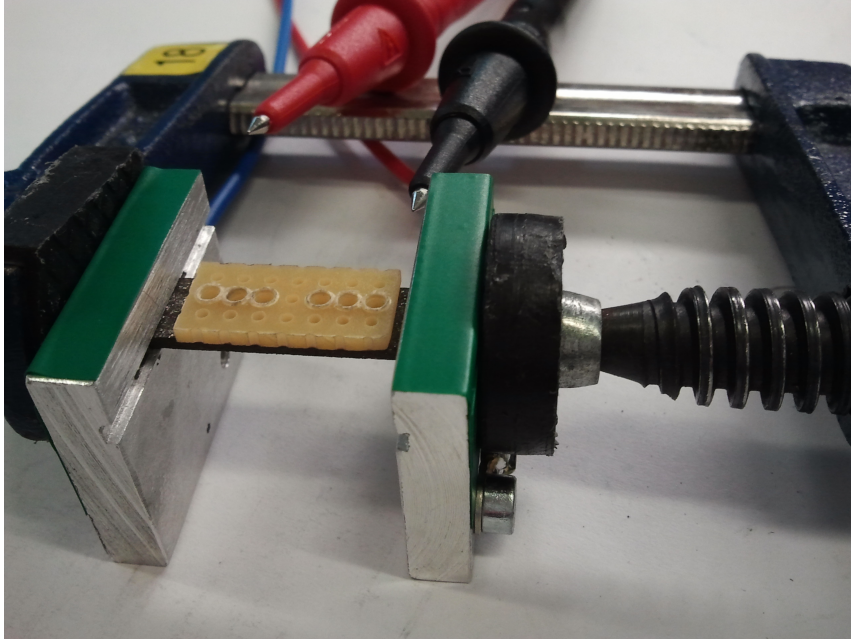


Figure 5.25: Setup for measuring the electric conductivity.

between the voltage sensing electrodes. The electric conductivity is calculated from

$$\gamma = \frac{lI}{\Gamma V}, \quad (5.1)$$

where Γ denotes the cross-section of the sample perpendicular to the surface and normal to the current density, and V the measured electric voltage. The resulting conductivity per sample is the mean value of the measurements at the different currents and distances. The surface, on which the conductivity is measured, is parallel to the plane where the eddy currents are expected to occur, since the magnetic flux density mainly points in direction of magnetization in the application, i.e. the direction of the short edges.

The measurement of the conductivity of samples P1 to P8 is shown in Fig. 5.26. These are the same samples that are used for the temperature cycles described in Section 5.2.1 before the stress tests. The conductivity shows an outlier with nearly double the value in Fig. 5.26. However, the mean value lies in the range of the conductivity of a comparable product specified by another manufacturer, namely *Neofer 55/100p* manufactured by *Magnetfabrik Bonn GmbH*, where the specific resistance is specified as $\sigma = 50 \mu\Omega\text{m}$, which corresponds to $\gamma = 20 \text{ kS/m}$. The electric conductivity of the investigated samples is not specified in the data sheet.

Due to visible inhomogenities in the material, the electric conductivity of samples S1 to S20 is investigated in more detail. These are the samples designated for the stress tests with excitation, as described in Section 5.2.2. Instead of measuring on just one surface, the conductivity is determined on the top and on the bottom surface. The results of these 40 measurements are depicted in Fig. 5.27. Additionally, the difference

5 Application

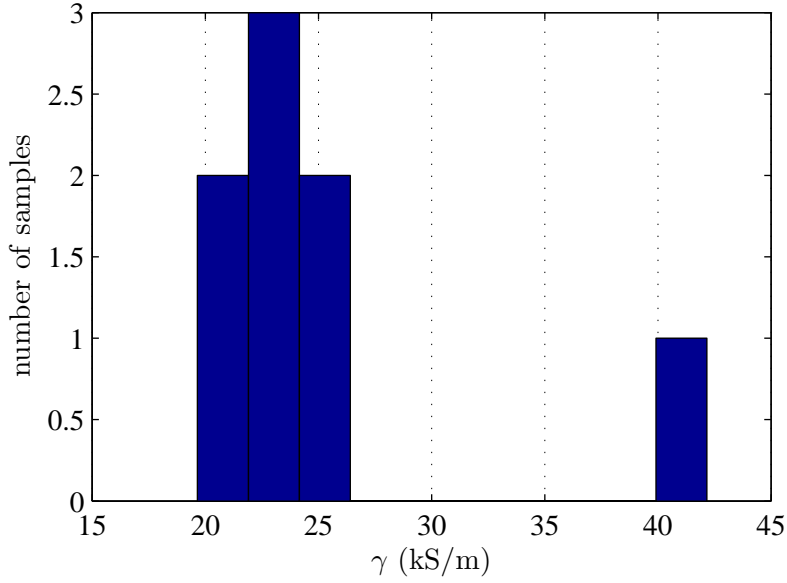


Figure 5.26: Measured electric conductivity of samples P1 to P8.

between the top and bottom surface is of interest, which is defined as

$$\Delta\gamma = \frac{|\gamma_{\text{up}} - \gamma_{\text{down}}|}{\max\{\gamma_{\text{up}}, \gamma_{\text{down}}\}}, \quad (5.2)$$

and which is shown in Fig. 5.28. The samples show a deviation of up to 15%, which is a considerable value regarding the eddy currents. As a side note, the mean value of the 40 measurements of $\gamma = 26.3262$ kS/m is used for the simulations starting from Section 3.2.

In order to provide a visual impression of the inhomogeneities, photographs of the top and bottom surface of one sample are shown in Figures 5.29 and 5.30. The distribution of lustrous metallic particles is more homogeneous in Fig. 5.30, whereas they form clusters on the top surface (see Fig. 5.29). The measured conductivity is actually not a local quantity, but obtained from averaging over a large part of the volume. However, the inhomogeneities might have additional local effects. If the conductivity is locally higher, the eddy currents could concentrate and lead to a hotspot, where the temperature rises more rapidly.

The temperature dependence of the electric resistivity, or conductivity, is another effect to consider. Since the conductivity usually decreases with rising temperature, it actually helps to prevent overheating of the PM. However, the influence of the conductivity on the eddy power is only linear. The temperature dependence of sintered SmCo and NdFeB magnets was investigated in [9]. Assuming a similar behavior of the plastic-bonded, isotropic neodymium samples used in this work, the effects are roughly estimated. Based on Fig. 7 in [9], the transversal resistivity of NdFeB samples rises from about $1.275 \mu\Omega\text{m}$

5 Application

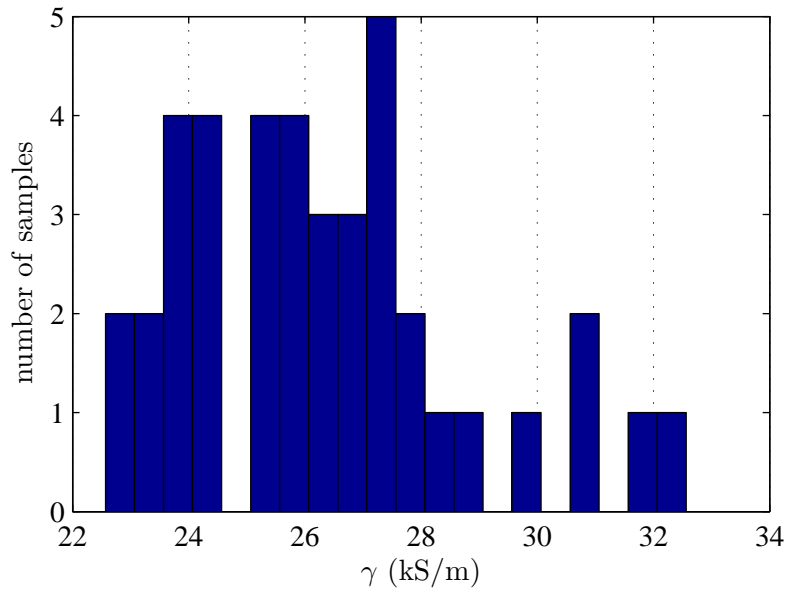


Figure 5.27: Measured electric conductivity of samples S1 to S20 on the top side and bottom side.

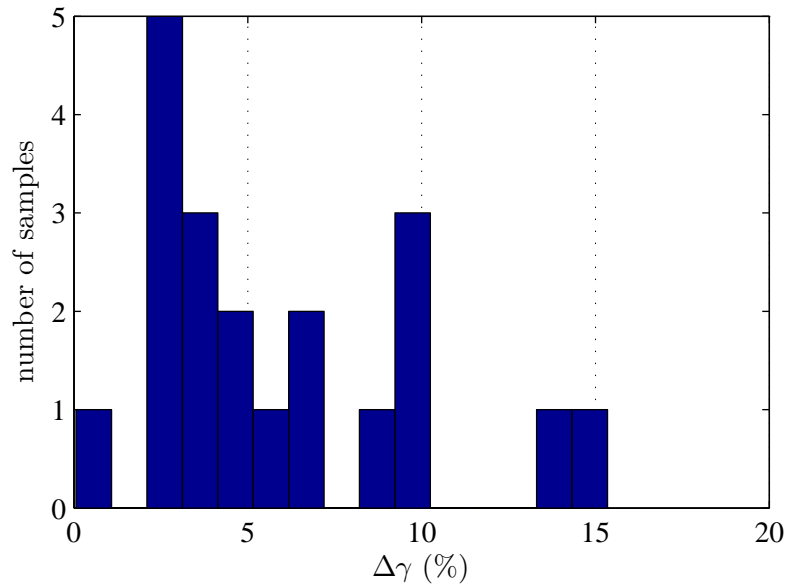


Figure 5.28: Difference between the electric conductivity on the top and on the bottom surface of samples S1 to S20.

5 Application

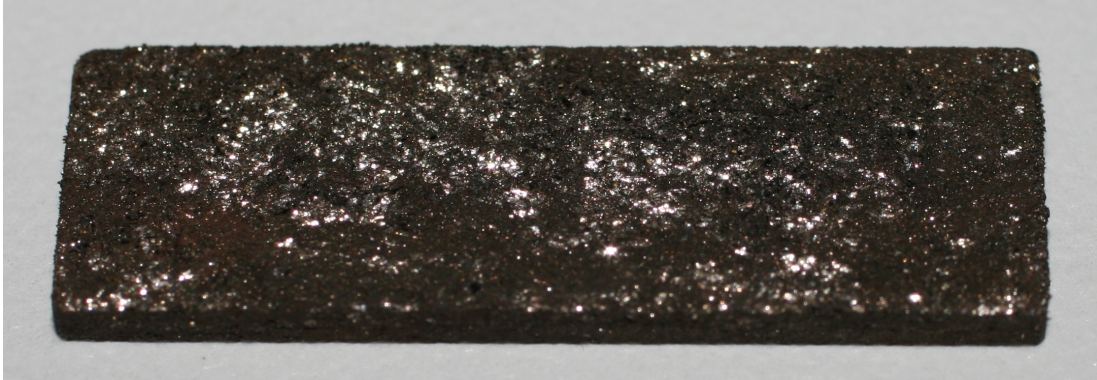


Figure 5.29: Photograph of the top surface of sample S3.

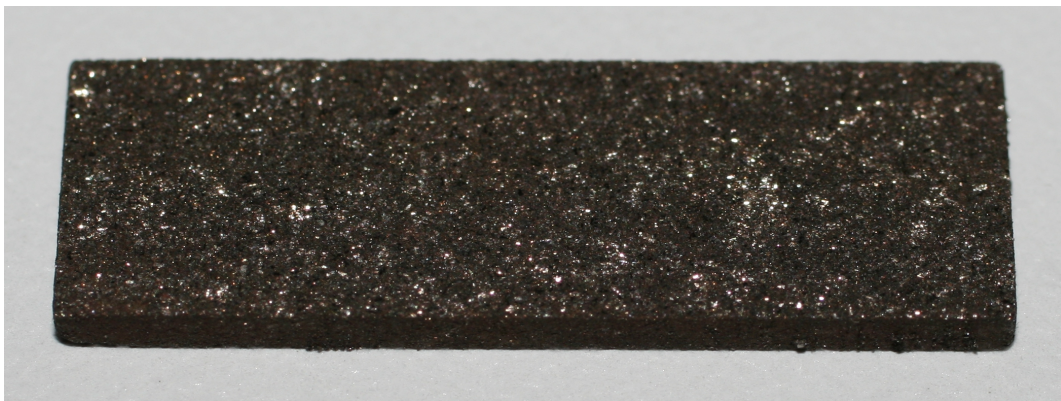


Figure 5.30: Photograph of the bottom surface of sample S3.



Figure 5.31: Photograph of 2 PMs composed of 8 parts during manufacturing.

to $1.38 \mu\Omega\text{m}$ from 20°C to 150°C , which is about 8.2% relative to the value at 20°C . This corresponds to about 7% considering a change to 130°C .

5.4 Measures against Eddy Currents

In order to reduce the heat generated by eddy currents, magnetically soft materials with a high electric conductivity are usually laminated. The magnetic core is laminated in a way that eddy currents are prevented from spreading in one direction normal to the main direction of the flux density. This technique is applied in e.g. transformers, where steel cores with a high permeability and a high saturation are used. In that case, the core is comprised of several layers of sheet metal, up to thousands for large transformers. In the following, this concept is applied to PMs.

Several PM samples were manufactured consisting of smaller PMs. For the first type of samples, a PM is subdivided into 4 parts along its dimension of 25 mm. The second type is composed of 8 parts, where the sample is additionally subdivided along its dimension of 8.3 mm. Two samples of the latter type are depicted in Fig. 5.31 during manufacturing. The individual parts were already magnetized by the manufacturer. In order to assemble one PM of the original size, they were attached to a steel block, which is covered by a polytetrafluoroethylene (PTFE) foil. Pieces of a synthetic foil are put in between the parts to guarantee electric insulation. The parts are bonded by a heat-resistant cyanoacrylate adhesive. The insulating foil is additionally roughened to improve the adhesion. As a practical hint, two other types of adhesive were also tested. A cyanoacrylate especially for strain gauges was found to be too weak, whereas an epoxy resin led to a strong bond, but made reworking cumbersome after the glue set.

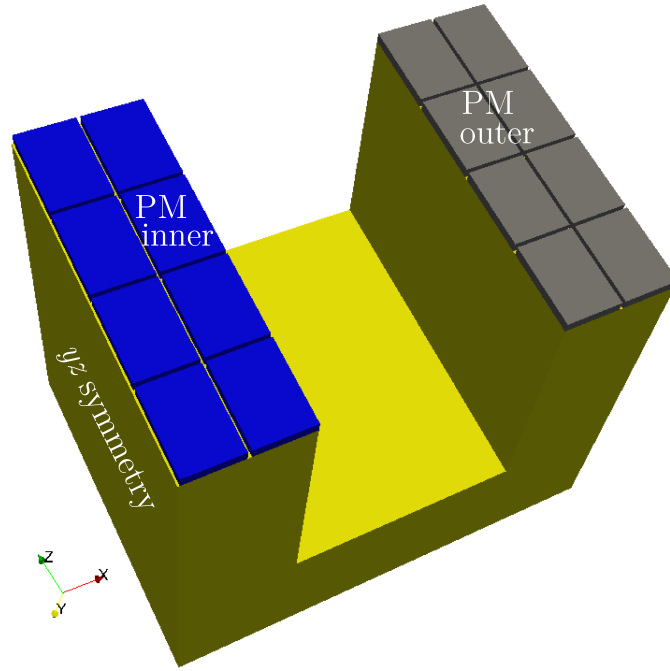


Figure 5.32: FE model of the E-core choke with subdivided PMs. The modeled air and the coil are not shown.

Three of the eight-part samples are included in the magnetic load tests at maximum operating temperature (see Fig. 5.14, Section 5.2.2). They do not show a noticeably different behavior, which demonstrates the applicability. The negligible impact on the operating characteristics is also shown by the simulations in the following.

The FE model, as described in the beginning of the chapter and depicted in Fig. 5.1, is updated regarding the subdivision of the PMs into several parts. The dimensions of the core stay the same, whereas the PM parts are separated by thin layers of air. This means that the composed PM loses some of its volume compared to the full PM, which should only slightly affect the level of biasing. A change of the dimensions of the core would be expected to have more impact, especially on the inductance, which would be inappropriate for comparison. The gap between the parts is assumed as $250\ \mu\text{m}$, which can be observed in the model depicted in Fig. 5.32. As for the previous simulations, the geometric symmetries with respect to the xy , xz and yz planes are exploited. Changes are only made to the PMs and the air region, since the adhesive is modeled with the material characteristics of air.

The flux density characteristics of the choke are shown in Fig. 5.33 for the original and the subdivided PMs from Fig. 5.32. Apart from the phase shift between B and i , the characteristics are nearly the same, which also applies to the inductance. The reduction of the phase shift already indicates a reduction of the eddy currents. In case of the subdivided PMs, the flux density $B_{\text{PM,inner}}$ refers to the center of the innermost

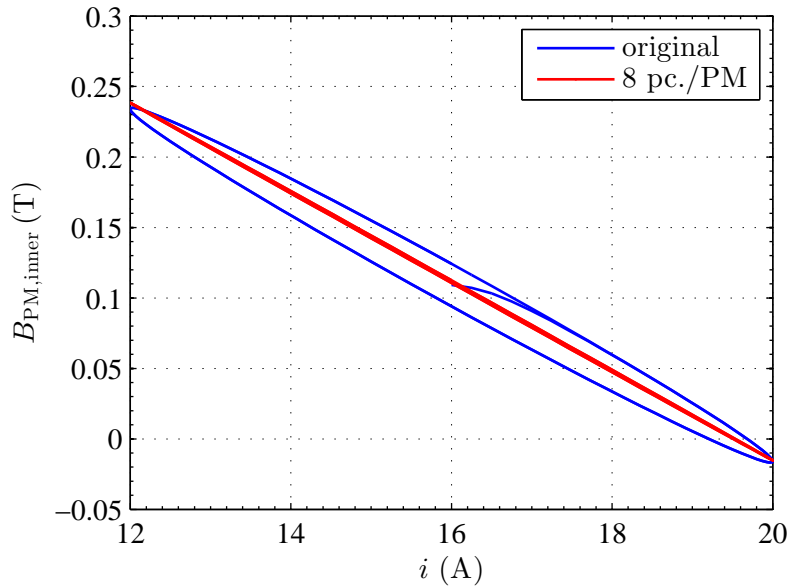


Figure 5.33: Simulated flux density in the subdivided and original PMs of the choke for the worst-case excitation with $N = 56$.

part, i.e. the part closest to the origin of the coordinate system. However, the flux density shows a very homogeneous distribution over all parts of one PM in the cases investigated.

In order to make clear what is meant by the original PMs and subdivided PMs, the bottom view of the model is shown in Fig. 5.34 for all cases investigated. The cases are denoted in such a way that the subdivision refers to one unit PM of the dimensions $25 \text{ mm} \times 8.3 \text{ mm} \times 1.5 \text{ mm}$ as investigated so far. However, in the E-core choke, the inner leg is twice as wide as one of the outer legs. The obvious approach would be to use PMs of the same cross-section as its corresponding leg due to reasons of manufacturing and assembly. This means that the PM in center leg would be twice as wide as a PM in an outer leg, which is referred to as original. In contrast, when subdividing the PM, all PMs are composed of parts of the same size regardless of whether they are in the center leg or in an outer leg. To avoid confusion, the total number of individual PMs is additionally given in Tab. 5.3 with the symmetries with respect to the xy , xz and yz planes taken into account.

To emphasize the difference in the magnitude of the eddy currents, the distribution of the eddy currents is shown in Figures 5.35 and 5.36 at the same time instant of the worst-case excitation. The fundamental difference between the original case and the subdivided cases can be observed again, as the eddy current density is normal to the surface on the yz plane in Fig. 5.35.

The effect of the subdivision on the power of the eddy currents is most interesting, especially regarding the thermal behavior. The resulting power for the worst-case excitation is shown in Figures 5.37 and 5.38 for the inner and the outer PMs, respectively.

5 Application

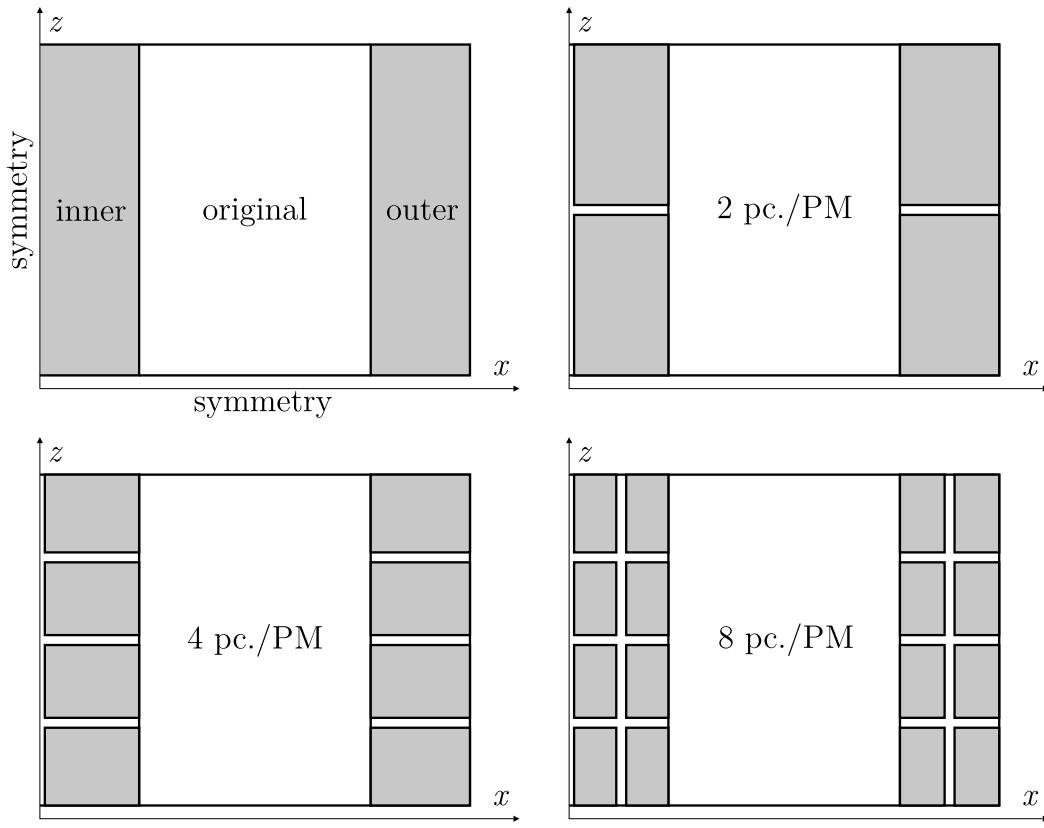


Figure 5.34: Bottom view of the simulation setups of the different cases of subdivision. Not to scale, otherwise the air gaps would barely be visible. The surrounding air and the coils are not shown.

case	inner legs	outer legs	total
original	2	4	6
2 pc./PM	8	8	16
4 pc./PM	16	16	32
8 pc./PM	32	32	64

Table 5.3: Total number of individual PMs for each case of subdivision including symmetries.

5 Application

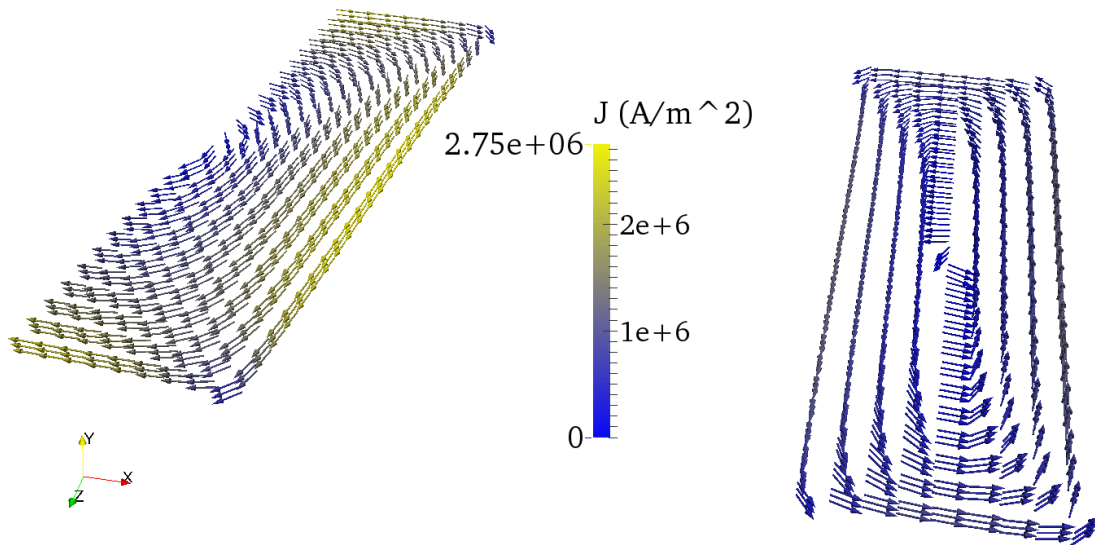


Figure 5.35: Eddy current density in the original PMs of the choke for the worst-case excitation with $N = 56$ at $t = 100 \mu\text{s}$. The length of the vectors does not correspond to the magnitude of \vec{J} for a better visibility.

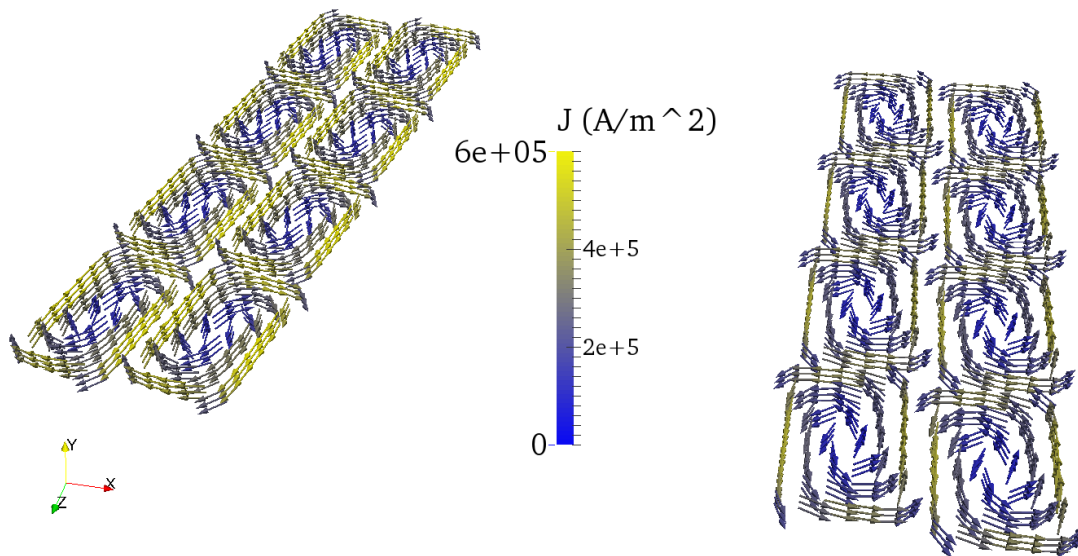


Figure 5.36: Eddy current density in the subdivided PMs of the choke for the worst-case excitation with $N = 56$ at $t = 100 \mu\text{s}$. The length of the vectors does not correspond to the magnitude of \vec{J} for a better visibility.

5 Application

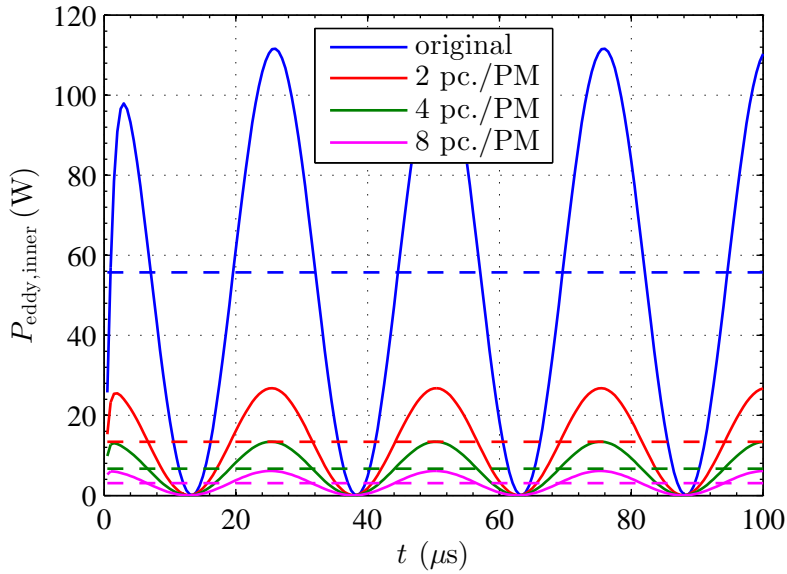


Figure 5.37: Simulated instantaneous power in the subdivided and original inner PMs of the choke for the worst-case excitation with $N = 56$. The dashed lines mark the corresponding mean values over the last $50 \mu\text{s}$.

This is the total power of the PMs of the full E-core choke, meaning that the symmetries are already taken into account. The subdivision leads to an enormous reduction of eddy currents, which is shown in terms of the mean power in Tab. 5.4, calculated according to (3.7). Due to the stray flux, the power of the inner and of the outer PMs is given separately as well as the ratio between them. Again, the difference between the original case and the composition of the PMs of parts of the same size can be observed in the ratio between the power of the outer and inner PMs. In the original case, where the PMs are as wide as the corresponding leg, the outer PMs cause only about 20% of the eddy power of the inner PMs. This changes to about 60% if all PMs consist of equally sized parts, which means that the power density is distributed more evenly.

case	\bar{P}_{inner} (W)	$\bar{P}_{\text{rel,inner}}$ (%)	\bar{P}_{outer} (W)	$\bar{P}_{\text{rel,outer}}$ (%)	$\frac{\bar{P}_{\text{outer}}}{\bar{P}_{\text{inner}}}$ (%)
original	55.71	100	10.92	100	19.61
2 pc./PM	13.40	24.04	8.02	73.46	59.90
4 pc./PM	6.71	12.05	3.98	36.45	59.31
8 pc./PM	3.06	5.50	1.83	16.79	59.88

Table 5.4: Mean power of the eddy currents over one period of the worst-case excitation for different subdivisions of the PMs.

5 Application

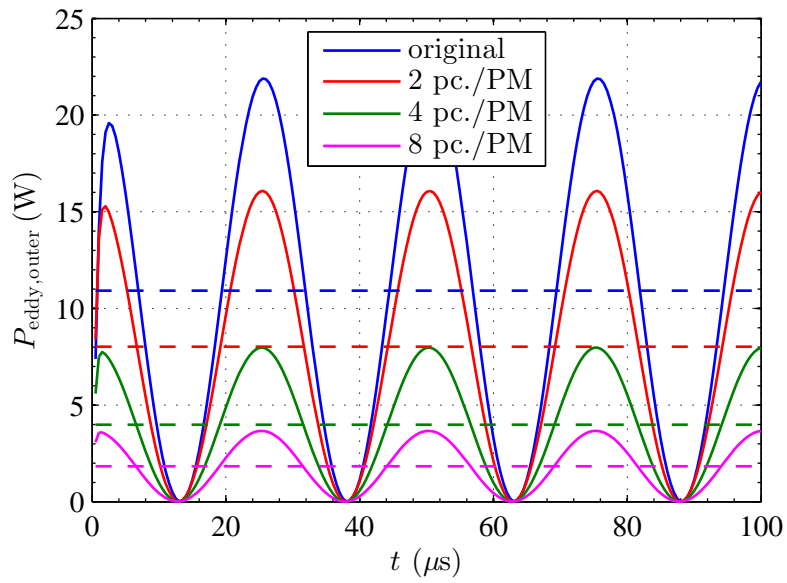


Figure 5.38: Simulated instantaneous power in the subdivided and original outer PMs of the choke for the worst-case excitation with $N = 56$. The dashed lines mark the corresponding mean values over the last $50 \mu\text{s}$.

6 Conclusion

The development of the presented measurement method originates from the need of a fast, flexible and relatively inexpensive characterization of the PMs. The method even allows for the use of a ferrite core, which has a lower saturation than the remanence of the PM, but which is suited for higher frequencies. This enables the investigation of PMs under dynamic conditions, since the eddy currents in the core can be neglected. The characterization is restricted to the main characteristic quantities, i.e. the remanence and the permeability, which are actually the only interesting quantities for the application. Thus, it is not a restriction from the application-oriented point of view. Additionally, it was shown that it is not necessary to measure the whole magnetization curve in order to identify the remanence, which results in a reduction of the required electric power for the measurement. The reduction of the electric power leads to a massive reduction of the cost for the electric power source, especially if the dynamic behavior is investigated with a harmonic excitation. The remanence is identified by means of a magnetic equivalent circuit, which takes the real geometry of the measurement setup into account, whereas the permeability is determined directly. The method of identification is combined with finite element (FE) simulations for the calibration, which determines only one offset parameter. The applicability of the method was demonstrated by the development of a measurement setup, which is capable of tracking the change of both the remanence and the permeability of PMs exposed to elevated temperatures. As an example, during the long-term tests at the maximum operating temperature of 130 °C, the relative permeability changes by a value of about 0.015 consistently for a number of samples over the whole duration, which corresponds to 1.25 % of the nominal relative permeability. Similarly, a change of the remanence in the order of 1 % of the starting remanence can be detected consistently.

The PMs were loaded by temperature and magnetic flux, which were the main quantities expected to have an impact on the PMs. Besides the temperature controlled by an environment simulator, the measurement setup was also able to magnetically load the PM similarly to the choke, since it is actually a similar magnetic circuit. In order to correlate certain effects, the characteristics of the PMs were measured firstly over temperature only and secondly at the maximum operating temperature of 130 °C with simultaneous magnetic load. The magnetic load was expected to have the maximum effect at maximum operating temperature. However, the tests showed that the remanence loss of the PMs was in the same range of a few percent with the magnetic load as without the magnetic load. This leads to the conclusion that the PMs suffer a small irreversible initial loss of remanence caused by the temperature. As those tests were of rather short duration, long-term tests were also conducted. In those experiments, the PMs were heated to a temperature equal to or higher than the specified maximum operating tem-

6 Conclusion

perature and they were not actively magnetically loaded. Due to the previous tests, the temperature is expected to be mainly responsible for the degradation. The PMs show a conclusive loss of remanence at temperatures ranging from 130 °C to 200 °C applied for 86 h. The general trend is a loss of remanence and an increase of the permeability, which indicates that the coercive field decreases faster than the remanence. It could be shown that the rate of change also depends on the history of the samples, since samples lost less remanence and gained less permeability if they had already been loaded. At only 130 °C, the increasing trend of the permeability can also be observed, but it is in a negligible range, which is the already mentioned 1.25 %. It can be concluded from the results of the tests, short-term as well as long-term, that the presented choke only fails if the maximum operating temperature of 130 °C is significantly exceeded for longer than 2 h at most.

A way to reduce the eddy currents, and therefore the temperature, is to subdivide the PMs into several parts, which is basically the same principle as applied to laminated cores. In the presented example, the subdivision of one original PM into 16 parts led to a simulated decrease of the power of the eddy currents by about 94.5 % in the inner leg of the E-core choke. This reduction is not accompanied by a much higher effort, since the PM pieces still have a cross-section of about 6 mm × 4 mm, which is a size that is still easy to handle.

In conclusion, in order to predict the failure of a choke, many effects have to be taken into account. Those include the non-linear behavior of the PM as well as the core and their temperature dependence, the electric conductivity of the PM and its temperature dependence, and the thermal characteristics of the materials. However, some material parameters might not be available from the manufacturer. Additionally, the manufacturer mostly provides more of a parameter range, since there is a high variance due to the manufacturing process. The electric conductivity is especially challenging, since it depends on the homogeneity of the mixed powder material in case of plastic-bonded permanent magnets. For the simulation and the understanding, the interaction between the different effects is of major interest. By changing the temperature, several effects occur simultaneously. The remanence decreases, the permeability increases and the electric conductivity decreases, which both influence the field distribution, the eddy currents and therefore the temperature itself. However, transient electromagnetic simulations coupled with the heat equation are very time-consuming due to the difference in scale of the time constants. Instead, a series of simulations at different temperatures could be more effective in order to obtain a region for the safe use of PMs. The field intensity of the PM seems one of the most important quantity to observe, since the coercive field of the polarization determines the point at which the PM can be weakened or demagnetized and it determines the magnetic voltage which can be countered regarding the coil. It also marks the point where the permeability of the PM can no longer be modeled linearly.

Bibliography

- [1] M. Kaltenbacher, *Numerical Simulation of Mechatronic Sensors and Actuators: Finite Elements for Computational Multiphysics*, Springer, ed. 3 (2015).
- [2] A. R. Aguilar, and S. Munk-Nielsen, *Design, Analysis and Simulation of Magnetic Biased Inductors with Saturation-Gap*, 16th European Conference on Power Electronics and Applications, Lappeenranta, Finland (2014).
- [3] A. R. Aguilar, and S. Munk-Nielsen, *Method for Introducing Bias Magnetization in Ungaped Cores: "The Saturation-Gap"*, Applied Power Electronics Conference and Exposition, Fort Worth, TX, USA (2014).
- [4] S. Herzog, A. Stadler, and Ch. Gulden, *MaxFlux - Magnetically Biased Inductor*, Bodo's Power Systems, Laboe, Germany (2014).
- [5] *InDUR MaxFlux*, technical document, STS - Spezialtransformatoren Stockach GmbH & Co. KG, Stockach, Germany (2014).
- [6] A. Stadler, Ch. Gulden, and T. Stolzke, *Nonlinear Inductors for Active Power Factor Correction Circuits*, 15th International Power Electronics and Motion Control Conference, Novi Sad, Serbia (2012).
- [7] L. Reznik, *Payton Planar Magnetics - An Innovative Technology for Modern SMPS*, technical document, Payton Group International (n.y.).
- [8] S. Liu, and E. P. Hoffman, *Application-Oriented Characterization of $Sm_2(Co,Fe,Cu,Zr)_{17}$ Permanent Magnets*, IEEE Transactions on Magnetics, Vol. 32, No. 5 (1996).
- [9] S. Ruoho et al., *Temperature Dependence of Resistivity of Sintered Rare-Earth Permanent-Magnet Materials*, IEEE Transactions on Magnetics, Vol. 46, No. 1 (2010).
- [10] Ch. Kral et al., *Modeling Demagnetization Effects in Permanent Magnet Synchronous Machines*, 19th International Conference on Electrical Machines, Rome, Italy (2010).
- [11] A. Belahcen, and A. Arkkio, *Permanent Magnets Models and Losses in 2D FEM Simulation of Electrical Machines*, 19th International Conference on Electrical Machines, Rome, Italy (2010).

Bibliography

- [12] S. Ruoho, E. Dlala, and A. Arkkio, *Comparison of Demagnetization Models for Finite-Element Analysis of Permanent-Magnet Synchronous Machines*, IEEE Transactions on Magnetics, Vol. 43, No. 11 (2007).
- [13] S. C. Mukhopadhyay, M. Iwahara, and S. Yaniada, *Investigation of the Performances of a Permanent Magnet Biased Fault Current Limiting Reactor with a Steel Core*, IEEE Transactions on Magnetics, Vol. 34, No. 4 (1998).
- [14] R. Wrobel, N. McNeill, and Ph. H. Mellor, *Design of a High-Temperature Pre-Biased Line Choke for Power Electronics Applications*, Power Electronics Specialists Conference, Rhodes, Greece (2008).
- [15] G. M. Shane, and S. D. Sudhoff, *Permanent Magnet Inductor Design*, Electric Ship Technologies Symposium, Alexandria, VA, USA (2011).
- [16] F. Fiorillo, *Measurement and Characterization of Magnetic Materials*, Elsevier Academic Press (2004).
- [17] S. Tumanski, *Handbook of Magnetic Measurements*, CRC Press (2011).
- [18] J. T. Ludwig, *Design of Optimum Inductors Using Magnetically Hard Ferrites in Combination with Magnetically Soft Materials*, Journal of Applied Physics 29, 497 (1958).
- [19] R. Cornelius et al., *Pulsed Field Magnetometer for Industrial Use*, IEEE Transactions on Magnetics, Vol. 38, No. 5 (2002).
- [20] D. Dufeu, and P. Lethuillier, *High Sensitivity 2 T Vibrating Sample Magnetometer*, Review of Scientific Instruments 70, 3035-3039 (1999).
- [21] O. Cugat, R. Byrne, J. McCaulay, and J. M. D. Coey, *A Compact Vibrating-sample Magnetometer with Variable Permanent Magnet Flux Source*, Review of Scientific Instruments 65, 3570 (1994).
- [22] R. Grössinger, G. W. Jewell, J. Dudding, and D. Howe, *Pulsed Field Magnetometry*, IEEE Transactions on Magnetics, Vol. 29, No. 6 (1993).
- [23] C. Golovanov, G. Reyne, G. Meunier, R. Grössinger, and J. Dudding, *Finite Element Modeling of Permanent Magnets Under Pulsed Field*, IEEE Transactions on Magnetics, Vol. 36, No. 4 (2000).
- [24] J. C. Téllez-Blanco, R. Sato Turtelli, R. Grössinger, E. Estévez-Rams, and J. Fidler, *Giant Magnetic Viscosity in SmCo 5-x Cu x Alloys*, Journal of Applied Physics 86, 5157 (1999).
- [25] H. Husstedt, *Measurement of Magnetic Fields for the Testing of Automotive Sensors*, dissertation, University of Klagenfurt, Austria (2012).

Bibliography

- [26] H. Husstedt, and M. Kaltenbacher, *Using the Redundancy of the Magnetic Field for Magnetic Scanning Applications*, Journal of Applied Physics 113, 173905 (2013).
- [27] H. Husstedt, and M. Kaltenbacher, *Detailed Analysis of Permanent Magnets by Means of Free Field Measurements*, Journal of Applied Physics 115, 17E302 (2014).
- [28] D. Perchtold, *Permanent Magnets in Chokes*, master thesis, University of Klagenfurt, Austria (2013).
- [29] D. Perchtold, H. Husstedt, and M. Kaltenbacher, *A Method for Parameter Identification of Thin Permanent Magnets at Higher Frequency and Temperature Ranges*, IEEE Transactions on Magnetics, Vol. 51, No. 10 (2015).
- [30] D. Perchtold, M. Kaltenbacher, and H. Husstedt, *Testing of Thin Permanent Magnets at Higher Frequencies*, 17th International Conference on Sensors and Measurement Technology, Nürnberg, Germany (2015).
- [31] R. Fratila, A. Benabou, A. Tounzi, and J. C. Mipo, *Nonlinear Modeling of Magnetization Loss in Permanent Magnets*, IEEE Transactions on Magnetics, Vol. 48, No. 11 (2012).
- [32] M. Weiß, J. Ilg, S. J. Rupitsch, and R. Lerch, *Inverse Method for Determining Material Parameters of Piezoceramics and Passive Materials*, 17th International Conference on Sensors and Measurement Technology, Nürnberg, Germany (2015).
- [33] P. Campbell, *Comments on Energy Stored in Permanent Magnets*, IEEE Transactions on Magnetics, Vol. 36, No. 1 (2000).

Curriculum Vitae

Personal Data

Name	Dominik Perchtold
Date of birth	August 19, 1986
Place of birth	Wels, Austria

Education

06/2004	General qualification for university entrance, Bundesgymnasium Anton-Bruckner-Straße, Wels, Austria Final exam in German, English, Latin, mathematics and computer science
10/2006 to 12/2009	Dipl.-Ing. (FH) in automation engineering, University of Applied Sciences Upper Austria, Wels, Austria Specialization: microsystems technology
03/2010 to 02/2013	Dipl.-Ing. in information technology with distinction, University of Klagenfurt, Austria Specializations: applied mechatronics, control systems engineering

Professional Experience

Summer holidays 2002, 03, 04 and 05	Warehouseman at Interspar GmbH, Wels, Austria
09/2004 to 05/2005	Military service, gunner, armoured reconnaissance, Hessen-Kaserne, Wels, Austria
07/2007 to 09/2007	Internship as technical assistant at the University of Applied Sciences Upper Austria, Wels, Austria
09/2008 to 10/2009	Internship and diploma thesis at Infineon Technologies Austria AG, Villach, Austria
03/2010 to 07/2012	Project assistant at the Institute of Applied Mechatronics, University of Klagenfurt, Austria
since 08/2012	Project assistant at the Institute of Mechanics and Mechatronics, TU Wien, Austria